UNIVERSITY OF SOUTHAMPTON

FACULTY OF ENGINEERING AND THE ENVIRONMENT

Domain Wall Dynamics and Resonant Modes of Magnetic Nanostructures

A thesis submitted in partial fulfillment of the requirements
for the degree of Doctor of Philosophy

Author:
Maximilian ALBERT

Supervisors:
Prof Hans FANGOHR
Dr Markus BREDE

September 2016

UNIVERSITY OF SOUTHAMPTON

ABSTRACT

FACULTY OF ENGINEERING AND THE ENVIRONMENT

Doctor of Philosophy

Domain Wall Dynamics and Resonant Modes of Magnetic Nanostructures

by Maximilian Albert

In this work we present finite element-based simulations of magnetic nanostructures using the micromagnetic software packages `Nmag` and `Finmag` developed at the University of Southampton.

As part of this work the package `Finmag` has been extended with the implementation of an eigenvalue-based method to compute resonant modes in magnetic nanosystems. The details of this implementation are discussed, including certain complications encountered in the context of a finite element discretisation scheme. The implementation is verified using results from an independently published study on eigenmodes of an elliptical nanodisc.

We present two studies of domain walls in magnetic nanowires. The first one investigates field-driven domain wall motion in nanowires with edge roughness. A new roughness model is introduced which allows the systematic study of how edge roughness features influence the domain wall motion compared to the case of a smooth nanowire. While the large-scale behaviour, such as the asymptotic domain wall velocity, is largely unaffected by the roughness, it introduces marked local alterations to the domain wall trajectories and can lead to dynamic pinning, both below and above the Walker breakdown. It is shown that the effective pinning strength of the roughness features is strongest when their size is comparable to the size of the domain wall.

The second domain wall study investigates different types of resonant modes (translational, breathing and twisting modes) of transverse domain walls pinned at notches in a

magnetic nanowire. The different sensititivies of each mode type on the nanowire and notch geometry are investigated in detail. It is found that the translational and twisting mode respond relatively strongly to changes in the notch geometry, while the breathing mode is fairly robust to changes in the notches' size, making it a promising candidate for applications.

We finally present a study of resonant modes in an elliptical magnetic nanodisc representing the free layer of a spin-torque nano-oscillator. We demonstrate that the resonant frequencies and spatial mode profiles are altered in the presence of a magnetic nanoparticle. The dependence of the frequency shifts on the nanoparticle position and material parameters is studied systematically. It is shown that these frequency shifts exceed achievable linewidths in state-of-the-art spin-torque oscillators and that they can be maintained over large external field ranges (owing to to the fact that they are a direct response to the stray field of the nanoparticle and do not rely on changes to the magnetic ground state of the disc). This opens up promising applications for novel nano-sensing devices using frequency-based detection schemes.

Contents

List of Figures

List of Tables

Declaration of Authorship

I, Maximilian Albert, declare that this thesis titled “Domain Wall Dynamics and Resonant Modes of Magnetic Nanostructures” and the work presented in it are my own and has been generated by me as the result of my own original research.

I confirm that:

1. This work was done wholly or mainly while in candidature for a research degree at this University;
2. Where any part of this thesis has previously been submitted for a degree or any other qualification at this University or any other institution, this has been clearly stated;
3. Where I have consulted the published work of others, this is always clearly attributed;
4. Where I have quoted from the work of others, the source is always given. With the exception of such quotations, this thesis is entirely my own work;
5. I have acknowledged all main sources of help;
6. Where the thesis is based on work done by myself jointly with others, I have made clear exactly what was done by others and what I have contributed myself;
7. Parts of this work have been published as:

    a) M. Albert, M. Franchin, T. Fischbacher, G. Meier, and H. Fangohr. “Domain wall motion in perpendicular anisotropy nanowires with edge roughness”. In: *Journal of Physics: Condensed Matter* 24.2 (2012), p. 024219

    b) M. Albert, M. Beg, D. Chernyshenko, M.-A. Bisotti, R. L. Carey, H. Fangohr, and P. J. Metaxas. “Frequency-based nanoparticle sensing over large field ranges using the ferromagnetic resonances of a magnetic nanodisc”. In: *Nanotechnology* (in press) (2016)

c) M. Albert, P. J. Metaxas, and H. Fangohr. *Supplementary material for "Frequency-based nanoparticle sensing over large field ranges using the ferromagnetic resonances of a magnetic nanodisc"*. 2016. URL: http://dx.doi.org/10.5281/zenodo.60605

d) P. J. Metaxas, M. Sushruth, R. A. Begley, J. Ding, R. C. Woodward, I. S. Maksymov, M. Albert, W. Wang, H. Fangohr, A. O. Adeyeye, and M. Kostylev. "Sensing magnetic nanoparticles using nano-confined ferromagnetic resonances in a magnonic crystal". In: *Applied Physics Letters* 106.23 (2015), p. 232406

e) P. J. Metaxas, M. Albert, S. Lequeux, V. Cros, J. Grollier, P. Bortolotti, A. Anane, and H. Fangohr. "Resonant translational, breathing, and twisting modes of transverse magnetic domain walls pinned at notches". In: *Physical Review B* 93.5 (2016), p. 054414

f) A. Baker, M. Beg, G. Ashton, M. Albert, D. Chernyshenko, W. Wang, S. Zhang, M.-A. Bisotti, M. Franchin, C. L. Hu, R. Stamps, T. Hesjedal, and H. Fangohr. "Proposal of a micromagnetic standard problem for ferromagnetic resonance simulations". In: *Journal of Magnetism and Magnetic Materials* 421 (2017), pp. 428 –439

g) M. Albert, G. Ashton, H. Fangohr, and A. Baker. *Code and data for micromagnetic standard problem on ferromagnetic resonance*. 2016. URL: http://dx.doi.org/10.5281/zenodo.59714

h) H. Fangohr, M. Albert, and M. Franchin. "Nmag Micromagnetic Simulation Tool: Software Engineering Lessons Learned". In: *Proceedings of the International Workshop on Software Engineering for Science*. SE4Science '16. Austin, Texas: ACM, 2016, pp. 1–7

Signed: .....

Date: .....

Acknowledgements

First of all, I would like express my sincere gratitude to my supervisor Prof Hans Fangohr for his continued support over the course of my PhD, including multiple difficult times and circumstances. Without his support and encouragement I would not have been able to complete this PhD and I am immensely grateful for it.

Similarly, my heartfelt thanks go to Dr Peter Metaxas for a fantastic collaboration over the course of multiple years and all his support, both during my research stay at UWA in Perth and during our remote work.

I would like to thank my previous supervisor Dr Thomas Fischbacher for all his support and encouragement during the first phase of my PhD before he left the University of Southampton. I have learned a huge deal from him during our numerous discussions, both about physics and many other subjects, for which I am immensely grateful.

My sincere thanks go to the directors of the Doctoral Training Centre for Complex Systems Simulation, Prof Seth Bullock, Prof Jonathan Essex and Prof Fangohr, as well as Nicki Lewin and Tracey Cantlie, for making this experience possible by creating and running such a fantastic DTC.

Big thanks go also to my colleagues and collaborators in Prof Fangohr's research group and the DTC of Complex Systems Simulations, all of who have made the past years a unique experience.

Many people have accompanied me on parts of this journey. I am very grateful for all the happy moments they shared with me and for their help when times were difficult and I felt like giving in to feelings of despair. In particular, I would like to thank Elisabeth for helping me bring structure to the last phase of writing up when everything was about to get lost in chaos, and for many deep discussions about all aspects of life before and after; Alex, Jake and Khilan for being awesome friends and housemates, and for whiskey, songs and lots of laughter; Sonya for countless moments of silliness over all those years

of our friendhship and our shared PhD experience; Dana for being an amazing person and enriching everyone's life that she touches; and last but not least Maike for special years that I will treasure for the happy and the difficult times, both of which have taught me a lot and helped me grow as a person.

Finally, I would like to thank my family for their never-ending love and support: my mother, who is the most unconditionally loving person I know and who has always supported me in everything I did; my sister, for being such a truly amazing and positive person who has taught me so many things in life about love, friendship and caring for each other; my father, whose unique creativity, vast knowledge and deep humanity I will always admire and remember; and Finja, for being the new sunshine in our lives. I would like to dedicate this thesis to them.

The funding for my PhD research was provided by the Faculty of Engineering and the Environment at the University of Southampton and by the EPSRC Centre for Doctoral Training grant EP/G03690X/1. Support for my research stay at UWA was provided in part by the University of Western Australia's Research Collaboration Award scheme.

List of Publications

Publications utilising some of the work described in this thesis:

1. M. Albert, M. Franchin, T. Fischbacher, G. Meier, and H. Fangohr. “Domain wall motion in perpendicular anisotropy nanowires with edge roughness”. In: *Journal of Physics: Condensed Matter* 24.2 (2012), p. 024219

2. M. Albert, M. Beg, D. Chernyshenko, M.-A. Bisotti, R. L. Carey, H. Fangohr, and P. J. Metaxas. “Frequency-based nanoparticle sensing over large field ranges using the ferromagnetic resonances of a magnetic nanodisc”. In: *Nanotechnology* (in press) (2016)

3. M. Albert, P. J. Metaxas, and H. Fangohr. *Supplementary material for "Frequency-based nanoparticle sensing over large field ranges using the ferromagnetic resonances of a magnetic nanodisc"*. 2016. URL: http://dx.doi.org/10.5281/zenodo.60605

4. P. J. Metaxas, M. Sushruth, R. A. Begley, J. Ding, R. C. Woodward, I. S. Maksymov, M. Albert, W. Wang, H. Fangohr, A. O. Adeyeye, and M. Kostylev. “Sensing magnetic nanoparticles using nano-confined ferromagnetic resonances in a magnonic crystal”. In: *Applied Physics Letters* 106.23 (2015), p. 232406

5. P. J. Metaxas, M. Albert, S. Lequeux, V. Cros, J. Grollier, P. Bortolotti, A. Anane, and H. Fangohr. “Resonant translational, breathing, and twisting modes of transverse magnetic domain walls pinned at notches”. In: *Physical Review B* 93.5 (2016), p. 054414

6. A. Baker, M. Beg, G. Ashton, M. Albert, D. Chernyshenko, W. Wang, S. Zhang, M.-A. Bisotti, M. Franchin, C. L. Hu, R. Stamps, T. Hesjedal, and H. Fangohr. “Proposal of a micromagnetic standard problem for ferromagnetic resonance simulations”. In: *Journal of Magnetism and Magnetic Materials* 421 (2017), pp. 428 –439

7. M. Albert, G. Ashton, H. Fangohr, and A. Baker. *Code and data for micromagnetic standard problem on ferromagnetic resonance*. 2016. URL: http://dx.doi.org/10.5281/zenodo.59714

8. H. Fangohr, M. Albert, and M. Franchin. "Nmag Micromagnetic Simulation Tool: Software Engineering Lessons Learned". In: *Proceedings of the International Workshop on Software Engineering for Science*. SE4Science '16. Austin, Texas: ACM, 2016, pp. 1–7

Publications which use my software contributions to `Nmag` and `Finmag`:

1. M. Franchin, A. Knittel, M. Albert, D. S. Chernyshenko, T. Fischbacher, A. Prabhakar, and H. Fangohr. "Enhanced spin transfer torque effect for transverse domain walls in cylindrical nanowires". In: *Physical Review B* 84.9 (2011), p. 094409

2. W. Wang, M. Dvornik, M.-A. Bisotti, D. Chernyshenko, M. Beg, M. Albert, A. Vansteenkiste, B. V. Waeyenberge, A. N. Kuchko, V. V. Kruglyak, and H. Fangohr. "Phenomenological description of the nonlocal magnetization relaxation in magnonics, spintronics, and domain-wall dynamics". In: *Physical Review B* 92.5 (2015), p. 054430

3. W. Wang, M. Albert, M. Beg, M.-A. Bisotti, D. Chernyshenko, D. Cortés-Ortuño, I. Hawke, and H. Fangohr. "Magnon-Driven Domain-Wall Motion with the Dzyaloshinskii-Moriya Interaction". In: *Physical Review Letters* 114.8 (2015), p. 087203

4. M. Beg, R. Carey, W. Wang, D. Cortés-Ortuño, M. Vousden, M.-A. Bisotti, M. Albert, D. Chernyshenko, O. Hovorka, R. L. Stamps, and H. Fangohr. "Ground state search, hysteretic behaviour, and reversal mechanism of skyrmionic textures in confined helimagnetic nanostructures". In: *Scientific Reports* 5 (2015), p. 17137

Publications unrelated to work in this thesis

1. M. Albert and A. Maier. "Additive polynomials for finite groups of Lie type". In: *Israel Journal of Mathematics* 186.1 (2012), pp. 125–195

2. R. Wilson, E. zu Erbach-Schoenberg, M. Albert, D. Power, S. Tudge, M. Gonzalez, S. Guthrie, H. Chamberlain, C. Brooks, C. Hughes, L. Pitonakova, C. Buckee, X. Lu, E. Wetter, A. Tatem, and L. Bengtsson. "Rapid and near Real-time Assessments of

Population Displacement Using Mobile Phone Data Following Disasters: The 2015 Nepal Earthquake". In: *PLOS Currents Disasters* (2016)

Chapter 1

Introduction

Over the past decades, computer simulations have become a ubiquitous and indispensable tool to assist research in engineering disciplines, as well as more theoretical branches of science. [1] Especially in areas where it is a formidable engineering challenge to build devices of interest, or perform experiments and measurements on them, computer simulations can be invaluable to explore ideas, conduct feasibility studies and develop or guide intuition. This is true for a large number of fields ranging from aerospace engineering to nanotechnology. In nanotechnology, for example, it is highly challenging to build nanostructures with sufficient precision and reproducibility, and a great deal of research is dedicated to building devices with higher accuracy. Even after samples have been successfully manufactured it is highly non-trivial to perform accurate measurements on them. Due to their smallness (typically on the order of $100\,\mathrm{nm}$ to a few micrometres) and the very short timescales of magnetisation dynamics (picoseconds to nanoseconds), accurate measurements are a challenge. This is reflected in the fact that routinely some of the highest-ranking publications report of breakthroughs in new measurement or imaging techniques. [2–6]

Despite continuing improvements in those techniques, frequently an experimental physicist can obtain only limited information from a measurement – for example, the spatially averaged value of the magnetisation across the studied sample, or the total power absorbed when the sample is excited at a certain frequency. While this can give us a certain level of insight into what is happening in the system, some effects cannot be explained by these types of measurements alone. Models can give us greater insights into the underlying processes and detailed dynamics that cause the experimentally observed behaviour. They allow us to gain a deeper understanding in these situations, helping to refine our theories and to make predictions about new effects or to design novel kinds of devices.

In certain cases it is possible to capture a system's behaviour using very simplified one- or two-dimensional models, or even macrospin models where the complex three-dimensional behaviour of the real system is represented by a single "macrospin" vector instead of a spatially resolved vector field. The Stoner-Wohlfarth model [7, 8], which successfully explains the basic principle behind magnetic hysteresis in single-domain magnetic nanoparticles, is one of most well-known examples of such a macrospin model. Richer simulations, based on the micromagnetic model introduced by Brown [9], can provide a valuable tool to enhance our understanding enabling us to study certain effects and processes in much more intricate detail. Micromagnetic simulations cover a middle ground between the experimental investigation of real samples and the drastic simplifications of analytical calculations or models with reduced dimensionality. They allow computing a fully 3d-resolved time evolution of the magnetic patterns in a nanodevice. With current technology this is virtually impossible to obtain in a real laboratory.

Micromagnetic simulations come with their own set of challenges – for example, the occurrence of stiff differential equations requiring a small timestep during time integration, large data output for high spatial and temporal resolutions, etc. Moreover, the micromagnetic model also makes certain simplifying assumptions. For example, the magnetisation is assumed to be continuous, disallowing systems that are too close to atomic resolution (for which other simulation techniques are more appropriate). Also, temperature effects are typically not included because the saturation magnetisation M_s of a material is assumed to be constant. However, if used consciously the simplifying assumptions in a model need not necessarily present a disadvantage. If a simplified model successfully explains an observation then this can tell us something about the dominant effects and the relevant mechanisms at play in the system, especially if the model can make new predictions that are later verified by experiments. While providing a powerful tool, models and simulations in turn rely on observations and real data for parameterisation and to ensure simplifications are justified. Ideally, simulations and experiments should go hand in hand to complement the insight gained from each other and mutually guide the direction of research. Increasingly, high-profile studies tend to follow this pattern of complementing experimental measurements with simulation results (e.g. [10, 11]).

The main focus of the work in this thesis is on two types of magnetic nanostructures: domain walls (DWs) in magnetic nanowires and nanodisks in various flavours.

In magnetic materials, the competition between (mostly) the exchange interaction and

the magnetostatic interaction (see Chapter 2) leads to the formation of so-called domains – regions of essentially uniform magnetisation which are separated by narrow transition regions called domain walls. Magnetic storage devices rely on domains to represent information stored as bits (e.g., magnetisation down=0, magnetisation up=1). A solid understanding of domain walls is crucial in order to understand the stability and switching of these domains, which is important for the design of smaller, faster and denser storage technologies.

Domain walls have been an area of active research for a long time and their basic properties are well-understood. Yet, despite their apparent simplicity they exhibit rich and sometimes surprising behaviour. For example, domain walls can be pushed along nanowires by use of an external field. The domain wall speed increases linearly with the field strength, but only up to a certain critical field at which a "phase transition" occurs and the motion switches from steady motion along the wire to oscillatory motion, which drastically reduces the average domain wall speed – a phenomenon known as "Walker breakdown". [12]

Another, seemingly unrelated, phenomenon in magnetic nanostructures is the so-called spin-transfer torque effect which was independently suggested by Slonczewksi [13] and Berger [14] and shortly afterwards confirmed experimentally. Simply put, when an electric current flows through a magnetic material the electron spins interact with the magnetisation. By passing through a ferromagnetic layer with fixed magnetisation, the current can become partially spin-polarised, and such a spin-polarised current can then exert a torque on the magnetisation in a second ferromagnetic layer where the magnetisation is free to precess. This effect can be used to manipulate the magnetisation in a material without the need for any external fields, which opens up completely new possibilities in the design of magnetic nanodevices.

The combination of spin-transfer torque and domain walls has led to the suggestion of a novel data storage mechanism. Currently available magnetic storage devices use magnetic fields created by a read/write head to store information on a hard disk and to retreive it later. The use of a mechanical components (like the read/write head and the moving arm to which it is attached) present a disadvantage because they need to be engineered to very high precision[1] and need to be able to deal with enormous stress during operation, which makes them prone to failure. Moreover, current hard disk drives are limited to effectively two-dimensional storage technology because the

[1] A common analogy makes the comparison with a fighter jet flying at supersonic speeds a few inches above the ground while it needs to be able to count every single blade of grass.

read/write head needs to move freely above the platter containing the data. A novel design by Parkin [15] (dubbed "racetrack memory") suggests to use the spin-transfer torque effect to push the domain walls (and thus the domains) along the wire, i.e. to shift the information itself towards a location where it can be read off, rather than having an external component move towards the information. This would eliminate the need for any mechanical parts and might even open up the path towards true three-dimensional storage technology. There are many unsolved questions with this approach (e.g., the prohibitively high current densities[2] in currently available materials which would lead to overheating in nanowires), but it is a very interesting and promising suggestion.

For applications such as the racetrack memory it is crucial to understand how domain walls travel along nanowires. In Chapter 3 we report a micromagnetic study of how edge roughness can impact domain wall motion in a nanowire. This is important for real-world applications because a fabricated sample will inevitably exhibit imperfections. It also illustrates how simplifications made in computer simulations (e.g. to use perfectly smooth wires) may lead to the inability to capture important behaviour (e.g. domain wall pinning).

Nanotechnology has also become very important in applications related to sensing, especially in the context of so-called lab-on-a-chip applications. Current nano-sensing technology almost exclusively works on basis of the so-called giant magnetoresistive (GMR) effect. The original discovery of the magnetoresistive effect at first did not receive much attention until more recent advances in material science have led to a much bigger (hence the term "giant") effect that is very important in modern applications. The way this effect works is that the sensor is composed of two different magnetic layers, separated by a metallic (but non-magnetic) spacer layer to avoid exchange coupling between the two. Since the entire structure is conducting, its resistance can be measured. With a suitable choice of materials this resistance can vary considerably depending on the relative orientation of the two layers. The device is fabricated in such a way that the magnetisation in the bottom layer is "fixed" so that in the presence of a moderate external field its orientation does not change. By contrast, the top layer is a "free" layer whose magnetisation responds to and aligns with an external field. Therefore the resistance of the structure is an indication of whether or not an external field is applied and which direction it points

[2] The problem of high current-densities may be solvable with the recent (re-)discovery of DMI materials. These allow topological structures called Skyrmions which, like domain walls, can be used to store individual bits of information. Recent research suggests that Skyrmians may need much lower current-densities to travel along nanowires.

in. Current nanosensing technology works by using precisely this effect, where the difference in the external field "felt" by the sensor is due to the presence of a nearby magnetic nanoparticle.[3] These nanoparticles can be "functionalised" by coating them with polymers and tagging them with specific labels which act like antibodies that attach only to a specific analyte of interest (e.g., a protein or a chemical pollutant) and can thus be used for sensing purposes. The advantage of this is that many biological and environmental samples exhibit negligible "magnetic background" so that magnetic sensing technologies can achieve very high sensitivity.

In Chapter 7 we report a study exploring a novel sensing mechanisms based on a more sophisticated scheme using so-called spin-transfer nano-oscillators (STNOs), which use the spin-transfer torque effect mentioned above to create a steady precession of the magnetisation so that they can act as nanoscale microwave emitters. We explore the resonant frequencies and oscillation modes in a magnetic nanodisc representing the free layer of a STNO. The key question is whether the presence of a magnetic nanoparticle in the vicinity of the disc is able to alter the resonances in a way that can be measured experimentally. This will be investigated in Chapter 7.

The study of resonant modes in general forms a core topic of this work, and a key contribution was to implement an eigenvalue-based method in the finite element-based micromagnetic simulation package `Finmag` which is collaboratively developed at the University of Southampton. The details of this implementation, as well as a comparison with the so-called *ringdown method* is presented in Chapter 4 and the method is subsequently applied to other types of nanosystems.

This thesis is structured as follows. In Chapter 2 we introduce the micromagnetic model. In Chapter 3 we present the study of domain wall motion in nanowires with edge roughness mentioned above. Chapter 4 continues with an in-depth discussion of the two main methods for computing resonant oscillation modes in micromagnetic systems, including the implementation details in `Finmag`. This implementation is verified using a comparative case study in Chapter 5, which also highlights some of the key strengths of the eigenvalue method. In Chapter 6 we study resonant modes of domain walls in magnetic nanowires pinned at notches, and the behaviour of these modes in response to changes

[3] Another important application is in magnetic storage technology, where the read head of a magnetic hard disk drive plays the role of the sensor. Current hard disk drive technology works on the basis of *tunnel magnetoresistance* (TMR), a variant of the magnetoresistive effect in which the conducting spacer layer of the magnetoresistive stack is replaced with a thin insulator that allows electrons to tunnel between the two ferromagnetic layers.

in the nanowire and notch geometry. Chapter 7 presents the study of resonant modes in an elliptical nanodisc with applications to biosensing which was mentioned previously. We conclude with a summary and outlook in Chapter 8.

Chapter 2

The Micromagnetic Model

Micromagnetics deals with the study of magnetisation dynamics in ferromagnetic materials at a mesoscopic level, with typical length scales on the order of a few dozen nanometres up to a few micrometres. The micromagnetic model uses a phenomenological approach, ignoring the atomic structure of the material as a crystalline solid and instead modelling the magnetisation as a *continuous* vector field $\mathbf{M}$ which can be thought of as a smoothly varying average of the individual magnetic moments in the material. This continuum assumption is valid as long as the length scales of the studied systems are sufficiently larger than the atomic scale. In the standard micromagnetic model the saturation magnetisation $M_\mathrm{s} = |\mathbf{M}|$ is assumed to be constant, i.e. $\mathbf{M} = M_\mathrm{s} \cdot \mathbf{m}$ everywhere, where $\mathbf{m}$ denotes the normalised magnetisation ($|\mathbf{m}| = 1$). The assumption of constant M_s means that thermal effects are not captured in this model.

The magnetisation dynamics are governed by the so-called Landau-Lifshitz-Gilbert (LLG) equation, which is discussed in Section 2.1. It is an ordinary differential equation that describes how the magnetisation evolves over time in response to an *effective field* $\mathbf{H}_\mathrm{eff}$. This effective field arises as the variational derivative of the total micromagnetic energy in the system and determines the torque acting on the magnetisation at every point in the magnetic body.

The standard micromagnetic model includes four contributions to the total energy, which are discussed in Section 2.2. Each energy term in turn gives rise to an associated contribution to the effective field. These are described in Section 2.3. We conclude with some comments regarding the finite element discretisation in Section 2.4 which are relevant for the computation of resonant modes in magnetic nanostructures (see Section 4.3).

The fact that the micromagnetic energies operate at different length scales and compete against one another results in a rich energy landscape, often with multiple metastable equilibria. This leads to complex patterns and behaviour, such as the formation of magnetic domains, vortex structures, and hysteresis, and makes micromagnetics a particularly fruitful area for the discovery and engineering of interesting systems with useful applications (for example, magnetic logic devices, nanosensors, etc.).

Further details and derivations regarding the micromagnetic model can be found in standard textbooks such as Brown's original treatise [9] from which the modern field of micromagnetics originates, as well as more recent works, for example by Aharoni [16].

2.1 The Landau-Lifshitz-Gilbert Equation

The dynamics of the magnetisation $\mathbf{M}$ are governed by the Landau-Lifshitz-Gilbert (LLG) equation:

$$\frac{\mathrm{d}\mathbf{M}}{\mathrm{d}t} = -\gamma \cdot \mathbf{M} \times \mathbf{H}_{\mathrm{eff}} + \frac{\alpha}{M_{\mathrm{s}}} \cdot \mathbf{M} \times \frac{\mathrm{d}\mathbf{M}}{\mathrm{d}t}. \tag{2.1}$$

Here α is a dimensionless parameter, the so-called *Gilbert damping constant*. Furthermore, $\gamma = \gamma_e \, \mu_0 \approx 2.213 \times 10^5 \, (\mathrm{m})/(\mathrm{s\,A})$, where $\gamma_e \approx 1.761 \times 10^{11} \, 1/(\mathrm{s\,T})$ the electron gyromagnetic ratio and $\mu_0 = 4\pi \times 10^{-7} \, \mathrm{T\,m/A}$ the vacuum permeability.

The first term in Eq. (2.1) describes the precession of the magnetisation around the (local) effective field axis. The second term is a phenomenological damping term which describes the dissipation of energy from the system and the gradual alignment of the magnetisation with the effective field.

Since both sides in Eq. (2.1) involve the time derivative of $\mathbf{M}$, this implicit form of the LLG equation is not well suited for computer implementations. For this purpose it is more favourable to use the following mathematically equivalent[1] form (Landau-Lifshitz equation):

$$\frac{\mathrm{d}\mathbf{M}}{\mathrm{d}t} = -\gamma' \cdot (\mathbf{M} \times \mathbf{H}_{\mathrm{eff}} + \frac{\alpha}{M_{\mathrm{s}}} \cdot \mathbf{M} \times (\mathbf{M} \times \mathbf{H}_{\mathrm{eff}})), \tag{2.2}$$

where $\gamma' = \gamma/(1+\alpha^2)$. Dividing by M_{s} leads to the equivalent equation for the unit magnetisation.

$$\frac{\mathrm{d}\mathbf{m}}{\mathrm{d}t} = -\gamma' \cdot (\mathbf{m} \times \mathbf{H}_{\mathrm{eff}} + \alpha \cdot \mathbf{m} \times (\mathbf{m} \times \mathbf{H}_{\mathrm{eff}})), \tag{2.3}$$

[1] The equivalence is easily seen by substituting the right-hand side of Eq. (2.1) for the last term $\frac{\mathrm{d}\mathbf{M}}{\mathrm{d}t}$ on the right-hand side and applying the vector identity $\mathbf{a} \times (\mathbf{b} \times \mathbf{c}) = \mathbf{b}(\mathbf{a} \cdot \mathbf{c}) - \mathbf{c}(\mathbf{a} \cdot \mathbf{b})$ to the last term in the resulting equation.

In most magnetic materials the Gilbert damping constant α is small (for example, $\alpha \approx 0.01$ in permalloy). As a result, the energy dissipation happens at a much slower time scale than the precessional dynamics. This poses challenges for the numerical simulation of micromagnetic systems because it leads to stiff differential equations which require a sufficiently small step size during time integration to avoid numerical instabilities.

2.2 The Micromagnetic Energy Contributions

In the standard micromagnetic model there are four contributions to the total energy in a ferromagnetic body. These are the Zeeman energy, anisotropy energy, exchange energy and magnetostatic energy:

$$E_{\text{total}} = E_{\text{exch}} + E_{\text{anis}} + E_{\text{demag}} + E_{\text{Zeeman}}. \tag{2.4}$$

They are discussed in the following sections.

2.2.1 Zeeman Energy

The Zeeman energy is due to an externally applied magnetic field $\mathbf{H}_{\text{ext}}$ and is the simplest of the four energy terms. The local energy density is given by the expression $\mathbf{M} \cdot \mathbf{H}_{\text{ext}}$, which measures the misalignment of the magnetisation with the external field axis. The total Zeeman energy of the system is therefore given by integrating this expression over the domain of the magnetic body Ω.

$$E_{\text{Zeeman}} = -\mu_0 \cdot \int_{\Omega} \mathbf{M} \cdot \mathbf{H}_{\text{ext}} \, \mathrm{d}\mathbf{r}. \tag{2.5}$$

2.2.2 Anisotropy Energy

The anisotropy energy is due to material effects. It accounts for the fact that depending on the crystal structure of the material the magnetisation may prefer to align along certain directions over others. It has the general form

$$\int_{\Omega} \varepsilon_{\text{anis}}(\mathbf{m}) \, \mathrm{d}\mathbf{r},$$

where $\varepsilon_{\text{anis}}$ is the local anisotropy energy density, which is a function of the magnetisation direction $\mathbf{m}$. It is usually expressed as a truncated power series in the direction cosines of $\mathbf{m}$ with respect to the crystallographic axes. In the case of uniaxial anisotropy with a single easy axis $\mathbf{a}$ (with $|\mathbf{a}| = 1$) this series expansion has the following form.[2]

$$\varepsilon_{\text{anis}}(\mathbf{m}) = -K_1 \cos^2(\theta) - K_2 \cos^4(\theta) + \dots,$$

Here K_1, K_2, ... are experimentally determined anisotropy constants and θ denotes the angle between $\mathbf{m}$ and the anisotropy axis $\mathbf{a}$. In most materials the higher-order terms from K_2 onwards are negligible. Using $\cos(\theta) = \mathbf{a} \cdot \mathbf{m}$, this leads to the the following expression for the uniaxial anisotropy energy,

$$E_{\text{anis}} = -K_1 \cdot \int_\Omega (\mathbf{a} \cdot \mathbf{m})^2 \, \mathrm{d}\mathbf{r}. \tag{2.6}$$

2.2.3 Exchange Energy

The exchange energy is defined as

$$E_{\text{exch}} = A \cdot \int_\Omega (\nabla m_x)^2 + (\nabla m_y)^2 + (\nabla m_z)^2 \, \mathrm{d}\mathbf{r}. \tag{2.7}$$

Here A is the so-called exchange coupling constant. This energy contribution arises from the exchange interaction, a quantum-mechanical effect that leads to the parallel alignment of neighbouring magnetic moments. A derivation of Eq. (2.7) can be found in Aharoni's book [16, §7.1], among others. The exchange interaction is a very strong effect, but it acts only over short length scales, typically on the order of a few nanometres.

2.2.4 Magnetostatic Energy

The magnetostatic energy is due to the mutual magnetostatic interaction of the magnetic moments in the material. Also known as the demagnetising energy because it effectively reduces the overall magnetic moment of the system, it takes the form

$$E_{\text{demag}} = -\frac{\mu_0}{2} \int \mathbf{M} \cdot \mathbf{H}_{\text{demag}} \, \mathrm{d}\mathbf{r}, \tag{2.8}$$

[2] It is a theoretical fact that the anisotropy energy is symmetric with respect to the plane perpendicular to $\mathbf{a}$ so that only even powers of $\cos(\theta)$ occur in this expansion. [16]

where $\mathbf{H}_{\text{demag}}$ is the *demagnetising field*, which is the field created by all magnetic moments in the material.

All other energy terms discussed earlier are *local* functions of the magnetisation. By contrast, the magnetostatic energy depends on the *global* state of the magnetisation in the system: every magnetic moment influences every other one (of course, with the strength of the interaction decreasing with distance).

The magnetostatic interaction has the opposite effect to the exchange interaction in that the magnetostatic energy of two magnetic moments is minimised if they are aligned antiparallel instead of parallel. The combination of the facts that the magnetostatic interaction is much weaker than the exchange interaction but acts on much larger length scales is one of the primary reasons which leads to competing energy terms on the mesoscale and to the existence of magnetic domains.

2.3 The Effective Field

Let $\mathbf{m}_0$ be the magnetisation configuration in a (potentially metastable) equilibrium state. An equilibrium is characterised by the free energy functional (Eq. (2.4)) attaining a local minimum. Using variational calculus with the definitions of the energy terms given above and the constraint $|\mathbf{M}| = M_{\text{s}}$ leads to the following condition (*Brown's equation*). [16]

$$\mathbf{M}_0 \times \mathbf{H}_{\text{eff}} = 0. \tag{2.9}$$

Here the effective field is defined as follows via the variational derivative of the total energy in the system:

$$\mathbf{H}_{\text{eff}} = -\frac{1}{\mu_0}\frac{\delta E_{\text{total}}}{\delta \mathbf{m}}. \tag{2.10}$$

The effective field can be decomposed into four contributions corresponding to the individual energy terms described above. For the Zeeman and magnetostatic energy we simply recover the terms $\mathbf{H}_{\text{ext}}$ and $\mathbf{H}_{\text{demag}}$. For the anisotropy and exchange interaction this leads to the expressions

$$\mathbf{H}_{\text{anis}} = -2K_1(\mathbf{a}\cdot\mathbf{m})\cdot\mathbf{a}, \tag{2.11}$$

$$\mathbf{H}_{\text{ex}} = \frac{2A}{\mu_0}\nabla^2\mathbf{m}. \tag{2.12}$$

The effective field then is the sum of the four contributions

$$\mathbf{H}_{\text{eff}} = \mathbf{H}_{\text{ex}} + \mathbf{H}_{\text{anis}} + \mathbf{H}_{\text{demag}} + \mathbf{H}_{\text{ext}} \tag{2.13}$$

and reflects all geometric and magnetic properties of the system.

2.4 Finite Element Discretisation of the Effective Field

As explained above, in the continuum formulation the effective field is defined via the variational derivative of the micromagnetic energy. We now discuss how it is computed in the context of the finite element discretisation in `Finmag`. Given a finite element mesh with N vertices, the magnetisation is defined at the mesh nodes and can be represented as a vector (M_j) of length $3N$ (three magnetisation components at each vertex).

In principle, the effective field can be derived similarly as in the continuum case via minimisation of the total energy with respect to the individual magnetisation components M_j. However, this has two disadvantages. Firstly, the minimisation procedure requires solving a sparse linear system of equations at each time step during the simulation to determine the effective field for the current magnetisation configuration. Secondly, while the continuous versions of the exchange, anisotropy and Zeeman contribution only depend on $\mathbf{M}$ locally (i.e., changing the magnetisation at one location will not change the effective field far away), this condition is not satisfied any more for the solution for $\mathbf{H}_{\text{eff}}$ obtained in this way by solving the linear system. Therefore the numerical solution obtained in this way behaves "unphysically".

Both problems can be avoided by using the so-called "box scheme" [17, 18] which is also used in the open source micromagnetic code `Magpar`. In this approach the effective field is computed via

$$H_{\text{eff,i}} = -\frac{1}{V_i} \frac{\partial E_{\text{total}}}{\partial \mathbf{M}_i} \tag{2.14}$$

Here $V_i = \int_\Omega \eta_i \, \mathrm{d}\mathbf{r}$ denotes the volume of the mesh associated with node i of the finite element mesh (the function η_i under the integral is the "tent function" associated with node i, which has value 1 at the node itself and value zero everywhere else).

This avoids the problem of a non-local influence of the magnetisation on the effective field and also allows a more efficient computation of $\mathbf{H}_{\text{eff}}$. This method is used in various

software packages for micromagnetic simulation, including `Magpar` [17], `Nmag` [19] and `Finmag`. However, as we will see in Section 4.3 it has unfavourable consequences in the context of computing resonance modes using an eigenvalue problem derived from the effective field.

Chapter 3

Domain wall motion in perpendicular anisotropy nanowires with edge roughness

In computer simulations, it is often necessary to make simplifying assumptions, either due to limitations of the model or in order to make the simulations computationally feasible. While it is useful to study simple cases first to gain an understanding of the fundamental mechanisms, real systems will often exhibit behaviour that cannot be fully captured using such simplified techniques.

A good example related to magnetic nanosystems is given by the motion of domain walls in nanowires. Typically, in computer simulations a nanowire is modelled as a long, flat rectangular box with smooth sides. However, real nanowires inevitably exhibit imperfections stemming from the production process (e.g. nanolithography).

In this chapter we report a systematic study of field-driven domain wall motion in nanowires with edge roughness. This edge roughness is introduced by deforming the finite element mesh, and we vary the correlation length and magnitude of the roughness deformation separately. We observe the typical Walker breakdown (a phase transition from steady to oscillatory motion of the domain wall) both with and without roughness, with steady domain wall motion for applied fields below the critical Walker field $\mathbf{H}_{\mathrm{c}}$, and oscillatory motion for larger fields. The value of $\mathbf{H}_{\mathrm{c}}$ is not altered in the presence of roughness.

The edge roughness introduces a depinning field. During the transient depinning process from the initial configuration to steady domain wall motion, the domain wall velocity is significantly reduced in comparison to a wire without roughness. The asymptotic domain wall velocity, on the other hand, is virtually unaffected by the roughness, even though the magnetisation reacts to the edge distortions during the entire course of motion, both

above and below the Walker breakdown, The depinning field depends linearly on the magnitude of the edge roughness. The strongest pinning fields are observed for roughness correlation lengths that match the domain wall width.

A moving domain wall can get pinned again at some later point ('dynamic pinning'). Dynamic pinning is a stochastic process and is observed both for small fields below $\mathbf{H}_c$ as well as for fields of any strength above $\mathbf{H}_c$. In the latter case, where the domain wall shows oscillatory motion and the magnetisation in the domain wall rotates in the film plane, pinning can only occur at positions where the DW reverses direction and the instantaneous velocity is zero, i.e., at the beginning or in the middle of a positional oscillation cycle. In our simulations pinning was only observed at the beginnings of cycles, where the magnetization is pointing along the wire.

The contents of this chapter have been published in a JPCM special issue on "Domain wall dynamics in nanostructures". [20]

3.1 Introduction

To realise potential storage devices, such as racetrack memory [15], nanowires with low intrinsic pinning as well as nanowires with intended pinning sites for individual domain walls are required. Real nanowires tend to exhibit a roughness at their boundaries, which introduces additional complexity. It is reasonable to distinguish between the surface roughness originating from the deposition process and the edge roughness that stems from the lithography.

The influence of the latter has been studied for in-plane anisotropy and soft materials [21], where a vortex-mediated breakdown localised at the sample edges was found and it turned out that the edge roughness can significantly affect the vortex nucleation and annihilation process that determines the behavior of the domain wall. The influence of surface roughness on the domain wall propagation process is also prominent in perpendicular magnetic anisotropy media (PMA) and has been studied, e.g. using the magneto-optical Kerr effect [22–24]. It has been found that as the wire width decreases, the magnetic domain wall dynamics change from elastic creep in two dimensions to a particle-like stochastic behaviour in one dimension.

Often, pinning sites are desired and can be realised by geometric constrictions to create local confining potentials that act as pinning sites for individual domain walls [25–28].

As an alternative, the local modification of magnetic properties by ion irradiation, e.g. by implanting Cr ions, is suitable to induce pinning sites [29, 30]. In this case, a variation of the wire geometry on the nanoscale is not required. The introduction of such magnetic soft spots is attractive due to lower requirements on the lithography in comparison to geometric constrictions on the nanoscale, a smaller distribution of properties due to parallel processing during implantation, and fine tunability of the pinning potential via the chromium ion fluence.

It is important to understand the influence of the usually undesired edge roughness to support work on domain wall propagation in wires without constrictions, with constrictions, and with other intentionally created pinning centres. The role of disorder in in-plane domain wall motion has been studied theoretically, including the effect of edge roughness [21] and surface roughness [31] on the domain wall velocity, the interplay of extrinsic pinning with the critical current or field at which the domain wall is depinned and starts to move [32], the influence of thermal excitations and roughness on domain wall motion [33], and domain wall velocity fluctuations due to edge pinning centers [34].

Surface roughness has been modelled through introduction of a set of pinning centers for the domain wall [32, 34]. To model edge roughness in the context of finite difference simulations, complete simulation cells have been removed from the micromagnetic sample edge [33], introducing disorder at the length scale of the cell size (of the order of $5\,\mathrm{nm}$). Other works use a Voronoi tessellation to model grains in the material, then remove grains from the sample edge, and map this modified sample edge boundary onto the finite-difference grid [21, 35]. The grains are adequately resolved if they are larger than the cell size. To model surface roughness in thin films with finite difference simulations, one can also vary the saturation magnetisation in each finite difference cell instead of varying the height of the cells [31]. The length scale of the surface roughness in this model cannot be smaller than the cell size but can be chosen to be longer by varying the saturation magnetisation slowly in space.

In this work, we study the effect of edge roughness which originates from the lithographic sample fabrication process on the domain wall propagation in perpendicular magnetic anisotropy media. A finite-element spatial discretisation of the nanowire and its edge roughness is used. In Sec. 3.2 we introduce the simulation model, geometry and materials, roughness model and comment on the automated data analysis used. We report simulation results for a smooth nanowire in Sec. 3.3, before extending the simulation to include edge roughness in Sec. 3.4. We close with a summary in Sec. 3.5.

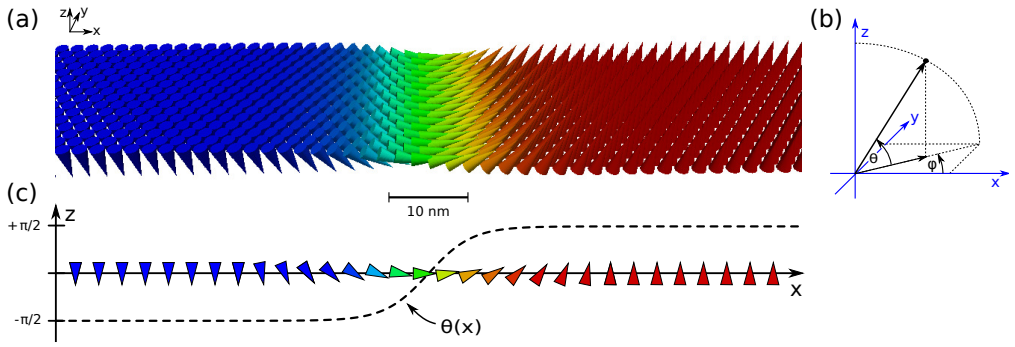

Figure 3.1: (a) Initial Néel wall configuration, after relaxation. (b) Convention of spherical coordinate system. (c) Domain wall profile.

3.2 Method

All simulations are carried out using the micromagnetic simulation package `Nmag` [19, 36] developed at the University of Southampton, which employs a hybrid finite element/boundary element method approach. For our purposes, an advantage over finite difference-based discretisation is that this allows us to model the edge roughness of the system more accurately using a tetrahedral mesh than would be possible with cuboidal cells (see Fig. 3.2).

3.2.1 Geometry and Material

The system under consideration is a PMA nanowire with rectangular cross-section and dimensions $1000\,\mathrm{nm} \times 20\,\mathrm{nm} \times 5\,\mathrm{nm}$ in x, y and z-axis directions, respectively. The extremal corners have coordinates $(0\,\mathrm{nm}, 0\,\mathrm{nm}, 0\,\mathrm{nm})$ and $(1000\,\mathrm{nm}, 20\,\mathrm{nm}, 5\,\mathrm{nm})$. We have deliberately chosen the wire width to be rather small so that the system can be treated as effectively one-dimensional since the exchange interaction keeps the magnetisation almost constant in y- and z-direction. Figure 3.1 shows the initial configuration for which we set the magnetisation to point down (in negative z-direction) at the left end of the wire (*i.e.* at $x = 0$) and up at the other end, with a domain wall located between the two uniform domains. This two-domain system with domain wall is well described by two parameters: (i) the DW position and (ii) the azimuthal angle ϕ of the magnetisation at the DW center. We use spherical coordinates to characterise the orientation of the magnetisation at the centre of the DW, as shown in Fig. 3.1, where θ is the vertical angle between $\mathbf{M}$ and the x-y-plane (polar angle), and ϕ is the horizontal angle between $\mathbf{M}$ and the x-axis (azimuthal angle). In what follows, we are particularly interested in the

value of ϕ at the center of the DW, as this – together with the DW position – captures the DW state. The angle ϕ will frequently be referred to as the *magnetisation angle* of the DW.

Inspired by experimental studies [37], we use the effective material parameters of a multilayered Co/Ni nanowire with saturation magnetisation $M_\mathrm{s} = 6.8 \times 10^5\,\mathrm{A\,m^{-1}}$, exchange coupling $A = 1.3 \times 10^{-11}\,\mathrm{J\,m^{-1}}$ and uniaxial anisotropy constant $K_1 = 3.8 \times 10^5\,\mathrm{J\,m^{-3}}$. The resulting exchange length is $\sqrt{A/K_1} = 5.85\,\mathrm{nm}$, the Gilbert damping parameter used is $\alpha = 0.032$ [38].

3.2.2 Simulation Stages

Each simulation consists of two stages: a relaxation phase and the main simulation of the domain wall dynamics. In the relaxation phase we initialise the magnetisation $\mathbf{M}$ in the nanowire to a Néel-like pattern, with $M_y = 0$ everywhere, *i.e.*, the magnetisation rotates in the x-z-plane (as shown in Fig. 3.1). The z-component M_z is initialised to $\tanh\left(\sqrt{K_1/A} \cdot (x - 200)\right)$, which describes the domain wall pattern for a system when the demagnetising field is neglected, with the DW center located at $x = 200\,\mathrm{nm}$.[1] This is then relaxed until it reaches a metastable state as illustrated in Fig. 3.1, which takes into account exchange, anisotropy and demagnetisation fields. The relaxation is carried out by numerical integration of the Landau-Lifshitz-Gilbert equation. A large damping coefficient, $\alpha = 1.0$, is used to speed up the relaxation. The relaxed system exhibits a Néel domain wall, as shown in Fig. 3.1, to avoid surface charges on the edges which would be associated with a Bloch wall.

Once equilibrium is reached the second stage is started. The damping is set to the realistic value, $\alpha = 0.032$, and a constant external field $\mathbf{H}_\mathrm{ext}$ is applied along the z-axis. The response of the magnetisation is then computed for $20\,\mathrm{ns}$. Every $0.1\,\mathrm{ns}$ the domain wall position (along the x-axis) is computed by finding the zero-crossing of θ along the nanowire axis. This is done by probing θ at 2000 auxiliary nodes along this line and determining the two adjacent nodes where a sign change occurs. Then θ is interpolated linearly between these adjacent nodes to determine the position of the zero-crossing.[2]

[1] Control simulations suggest that boundary effects are negligible further than $\approx 150\,\mathrm{nm}$ away from the ends of the nanowire. In this work no data of domain walls outside this range was used.

[2] The determination of the zero-crossing uses a Python function which is given to the simulation framework with the instruction to call it every $0.1\,\mathrm{ns}$ during the computation, which avoids storing all the field data for later postprocessing. The integration of the micromagnetic simulation tool into an existing programming language thus simplifies data capture and analysis here [39].

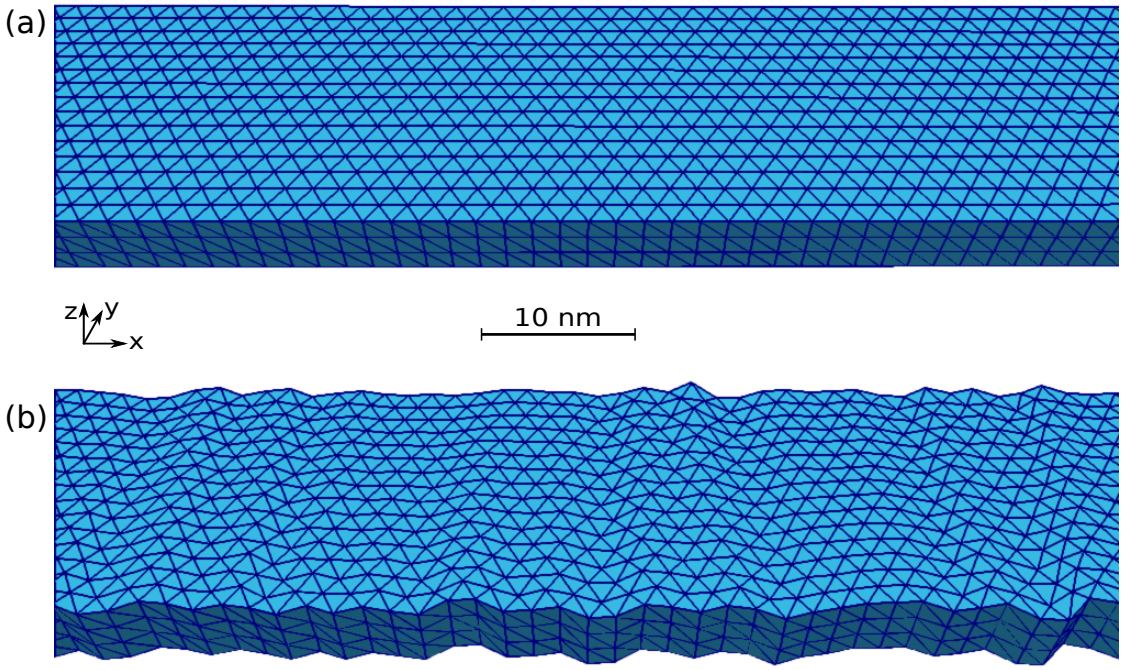

Figure 3.2: (a) Smooth mesh. For this mesh there are three layers of tetrahedra in z-direction representing the film thickness of $5\,\mathrm{nm}$ and 15 layers in y-direction extending $20\,\mathrm{nm}$. Only a part of the mesh of the wire is shown in the x-direction. (b) Rough version of the same mesh (with correlation length $c = 2\,\mathrm{nm}$ and distortion amplitude $d = 0.4\,\mathrm{nm}$).

Moreover, at the position of the DW center the magnetisation angle ϕ is recorded and both the domain wall position and magnetisation angle, together with the current time step, are written to an output file for subsequent analysis.

3.2.3 Roughness Model

In this work, we use a finite element-based discretisation of space. This allows to model rough edges explicitly using a distorted finite element mesh. We start from a smooth tetrahedral mesh as shown in Fig. 3.2 (a) with dimensions $1000\,\mathrm{nm} \times 20\,\mathrm{nm} \times 5\,\mathrm{nm}$, which is subsequently distorted at front and rear edges as shown in Fig. 3.2 (b). In the following, the term *edge* or *edge surface* always refers to the two surfaces of dimensions $1000\,\mathrm{nm} \times 5\,\mathrm{nm}$ at the the long edges of the wire parallel to the x-z plane.

The overall distortion process works as follows. We first construct a 'distortion function' $f(x)$. This function specifies the amount by which each node lying on the front edge

surface of the mesh (where $y = 0\,\mathrm{nm}$) is displaced in y-direction, as a function of the x-coordinate of the node. Analogously, the nodes at the rear edge surface (where $y = 20\,\mathrm{nm}$) are displaced using a second, independently constructed distortion function $g(x)$ so that both edges of the mesh are distorted differently. The positions of the internal mesh nodes are then rescaled in order to fit between the new distorted sides.

The distortion functions f and g are constructed as follows. First we pick equidistant positions x_i along the x-axis. These are just auxiliary entities and completely independent of the actual mesh nodes. The distance between two neighbouring auxiliary nodes is referred to as the *correlation length* c of the distortion. Next, random values $f(x_i)$ and $g(x_i)$ are assigned to each position x_i, chosen from a Gaussian distribution with mean 0 and standard deviation d, which is referred to as the *distortion amplitude* of the roughness or simply as the *roughness level*. Finally, the random values $f(x_i)$ and $g(x_i)$ are interpolated smoothly to obtain the continuous distortion functions $f(x)$ and $g(x)$. The whole process is illustrated in Fig. 3.3. In order to make the randomisation reproducible, it is possible to specify a seed for the internal random number generator. This allows us for a given c to produce meshes with the same 'shape of roughness' but different roughness amplitudes: the distortion functions of these meshes are just scaled versions of each other. We introduce the distortion functions f and g, rather than displacing the mesh nodes on the edges randomly and thus independently of each other, in order to be able to control the roughness correlation length independently of the actual mesh discretization (assuming that the edge length of the tetrahedra for the chosen mesh discretisation is smaller than the correlation length c).

The effective roughness length scale, which we define as the average width of the peaks and troughs of the rough edge, or – equivalently – the distance between adjacent local minima in $f(x)$ and $g(x)$, is larger than the correlation length c as visible in Fig. 3.3 (b). Statistical analysis of this effective roughness length scale for a range of disorder functions $f(x)$ and $g(x)$ shows that the effective roughness length is given by $\approx 2.76c$ (see Fig. 3.3 (d)).

There are several conceivable ways of modelling edge roughness, including locally varying material parameters or Voronoi cell approaches, as mentioned in Sec. 3.1. The method used here models the kind of roughness associated with irregularities in the sample geometry originating from electron beam lithography, due to the remaining jitter of the electron beam around a zero position. The amount of this jitter is modelled by the roughness amplitude d. Depending on the speed of the beam along the edge this jitter is 'spread out' over a certain distance, which is modelled by the correlation length c. We

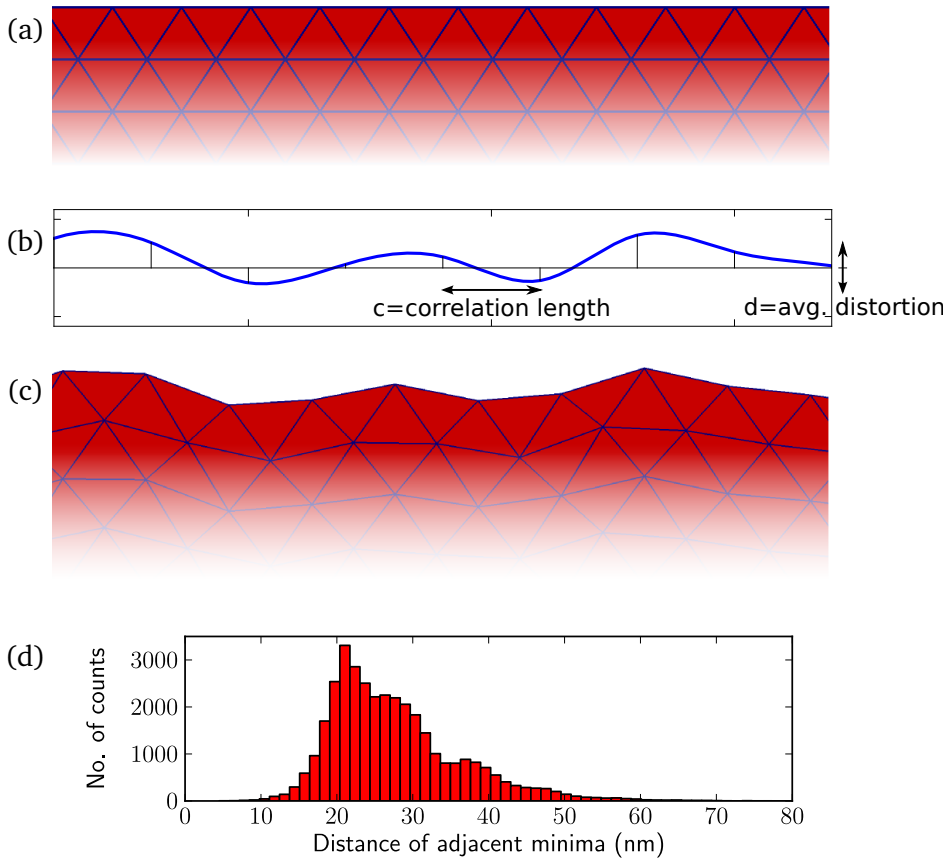

Figure 3.3: Illustration of the edge distortion process, showing a top view of the rear edge of the nanowire. (a) Original mesh. (b) Construction of the distortion function g with certain correlation length and distortion amplitude. (c) The mesh after distortion with g. The contour of the distorted mesh follows the outline of g. (d) Distribution of the distances between adjacent local minima. The data was gathered from a collection of 1000 different distortion functions, each produced with a different randomisation seed at the fixed correlation length $c = 10\,\mathrm{nm}$. The mean distance is $27.6\,\mathrm{nm} = 2.76 \times c$, which defines the effective roughness length scale.

note, however, that there is a second source of roughness due to the chemical process of transferring the latent image of the nanowire after exposure, which involves rather long-chain molecules. Unless special care is taken this is usually the dominant source of roughness.

3.2.4 Data Analysis

We have carried out over 24,000 simulations where we systematically vary the external field strength H, roughness correlation length c, and roughness amplitude d. For each configuration, *i.e.* combination of the three parameters (H, c, d), we carry out one simulation run. Each simulation run produces an output file containing data recorded every $0.1\,\mathrm{ns}$ between $0\,\mathrm{ns}$ and $20\,\mathrm{ns}$. For each of the time steps the corresponding computed domain wall position and the magnetisation angle ϕ inside the domain wall are recorded.

The main observable we are interested in for each configuration is the DW velocity $v_\mathrm{x}(t)$, which is derived from the DW position $r_\mathrm{x}(t)$ as a function of time. All other quantities, such as the depinning field for a given roughness level, can be computed from this. Our simulation results of a smooth nanowire in Sec. 3.3 and a nanowire with edge roughness in Sec. 3.4 agree qualitatively with Walker's prediction [12] that there is steady domain wall motion for applied fields $\mathbf{H}$ below a critical field $\mathbf{H}_\mathrm{c}$, and oscillatory motion for larger applied fields. We need to distinguish between these two regimes to apply appropriate methods to compute the domain wall velocity. To do this, we use the angle ϕ as the criterion: in the steady-motion regime the magnetisation angle ϕ approaches an asymptotic value $|\phi| < \frac{\pi}{2}$, whereas in the oscillatory regime the magnetisation inside the DW keeps precessing indefinitely, so that $|\phi|$ grows to infinity.

3.2.4.1 Mean velocity

The simplest way to compute the domain wall velocity is to subtract the initial domain wall position $r_\mathrm{x}(t_0)$ at time t_0 from the final position $r_\mathrm{x}(t_\mathrm{f})$ at time t_f, and to divide by the time it took to travel that distance:

$$v_\mathrm{x}^\mathrm{mean} = \frac{r_\mathrm{x}(t_\mathrm{f}) - r_\mathrm{x}(t_0)}{t_\mathrm{f} - t_0} \tag{3.1}$$

Later analysis in Sections 3.3 and 3.4 shows, however, that the initial depinning process of a domain wall is qualitatively different from the subsequent domain wall motion: during the depinning process, the domain wall increases its velocity from zero to an asymptotic value for fields below the Walker breakdown, or shows asymptotic periodic behaviour for fields above the Walker breakdown. As this increase does not happen instantaneously, the transient process will reduce the mean velocity in the steady-motion regime if computed using (3.1). The decrease will depend on the simulated time: the longer we run the simulation, the smaller the reduction of $v_{\mathrm{x}}^{\mathrm{mean}}$ due to the initial transient, and the smaller the difference between mean and asymptotic velocities. Moreover, for oscillatory motion there can be some variation in the mean velocity as computed using (3.1) depending on how much of the last oscillation cycle is completed when the simulation exits (but this is purely a computational artifact due to the chosen stopping time t_{f}).

3.2.4.2 Asymptotic velocity

We thus use a different method to compute the domain wall velocity, which eliminates the reduction of $v_{\mathrm{x}}^{\mathrm{mean}}$ due to the initial transient and removes artefacts due to incomplete oscillation cycles. To distinguish from the mean velocity, we refer to this as the asymptotic velocity.

In the oscillatory case we identify the time and position of the DW at the beginning of each oscillation cycle, *i.e.* when the angle ϕ is a multiple of π. Using a least-squares approximation we then fit a line through these positions as a function of time, and compute the velocity as the slope of the fitted line as shown in Fig. 3.4 (a).[3] The initial depinning transient is negligible for external fields above $\mathbf{H}_{\mathrm{c}}$ and therefore does not affect the calculation of the asymptotic velocity in this regime.

For applied fields below the Walker breakdown, the domain wall shows non-oscillatory motion. To eliminate the initial transient from the data analysis in this regime, we identify the first time t_1 and domain wall position $r_{\mathrm{x}}(t_1)$ from which onwards the plot of domain wall position as function of time shows an approximately linear dependence. We then compute the velocity as

$$v_{\mathrm{x}}^{\mathrm{asymptotic}} = \frac{r_{\mathrm{x}}(t_{\mathrm{f}}) - r_{\mathrm{x}}(t_1)}{t_{\mathrm{f}} - t_1} \tag{3.2}$$

[3] Contrary to the usual convention, in this paper we plot time t along the vertical axis and the DW position x along the horizontal axis. This is consistent with the orientation of the nanowire in figures 3.1, 3.2, 3.7, and allows better comparison between plots in the same figure. With this convention the velocities of the domain walls are actually given by the *inverse* slope of the trajectories in these figures. Hence a steeper line indicates a slower domain wall since it moves less far along the x-axis during the course of the simulation.

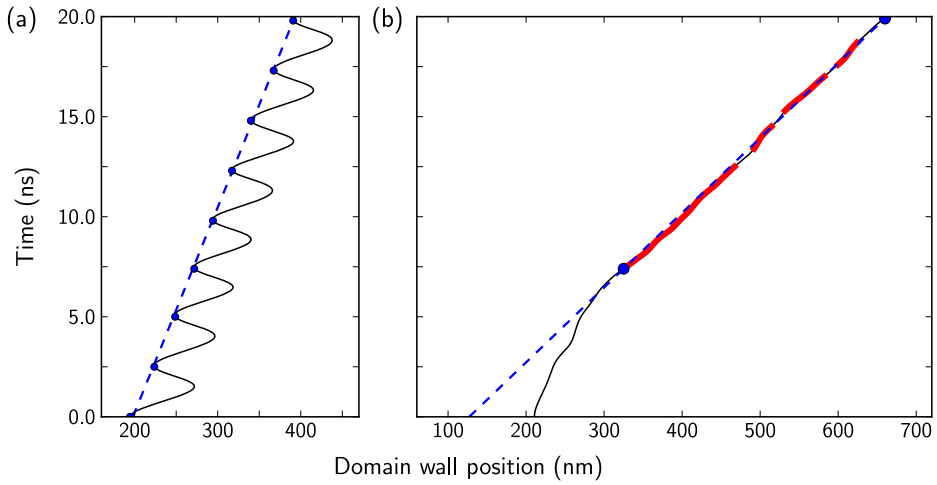

Figure 3.4: Illustration of the computation of the asymptotic domain wall velocity. (a) In the oscillatory case, the positions and times for the beginning of each oscillation cycle are identified, and a line is fitted through them (dashed blue line). The line's slope provides the velocity. (b) In the steady-motion regime below the Walker breakdown field, we identify the beginning of the first straight segment in the plot (thickened red part), and take the position and time of this point, together with the last position and time, to compute the asymptotic velocity. The interpolated points for both cases are marked with blue dots in both plots.

We identify segments of the $r_x(t)$ function where the DW exhibits approximately straight motion by using a Savitzky-Golay filter [40, Ch. 14.8]. This computes for each recorded time step the second derivative of a smoothed version of the trajectory, which gives an indication of the curvature of the trajectory at that point. By discarding points where the second derivatives are above a given threshold we identify one or more segments where the DW exhibits approximately straight motion as shown in Fig. 3.4 (b) (segments marked with thick red lines).

3.2.4.3 Pinning

Using these tools, we can also identify when a domain wall (i) is never depinned, or (ii) gets pinned again after having moved a certain distance (dynamic pinning; see Fig. 3.9 and Fig. 3.10 below for examples). In case (i), we record the domain wall velocity as zero for both v_x^{mean} and $v_x^{\mathrm{asymptotic}}$. In case (ii), we compute the mean velocity v_x^{mean} using (3.1) but record no velocity for $v_x^{\mathrm{asymptotic}}$ as the motion is too irregular to estimate the asymptotic velocity.

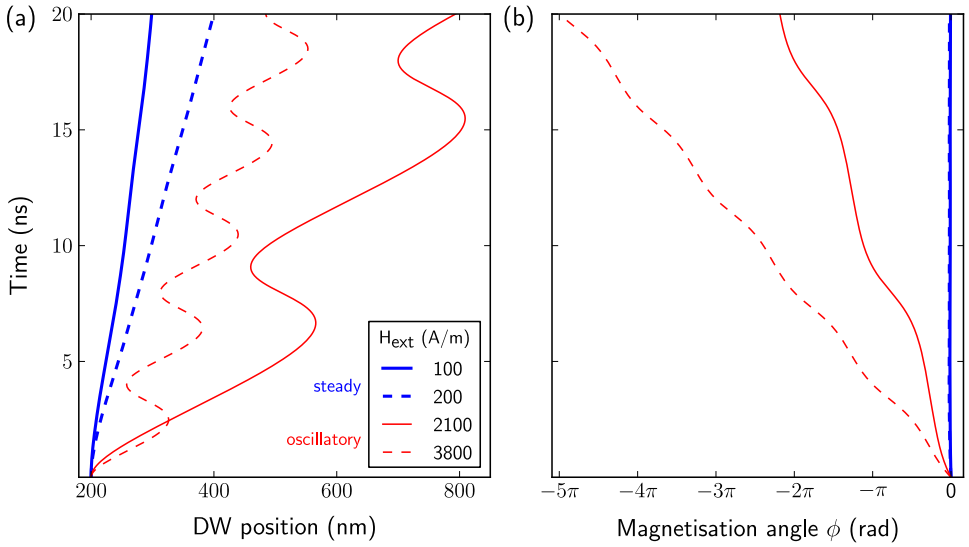

Figure 3.5: (a) Sample DW trajectories for different applied fields H: steady (thick blue lines) and oscillatory (thin red lines). (b) The corresponding magnetisation angles ϕ.

3.3 Smooth Nanowire

In the following we give a summary of the dynamics of perpendicular domain walls in a smooth nanowire in external fields. These results present the reference for the rough nanowire studied in Section 3.4.

The external field $\mathbf{H}_{\text{ext}}$ is applied along the negative out-of-plane z-direction (see Figure 3.1). The domain wall then moves to the right, *i.e.* along the positive x-direction. This behaviour can be understood in terms of energy minimisation: the domain wall moves to the right to allow the left domain to grow. Indeed, a wider left domain corresponds to an increased alignment of the magnetisation to the applied field and a reduction of the Zeeman and total energy.

Figure 3.5 (a) shows the position of the domain wall against time for four different applied field strengths. We see that the domain wall starts to move as the field is applied, in all the considered cases. For the two lower fields (blue thick lines), the motion is 'steady', with the velocity increasing as the applied field is increased. In contrast, for the two higher applied fields (thin red lines) the motion of the domain wall is oscillatory. The domain wall moves backwards and forwards as a function of time, but moves further forward than backward in each cycle, leading to a net positive velocity. The frequency of the oscillation depends on the external field strength, and is higher for the larger

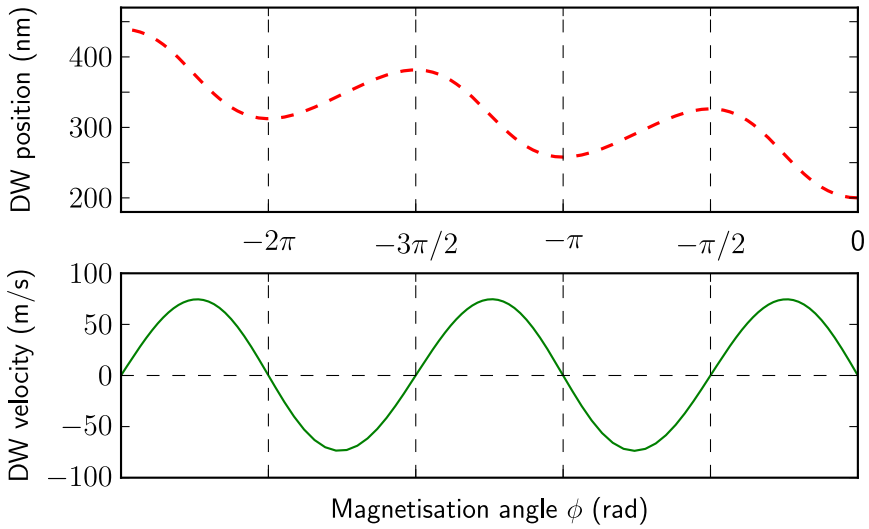

Figure 3.6: Domain wall position (top) and domain wall velocity (bottom) as a function of magnetisation angle ϕ for $H = 3.8\,\mathrm{kA\,m^{-1}}$ in the oscillatory regime. The figure should be read 'from right to left' because the angle ϕ increases in the negative direction during the DW motion.

external field (dashed thin line), while the net velocity is lower for the larger external field.

Figure 3.5 (b) shows the magnetisation angle at the DW centre, ϕ, against time for the same simulations considered in Fig. 3.5 (a). For the steady motion curves (thick lines), ϕ changes from zero at time $t = 0$ to a very small negative value and then remains constant. In the oscillatory regime (thin lines), ϕ behaves differently: it grows continuously as a function of time, and grows faster for stronger applied fields. For the steady-motion curves considered in Fig. 3.5 the angle is small because the fields are weak; for fields close to $\mathbf{H}_\mathrm{c}$ the asymptotic angle can become quite large until at $\mathbf{H}_\mathrm{c}$ it reaches $-\frac{\pi}{2}$ and 'tips over' so that it can keep growing grow continuously.

Figure 3.6 combines the data from the two previous plots and shows domain wall position (top) and velocity (bottom) as a function of the magnetisation angle ϕ for the $H = 3.8\,\mathrm{kA\,m^{-1}}$ curve in Fig. 3.5. The figure should be read 'from right to left' because the angle ϕ increases in the negative direction during motion. We can see that the domain wall position increases as ϕ grows from 0 to $-\frac{\pi}{2}$ and that the velocity remains positive in this interval. From $\phi = -\frac{\pi}{2}$ the domain wall moves backwards until $\phi = -\pi$, at which point the cycle repeats. We note that ϕ changes by $-\pi$ (not -2π) while the domain wall position completes an oscillation cycle, so that the magnetisation in

the domain wall centre points in the negative x direction at the end of the positional cycle (*i.e.* $\phi = -\pi$) whereas it was pointing in the positive x direction at the beginning. After one more positional cycle the angle also returns to the original position, so that the DW position completes two cycles during a full rotation of the magnetisation angle.

Figure 3.7 shows a set of corresponding magnetisation configurations for different magnetisation angles ϕ. We use these figures to interpret the oscillatory motion. Starting from Fig. 3.7 (a), the applied external field forces the magnetisation to precess so that ϕ changes from 0 to a negative value. The configuration in Fig. 3.7 (a), resembles a Néel wall which has no surface charges on the front and back edge of the wire. However, once the magnetisation in the domain wall starts to rotate in the x-y plane, surface charges start to appear on the sides of the wire as in Fig. 3.7 (b). These increase the demagnetisation energy of the system, and energy has to be found to allow this change. This energy is provided through the Zeeman term by growing the left domain in the wire: both magnetisation and applied field point in the negative z direction in this domain. Growing the domain on the left means that the domain wall needs to move to the right, *i.e.* towards larger x values. The further ϕ grows towards $-\frac{\pi}{2}$, the further the domain wall needs to move.

For weak applied fields, the growing demagnetisation field can counteract the precession torque from the applied field and the system settles into a steady state with fixed angle ϕ in which the domain wall moves continuously towards larger x-values (thick lines in Fig. 3.5). For large applied fields, however, ϕ eventually reaches $-\frac{\pi}{2}$, corresponding to snapshot 3.7 (c) where the magnetisation is pointing in the negative y direction, which is best visible in the centre of the domain wall. While ϕ increases further from $-\frac{\pi}{2}$ to $-\pi$, the surface charges reduce and thus the demagnetisation energy is reduced. This is compensated by the domain wall moving back to the left to shrink the domain on the left that is aligned with the applied field, as shown in Fig. 3.7 (d). When ϕ reaches $-\pi$, the surface charges have disappeared and the cycle will start again in a mirror-symmetric way, explaining why the domain wall moves backwards and forwards twice while ϕ increases from 0 to -2π.

If there was no damping in this system (*i.e.* $\alpha = 0$), the domain wall would move back to its starting position when ϕ reaches multiples of π. It is the damping term that allows to release energy from the system, and this results in a net motion of the domain wall in the positive x direction due to the applied field in the negative z direction. We also note that

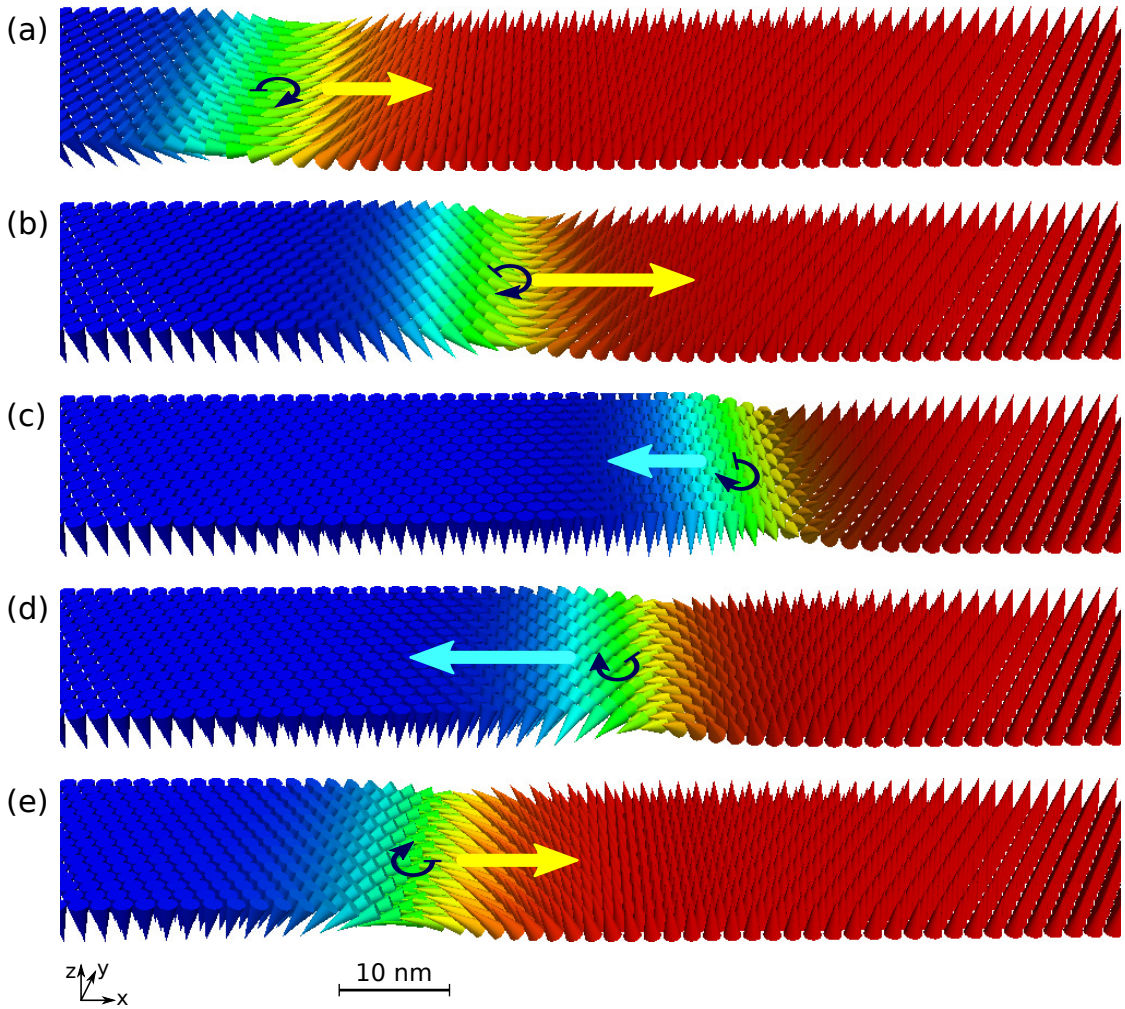

Figure 3.7: Snapshots of a domain wall moving in a smooth nanowire ($\mathbf{H}_{\mathrm{ext}} = 9\,\mathrm{kA\,m^{-1}} > \mathbf{H}_{\mathrm{c}}$). The pictures show half a rotation of the first oscillation, with time increasing from top to bottom. (a) The initial configuration, cf. Fig. 3.1. (b) The domain wall moves to the right as the magnetisation angle ϕ precesses around the vertical axis. (c) At $\phi = \frac{\pi}{2}$ the DW reverses direction and (d) starts moving to the left. (e) At $\phi = \pi$ another reversal of direction occurs and the DW moves to the right again. The same procedure repeats itself with two more direction reversals at $\phi = 3/2\pi$ and $\phi = 2\pi$ (both not shown) until the angle ϕ has completed a full turn and the DW starts its third oscillation. Large superimposed arrows indicate velocity of the domain wall. The thin curly arrows indicate the direction of rotation of the magnetic moments in the domain wall.

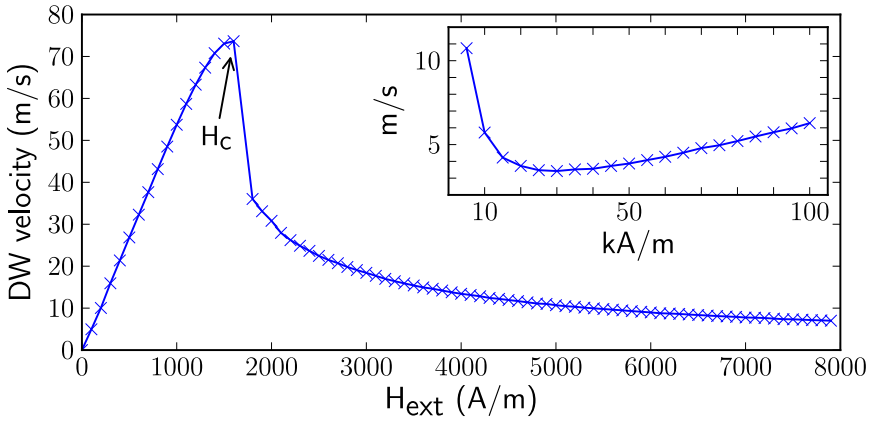

Figure 3.8: Domain wall velocity as a function of $\mathbf{H}_{\mathrm{ext}}$. The separation into two regimes, one above and one below the Walker breakdown, is clearly distinguishable. The inset shows the increase of the velocity for very strong fields $\gg \mathbf{H}_{\mathrm{c}}$ (note the different scale).

if the simulations are carried out without consideration of the demagnetising field, then the oscillations in the domain wall position cannot be observed.

We thus find two different domain wall motion regimes: steady motion for applied fields H below the so-called Walker breakdown field $\mathbf{H}_{\mathrm{c}}$ and oscillatory motion for $H > \mathbf{H}_{\mathrm{c}}$ [12]. Figure 3.8 shows the DW velocity as a function of the external field. In a smooth system as simulated here, *i.e.* in the absence of any domain wall pinning due to roughness, the domain wall starts to move if any non-zero external field is applied. In line with Walker's prediction the domain wall velocity increases with the applied field up to the Walker breakdown field $\mathbf{H}_{\mathrm{c}}$ at which the velocity reaches its maximum. For larger applied fields, the domain wall velocity decreases. Sample simulations with field strengths much larger than $\mathbf{H}_{\mathrm{c}}$ have shown that the DW velocity assumes a minimum around $H = 30\,\mathrm{kA\,m^{-1}}$ and increases again for even stronger external fields.

3.4 Nanowire with edge roughness

In this section we introduce edge roughness to the wire geometry and repeat the simulations of field driven domain wall motion from Section 3.3 in the presence of this disorder. The relaxation stage of the simulations (Section 3.2.2) allows the domain wall to settle into an energetically favourable position inside a constriction caused by the edge roughness (which typically deviates slightly from the initial position in the smooth case). As a result, the system needs a certain applied field strength to depin the domain wall from

this location and cause the domain wall to move. In this section we investigate how the edge roughness affects the domain wall motion (Section 3.4.1), the domain wall velocity (Section 3.4.2) and the depinning field (Section 3.4.3).

3.4.1 Domain wall motion

We discuss the effect of roughness on domain wall motion for applied fields H below (Section 3.4.1.1) and above (Section 3.4.1.2) the Walker breakdown field $\mathbf{H}_\mathrm{c}$ separately.

3.4.1.1 Influence of the roughness below the Walker breakdown

Figure 3.9 (a) shows some typical domain wall trajectories in nanowires with different strengths of edge roughness in a fixed external field $H = 0.6\,\mathrm{kA\,m^{-1}}$. One additional trajectory for a different field strength $H = 0.5\,\mathrm{kA\,m^{-1}}$ (dotted curve) was included to illustrate dynamic pinning.[4] The roughness correlation length is fixed at $c = 4\,\mathrm{nm}$ whereas the roughness magnitude varies between $d = 0\,\mathrm{nm}$ (smooth wire) and $d = 0.06\,\mathrm{nm}$; for clarity, the curves for some intermediate values of d have been omitted in the figure. The same randomisation seed was used in all cases so that the shape of the edge distortions is the same and only the amplitude d varies. The particular edge roughness profile used is displayed at the top of the figure: we see the distortions introduced by the roughness functions $f(x)$ and $g(x)$ as explained in Section 3.2.3. For visibility, the vertical extents of the distortions f(x) and g(x) are scaled up in this plot. As mentioned previously, we plot the domain wall position x along the horizontal axis. This allows us to compare the domain wall trajectories with the roughness profile that the domain wall centre is located in.

The trajectory in the smooth wire (dashed curve) shows the same characteristics as the ones discussed in Section 3.3: it takes the domain wall $\approx 3\,\mathrm{ns}$ to reach its full speed, during which time the magnetisation angle ϕ increases and approaches its asymptotic value as can be seen in Fig. 3.9 (b). Once this is reached so that the surface charges on the sides of the wire balance the torque which the external field exerts on the magnetisation inside the DW, the DW moves along the nanowire with constant velocity.

[4] We note that this dynamic pinning site is located at a constriction of the nanowire which at first glance appears to be less pronounced than others along the wire. However, its width almost exactly matches the size of the DW so that it exhibits a strong pinning effect, as discussed in Section 3.4.3.

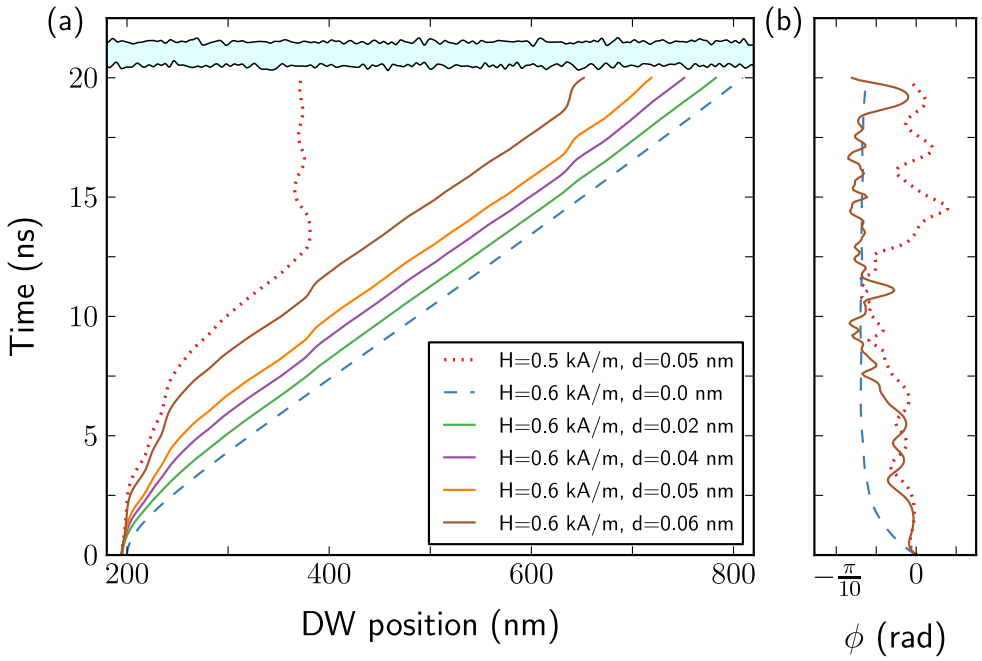

Figure 3.9: (a) Sample trajectories in a constant external field $\mathbf{H}_{\text{ext}} = 0.6\,\text{kA}\,\text{m}^{-1} < \mathbf{H}_{\text{c}}$ for varying roughness magnitudes d. The roughness correlation length is fixed at $c = 4\,\text{nm}$. One additional trajectory for a different field strength $H = 0.5\,\text{kA}\,\text{m}^{-1}$ (dotted curve) was included to illustrate dynamic pinning. The particular edge roughness profiles used in these simulations is shown as an inset towards the top: the roughness has been scaled up along the vertical axis to make the profile visible more easily. (b) Time evolution of the magnetisation angle ϕ for selected trajectories $d = 0\,\text{nm}$ (dashed) and $d = 0.06\,\text{nm}$ (solid) at $\mathbf{H}_{\text{ext}} = 0.6\,\text{kA/m}$ and $d = 0.05\,\text{nm}$ at $\mathbf{H}_{\text{ext}} = 0.5\,\text{kA/m}$ (dotted).

The trajectories for non-zero roughness show two marked differences in comparison to the smooth system. Firstly, it takes a longer time for the domain wall to depin and for the angle ϕ to approach its asymptotic value. The effect is stronger for greater roughness magnitude d as shown by solid lines in Fig. 3.9 (a). For $d = 0.02\,\mathrm{nm}$ the effect is small and the DW reaches its full speed after $\approx 4\,\mathrm{ns}$. For $d = 0.06\,\mathrm{nm}$ this initial phase takes $\approx 8\,\mathrm{ns}$ — almost triple the time of the domain wall in the smooth nanowire ($d = 0\,\mathrm{nm}$). For $d = 0.06\,\mathrm{nm}$, we can see from Figures 3.9 (a) and (b) that the DW reacts to the edge distortions between $x = 200\,\mathrm{nm}$ and $x = 250\,\mathrm{nm}$ during this initial transient.

The second difference between the trajectories in the smooth and the rough nanowires is that we observe local decelerations of the DW during the motion in the presence of edge roughness. In the examples shown in Fig. 3.9 (a) these manifest themselves as bumps in the curves and occur at $x \approx 380\,\mathrm{nm}$ and $x \approx 640\,\mathrm{nm}$. For the lower roughness magnitudes ($d = 0.02\,\mathrm{nm}$, $0.04\,\mathrm{nm}$) these are hardly noticeable, whereas for $d = 0.05\,\mathrm{nm}$ and $0.06\,\mathrm{nm}$ they become visible. However, for the largest part of the motion the DW couples very weakly to the edge distortions and the curve is effectively straight (corresponding to constant velocity) with the velocity being virtually the same as in the smooth nanowire in these sections between the decelerations. If the driving field is too weak then the DW can get dynamically pinned during one of these decelerations. This is illustrated by the dotted curve in Fig. 3.9 (a).

In order to gain a better understanding of these two phenomena it is helpful to look at the magnetisation angle ϕ inside the DW. Figure 3.9 (b) shows the time evolution of ϕ as the DW progresses along the nanowire. In the smooth system (dashed curve) ϕ gradually increases from zero until it reaches its asymptotic value and then remains constant. For $d = 0.06\,\mathrm{nm}$ (solid line) the angle ϕ shows a much more erratic behaviour as a function of time as the magnetisation reacts to the edge distortions in an attempt to minimise the surface charges at the sides. The value of ϕ for the domain wall in the wire with $d = 0.06\,\mathrm{nm}$ approaches the asymptotic value of ϕ in the smooth system at $t \approx 8\,\mathrm{ns}$. For larger values of t the angle ϕ shows small, apparently random deviations from this value. There are two exceptions at $t \approx 11\,\mathrm{ns}$ and $t \approx 19\,\mathrm{ns}$ where $|\phi|$ gets close to zero, resulting in two larger spikes in the dashed curve. These correspond to the two local decelerations visible in Fig. 3.9 (a).

The dotted curve shows the time evolution of ϕ in the slightly weaker field $H = 0.5\,\mathrm{kA\,m^{-1}}$, corresponding to the dotted trajectory in Fig. 3.9 (a). The way in which ϕ reacts to the edge distortions during the first half of the simulation is virtually identical to $H =$

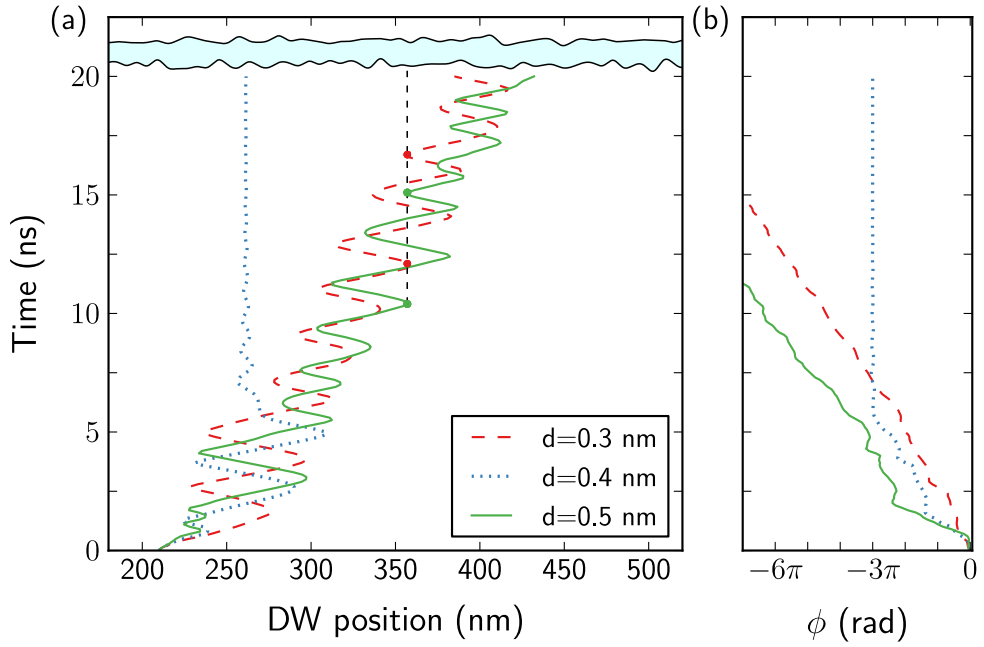

Figure 3.10: (a) Sample trajectories in a constant external field $\mathbf{H}_{\text{ext}} = 5.75\,\text{kA m}^{-1}$ for varying roughness magnitudes d. The roughness correlation length is fixed at $c = 4\,\text{nm}$. The inset at the top shows the profile of the nanowire with roughness as in Fig. 3.9. (b) Time evolution of the magnetisation angle ϕ for these trajectories.

$0.6\,\text{kA m}^{-1}$, except that the changes happen more slowly due to the lower driving field. Thus the first half of the dotted curve in Fig. 3.9 (b), before $t = 12\,\text{ns}$, is just a slightly vertically stretched version of the solid curve. The DW reaches the pinning site $x \approx 380\,\text{nm}$ at $t \approx 11\,\text{ns}$ in the stronger field (solid curve) and at $t \approx 13\,\text{ns}$ in the weaker field (dotted curve). In the first case the field is strong enough to push the DW past the pinning site, which only results in a small spike of the angle towards zero. For the weaker field, on the other hand, the DW gets pinned and ϕ slowly relaxes back into the zero-position where the magnetisation points along the nanowire axis.

3.4.1.2 Influence of the roughness above the Walker breakdown

Figure 3.10 (a) shows three trajectories of domain walls in an external field $H = 5.75\,\text{kA m}^{-1} > \mathbf{H}_{\text{c}}$. The roughness correlation length $c = 4\,\text{nm}$ is fixed and only the roughness magnitude d varies between $0.3\,\text{nm}$ and $0.5\,\text{nm}$. All trajectories show the oscillatory motion typical of fields $H > \mathbf{H}_{\text{c}}$. In the absence of roughness (*i.e.* $d = 0.0\,\text{nm}$), all three curves would coincide.

The trajectory for the smallest roughness magnitude $d = 0.3\,\mathrm{nm}$ (dashed red curve) is the most regular of the three and quite similar to the trajectory in the smooth wire (not shown to avoid clutter in the plot). For the next larger value of roughness magnitude $d = 0.4\,\mathrm{nm}$ (dotted blue curve) the edge distortions around $x = 230\,\mathrm{nm}$ result in one short cycle with two quick direction reversals during the first $2\,\mathrm{ns}$. Subsequently, the DW performs two larger position oscillation cycles before it gets caught by a pinning site at $x = 261\,\mathrm{nm}$ and relaxes into a metastable state at this location. For the largest value shown in the plot, $d = 0.5\,\mathrm{nm}$ (solid green curve), the domain wall reacts even more strongly to the edge roughness around $x = 230\,\mathrm{nm}$, this time performing four quick direction reversals during the first $2\,\mathrm{ns}$, before it continues in a fashion similar to the dashed curve ($d = 0.3\,\mathrm{nm}$).

The x-positions where the domain wall reverses direction during the oscillations in each of the trajectories are not arbitrarily distributed along the nanowire. Rather, the direction reversals nearly always fall into a constriction of the wire. The dashed black vertical line at $x = 357\,\mathrm{nm}$ indicates one example where four direction reversals at different time steps in two trajectories (marked with green and red dots) fall into the same constriction. The same applies to virtually all other cycles in the three curves. This shows that the DW couples rather strongly to the edge distortions at the left and right turning points of the domain wall position cycles. Thus individual cycles can be lengthened or shortened as the DW reacts to the roughness, which accounts for the alterations in the trajectories visible for higher roughness strengths. By contrast, the edge distortions do not have a noticeable influence on the motion in the middle of a cycle.

For $d = 0.4\,\mathrm{nm}$ the DW gets dynamically pinned at $x = 261\,\mathrm{nm}$, whereas pinning does not occur for the smaller roughness magnitude $d = 0.3\,\mathrm{nm}$ nor the larger one $d = 0.5\,\mathrm{nm}$. Similarly, other simulation runs at a fixed roughness magnitude d have shown that it is possible for the DW to get dynamically pinned in an external field of a certain strength while no pinning occurs for higher or lower fields.

We explain these observations by studying how the magnetisation angle ϕ in the domain wall couples to the edge distortions in the nanowire in the next section.

3.4.1.3 Discussion

Dynamic pinning occurs where the total energy of the domain wall can be reduced by moving it into the pinning position. The domain wall carries a certain exchange and anisotropy energy which grow proportionally with the length (extension in y-direction)

of the domain wall. The domain wall energy can thus be reduced if it moves to locations where the edge distortions on both sides of the nanowire collude to form a constriction, and thus reduce the length of the domain wall. For example, the domain wall for $d = 0.4\,\mathrm{nm}$ that is shown as a dotted line in Fig. 3.10 (a) is dynamically pinned at $x \approx 261\,\mathrm{nm}$, and we see a constriction in the roughness profile which is shown as an inset in the top of the figure.

Above the Walker breakdown, the angle ϕ keeps growing, which reflects the rotation of the magnetisation in the x-y-plane during the oscillatory motion of the domain wall; the displacement of the domain wall and the change in ϕ are coupled as described in Section 3.3 and visible in Fig. 3.6. For $\phi = n\pi$ with $n = 0, \pm1, \pm2, \ldots$, the domain wall magnetisation points along the wire and there are no surface charges along the edges associated with the domain wall, so the demagnetisation energy of the domain wall is minimal. Conversely, for $\phi = (n + \frac{1}{2})\pi$ the magnetisation points in $\pm y$ direction, and this maximises the demagnetisation energy associated with the domain wall. Between those extrema the energy varies continuously. The increase in demagnetisation energy due to ϕ changing from, say, 0 to $\frac{\pi}{2}$ is large in comparison to the energy fluctuations caused by the edge roughness, such as the decrease in energy due to a reduced domain wall length in a constriction.

Therefore the domain wall only interacts with the roughness where the energy reduction caused by a constriction is of a magnitude comparable to the change in the demagnetisation energy associated with a small displacement of the domain wall, or equivalently a small change in ϕ. The response of the demagnetisation energy to a change in ϕ is smallest around extrema, *i.e.* around $\phi = n\pi$ (minima) and $\phi = (n + \frac{1}{2})\pi$ (maxima). For intermediate values of ϕ, the energy change due to roughness is insignificant in comparison to the dominating demagnetisation energy change.

This interpretation explains why the turning points of the positions of the domain wall tend to coincide with constrictions in the roughness pattern: at the left-hand turning points we have $\phi = n\pi$ and at the right-hand turning points $\phi = (n + \frac{1}{2})\pi$, so that the DW can couple to the edge distortions at these points in the motion. Figure 3.10 (a) shows selected turning points of the oscillating domain wall position and illustrates how these align with the effective constrictions in the roughness of the wire as indicated by the vertical dashed black line.

The same argument suggests that dynamic pinning above the Walker breakdown can only occur for $\phi \approx n\pi$ and $\phi \approx (n + \frac{1}{2})\pi$. In our simulations, we have only observed dynamic pinning where $\phi \approx n\pi$. An example for this dynamic pinning above the Walker

breakdown is shown in Fig. 3.10 (a) for $d = 0.4\,\mathrm{nm}$ as a dotted line. The domain wall shows oscillatory motion up to $t \approx 5\,\mathrm{ns}$, and subsequently gets pinned at $t \approx 7\,\mathrm{ns}$. The corresponding dotted line in Fig. 3.10 (b) shows that $\phi = -3\pi$, *i.e.* $\sin(\phi) = 0$, when the domain wall reaches the pinning site. The requirement that ϕ must be close to $n\pi$ or $(n + \frac{1}{2})\pi$ for dynamic pinning to occur above the Walker breakdown explains why the domain wall $d = 0.4\,\mathrm{nm}$ in Fig. 3.10 (a) can pass through the pinning site $x \approx 260\,\mathrm{nm}$ repeatedly without being pinned (three times for $t < 5\,\mathrm{ns}$).

Below the Walker breakdown, there is competition between the external field that drives the domain wall forward and the effective potential that the domain wall experiences due to the roughness. If the roughness exhibits a constriction, this reduces the domain wall length and energy. The constriction can be interpreted as a pinning potential well that the domain wall experiences if we use a model where the domain wall is a particle that experiences a spatially varying potential energy. It depends on the depth and width of this potential well whether the applied field can push the domain wall through it or whether pinning takes place. An increasing external field reduces the pinning strength. This is in line with our observations that pinning becomes less likely for larger fields H below the critical Walker breakdown field.

We hypothesise that in addition to the length (in y-direction) of a constriction in the roughness profile, it is also its width (in x-direction) which contributes to how effective a constriction is as a dynamic pinning centre: constrictions of width comparable to the domain wall width are most effective (see discussion in Section 3.4.3), but the detailed shape of the constriction is likely to be important, too.

The discussion above shows that in the steady and oscillatory regimes the pinning process, although guided by the same underlying principles, leads to rather different phenomena. For $H < \mathbf{H}_\mathrm{c}$ the probability of the DW being pinned decreases with increasing external field H since higher fields lead to a larger asymptotic value of ϕ, whereas for $H > \mathbf{H}_\mathrm{c}$ there is no simple relationship between the strength of the field and the pinning probability since the latter depends on the intricate interaction of the constantly precessing magnetisation and the edge distortions. Our simulation results have shown that pinning above the Walker breakdown occurs in the whole range up to the highest simulated fields ($10\,\mathrm{kA\,m^{-1}}$) and appears to be more common for higher fields than for fields just above $\mathbf{H}_\mathrm{c}$. This seemingly counter-intuitive observation can be explained by the fact that the oscillations of the DW position are much shorter for large fields H than for small fields. For large fields, the domain wall position trajectory overlaps with itself (see the quickly oscillating curves in figures 3.5 (a) and 3.10 (a)). Thus the DW passes the same

location in the nanowire more often, with different angles. This makes it more likely to reach a pinning site with $\phi = n\pi$ or $\phi = (n + \frac{1}{2})\pi$ and thus increases the pinning probability.

3.4.2 Influence of the roughness on the domain wall velocity

The domain wall trajectories in Fig. 3.10 (a) show that, although individual oscillation cycles can be significantly altered at different roughness levels d, the changes mostly average out over time. Thus the mean velocities are quite similar for all roughness strengths. This is in line with the observation which we made earlier for $H < \mathbf{H}_\mathrm{c}$ in Fig. 3.9 (a), where the asymptotic velocities are also virtually identical for all trajectories. In this section we study the influence of the roughness on the domain wall velocity in more detail.

As discussed in Section 3.2.4, there are two distinct ways of computing the velocity: (i) the *mean velocity*, which uses the distance travelled during the simulated time based on the first and last point of the trajectory; (ii) the *asymptotic velocity*, which attempts to estimate the asymptotic velocity by disregarding the depinning process and, for fields above the Walker breakdown, removes artefacts due to incomplete oscillation cycles at the end of the simulation. We discuss both methods, putting our main emphasis on the second one.

Figure 3.11 (a) shows plots of the asymptotic domain wall velocity (Section 3.2.4.2) as a function of the applied field for various roughness magnitudes d. Figure 3.11 (b) shows the corresponding mean velocity (Section 3.2.4.1). The correlation length of the roughness is $c = 6.0\,\mathrm{nm}$ for all data shown while the roughness amplitude varies between $d = 0.0\,\mathrm{nm}$ (smooth wire) and $d = 0.09\,\mathrm{nm}$ in steps of $0.01\,\mathrm{nm}$. The same randomisation seed was used to produce the roughness profile in all cases so that increasing d does not change the shape of the edge roughness but only increases the vertical size of the distortions. For each value of d the external field was increased from $0\,\mathrm{A\,m^{-1}}$ up to $3000\,\mathrm{A\,m^{-1}}$ in steps of $100\,\mathrm{A\,m^{-1}}$ and a simulation was run for each applied field value in order to compute the DW velocities. In a second phase the external field interval containing the depinning field was discretised in finer steps of $10\,\mathrm{A\,m^{-1}}$ to obtain a better resolution.

We define the depinning field $\mathrm{H_{depin}}$ as the smallest field that is just strong enough to drive the DW away from its original position into which the system has been relaxed

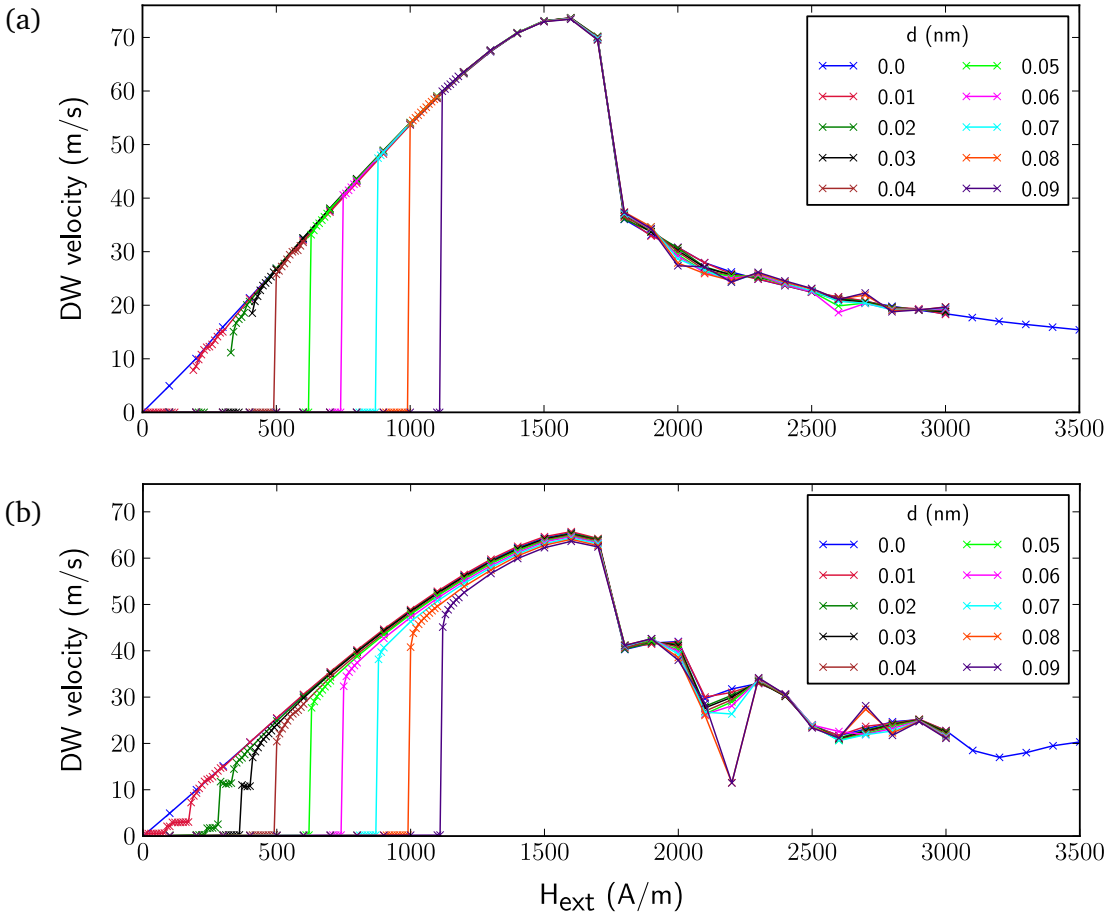

Figure 3.11: (a) Asymptotic domain wall velocity, computed using the method described in Section 3.2.4.2, as a function of applied field H. Each line corresponds to one roughness magnitude d. (b) Corresponding mean domain wall velocity, computed using method described in Section 3.2.4.1.

during the first stage of the simulation, irrespective of whether the DW gets pinned at a later stage or not. The depinning field is a function of the correlation length c and roughness magnitude d that define the edge roughness: $\mathrm{H_{depin}} = \mathrm{H_{depin}}(c, d)$. For the discussion of Fig. 3.11, c is kept fixed at $6\,\mathrm{nm}$.

The line for $d = 0\,\mathrm{nm}$ in Fig. 3.11 corresponds to a nanowire without roughness, and there is no depinning field defined: any finite applied field will result in domain wall motion. For increasing roughness magnitude we see that the domain wall remains pinned in its original position (corresponding to zero velocity) up to the critical depinning field, which increases with increasing d. Once the external field H exceeds $\mathrm{H_{depin}}$ for a given roughness magnitude d, the DW starts moving.

For a couple of small values of d, such as $d = 0.02\,\mathrm{nm}$ or $0.03\,\mathrm{nm}$, the DW mean velocity appears to increase 'in leaps' (Fig. 3.11 (b)), which is due to the DW being pinned dynamically for small fields so that the mean velocity is reduced. This is not visible in the asymptotic velocity (Fig. 3.11 (a)) where these data points have been removed as in these cases the asymptotic velocity is not defined (see Section 3.2.4.3). However, for larger d such as $d = 0.04 - 0.09\,\mathrm{nm}$ the asymptotic velocity appears, on the scale of this graph, to jump immediately from zero to the velocity of the smooth system. For stronger applied fields up to the critical Walker field $\mathbf{H}_\mathrm{c} \approx 1.7\,\mathrm{kA\,m^{-1}}$ the asymptotic DW velocities are virtually identical for all roughness strenghts. Above the Walker breakdown there is some slight variation, but the discrepancies are small ($\approx 10\%$ for the largest deviations, e.g. for $H = 2.0\,\mathrm{kA\,m^{-1}}$).

The plot of the domain wall mean velocities in Fig. 3.11 (b) shows that there is a somewhat gradual increase in the mean velocity once $\mathbf{H}_\mathrm{ext}$ exceeds $\mathrm{H_{depin}}$ and that up to the Walker field $\mathbf{H}_\mathrm{c}$ the DW velocity in rough nanowires always stays below the value of the smooth wire. The larger the roughness magnitude d, the further does the mean velocity stay below the domain wall velocity of the smooth wire. It appears as if larger roughness reduces the velocity, but the comparison with the asymptotic velocities (Fig. 3.11 (a)) reveals that it is the initial depinning process that gets increasingly slower with increasing roughness magnitude d (see Section 3.4.1.1). As the mean velocity is a time average of the domain wall velocity, this initial slowdown is visible. We note that the reduction of the mean velocity due to the depinning will decrease if the domain wall motion is simulated for longer periods of time. Unless we want to study the effect of the depinning process on the mean velocity, we prefer the asymptotic velocity as an observable because it is independent of the simulated time. However, the mean velocity can be a useful observable for applications where the DW only moves over a limited distance,

for example between engineered notches in racetrack memory [15] and similar applications.

Above the critical Walker field, the mean velocity curves in Fig. 3.11 (b) exhibit a seemingly erratic behaviour. Even the one for the smooth system ($d = 0.0\,\mathrm{nm}$) shows a kind of undulation which the other curves more or less follow. To illustrate this more clearly, the curve for the smooth system has been extended up to $H = 3.5\,\mathrm{kA\,m^{-1}}$. This behaviour can be explained as follows. Since the DW motion is oscillatory, the end point of the trajectory can vary significantly depending on where last oscillation is cut off when the simulation exits. With the exit time of the simulation remaining constant at $20\,\mathrm{ns}$ but the oscillations becoming shorter for increasing $\mathbf{H}_{\mathrm{ext}}$, the cut-off point varies significantly and also jumps backward and forward, leading to the undulating values of the velocity within each curve in Fig. 3.11 (b). The two outliers for $H = 2.2\,\mathrm{kA\,m^{-1}}$ indicate that the DW was dynamically pinned for these two roughness levels, which affects the mean velocity but is filtered out by our method to compute the asymptotic velocity.

The observation that the asymptotic velocity in the presence of roughness coincides with the domain wall velocity without roughness is in agreement with the data and discussion in sections 3.4.1.1 and 3.4.1.2: Figures 3.9 (a) and 3.10 (a) illustrate that even though there are perturbations in the trajectories – local decelerations below $\mathbf{H}_{\mathrm{c}}$ and alterations of the oscillations above $\mathbf{H}_{\mathrm{c}}$ – the asymptotic velocities are effectively the same as in the smooth nanowire even for higher roughness amplitudes.

Figure 3.11 shows that the critical Walker breakdown field is the same for all roughness strengths, which was observed in all other performed simulation runs as well. This is in contrast to a similar study of in-plane domain walls by Min et al.[31], where an increase of the critical field (combined with a slightly decreased peak DW velocity) was observed for higher roughness magnitudes. Similarly, Nakatani et al.[21] also observe a suppression of the Walker breakdown for in-plane domain walls, due to the fact that the formation of an antivortex (which absorbs most of the torque exerted by the external field, thus leading to a slowdown of the DW) is inhibited by the edge roughness. The reason why in our case no change in the critical Walker field is observed is because our nanowire is much narrower, leading to effectively one-dimensional behaviour of the magnetisation inside the DW without internal degrees of freedom.

We have discussed two different ways to analyze data from the time dependent simulations to compute (i) the mean velocity, and (ii) the asymptotic velocity. Depending on the experimental context, either entity may be of interest: for domain wall motion in very short nanowires, inclusion of the depinning time as in the mean velocity calculation

may be desired. If the simulation is meant to simulate a system where the depinning time is irrelevant (because the wire is very long) but matters in the simulation (because the simulated wire is not so long), then the asymptotic velocity may be a better measure.

3.4.3 Influence of the roughness on the depinning field

In the study of Fig. 3.11, where the roughness correlation length is $c = 6\,\mathrm{nm}$, we have noted that the depinning field $\mathrm{H}_{\mathrm{depin}}(c, d)$ increases as a function of roughness magnitude d. In this section, we analyse this dependence quantitatively for varying correlation lengths c. The corresponding simulation results are gathered in Fig. 3.12. Each of the curves displays the dependence of the depinning field $\mathrm{H}_{\mathrm{depin}}$ on the roughness magnitude d for a fixed roughness correlation length c. The data shows that the depinning field has an approximately linear dependence on the roughness magnitude d for all values of c. We denote the constant of proportionality in this linear relationship by β_c, so that $\mathrm{H}_{\mathrm{depin}}(c, d) = \beta_c \cdot d$. Thus β_c is a measure of the effective pinning strength of the edge roughness for a given roughness correlation length c, and given by the slope of the lines in Fig. 3.12. We use a least-squares fit to determine the value of β_c for each line, omitting the data points for $0.01 \leq d \leq 0.09$ to avoid a bias.

Figure 3.13 shows how β_c varies as a function of c. The data points marked with a cross and connected by a solid line show the slopes of the ten lines that are plotted in Fig. 3.12. The dashed line shows corresponding results that have been averaged over four different sets of simulation runs (*i.e.* using four different random seeds for the domain wall roughness functions, and then repeating all simulations required to obtain the β_c's). Both curves show low values for small and large c and a maximum between at $c = 7\,\mathrm{nm}$ (solid line) and $c = 9\,\mathrm{nm}$.

The largest influence of the roughness on the DW motion is expected if the characteristic length scale of the edge distortions is of the same order as the domain wall width: for very small correlation lengths c the roughness is at a scale too small to be noticed by the DW, whereas for very large values of c the wire edge appears locally flat to the DW. The characteristic domain wall width is taken as $\pi\sqrt{A/K_1}$ [41, 42], which is $18.4\,\mathrm{nm}$ for our material parameters. The effective roughness length scale for a given parameter c is on the order of $2.76\,c$ as shown in Section 3.2.3. Matching of the effective roughness length scale with the domain wall width should thus occur where $c = \pi\sqrt{A/K_1}/2.76 \approx 6.7\,\mathrm{nm}$.

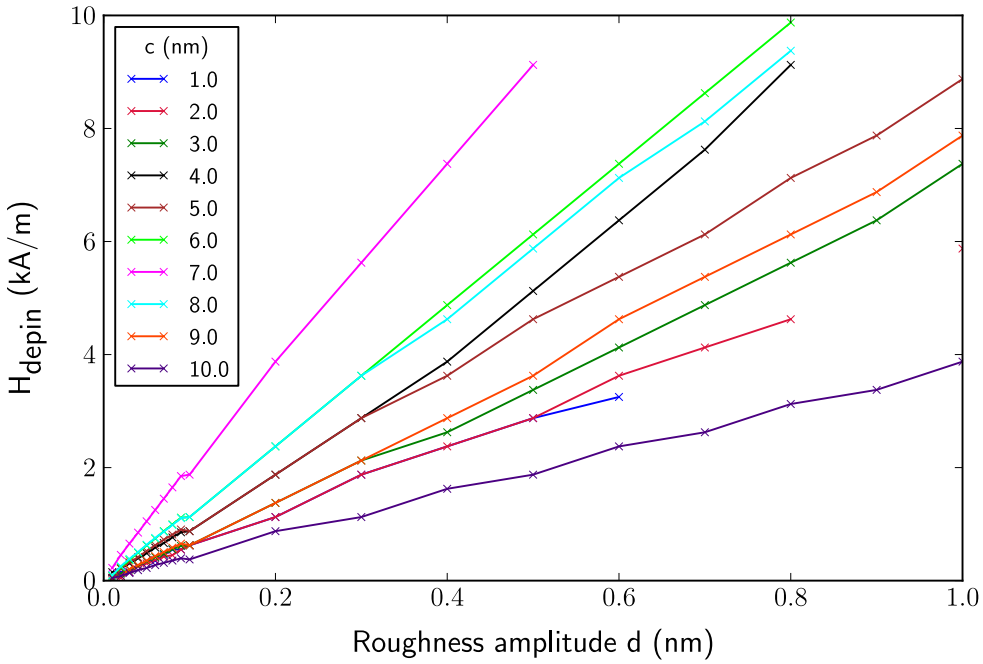

Figure 3.12: Depinning field H_{depin} as a function of the roughness amplitude d, for different correlation lengths c.

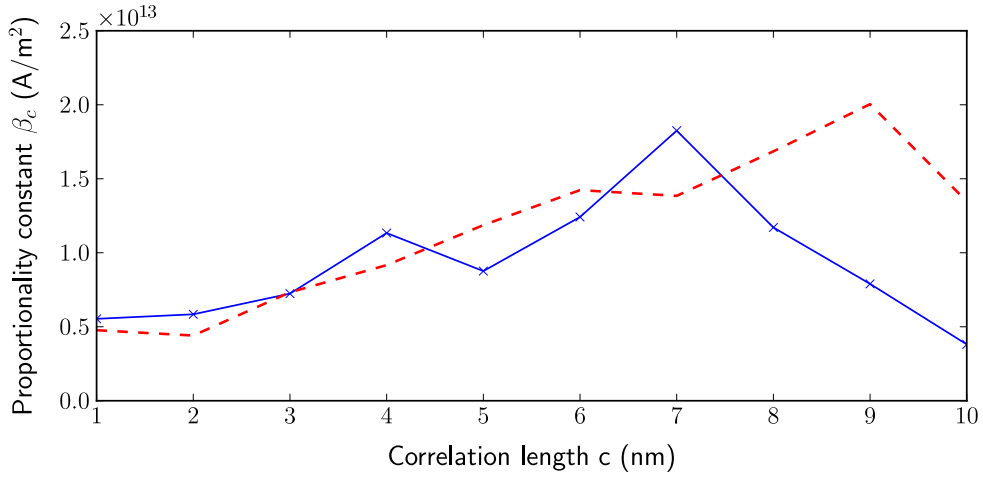

Figure 3.13: Proportionality constants β_c describing the dependence of the depinning field on the roughness level d for each correlation length c. The solid line corresponds to Fig. 3.12; the dashed line represents values averaged over four runs with different roughness shapes.

This is compatible with the data shown in Fig. 3.13 where the most effective pinning is found for c in the range $7\,\mathrm{nm}$ to $9\,\mathrm{nm}$.

Finally, focusing on the range of values which β_c takes for different roughness correlation lengths c, we note that by matching the effective roughness length scale with the domain wall width, the pinning effect can be increased significantly (approximately a factor of 5 for the data shown here).

3.5 Summary

We have studied the dynamics of field-driven domain walls in perpendicular magnetic anisotropy (PMA) nanowires with added edge roughness. We used a finite-element based roughness model which allows systematic exploration of the roughness configuration space using two parameters: (i) the roughness length scale c and (ii) the roughness magnitude d (Section 3.2.3).

The dynamics of a domain wall moving in a smooth nanowire was studied first in order to have a reference point for the rough systems. The typical Walker breakdown was observed, with the domain wall showing steady motion below the critical Walker field $\mathbf{H}_\mathrm{c}$ and oscillatory motion above $\mathbf{H}_\mathrm{c}$. In the smooth system the DW dynamics can be understood in terms of the precession of the magnetisation angle ϕ inside the domain wall.

In the nanowire with edge roughness, the Walker breakdown occurs at the same critical applied field $\mathbf{H}_\mathrm{c}$ as in the smooth nanowire, due to the fact that the system studied here is effectively one-dimensional. This is in contrast to results seen in other studies of in-plane domain walls in wider nanowires (which allow internal degrees of freedom of the DW), where the presence of edge roughness can suppress the Walker breakdown until much larger fields.

While in the smooth system the DW moves for any non-zero applied field, with added edge roughness the domain wall remains pinned up to a critical depinning field $\mathrm{H}_\mathrm{depin}$ which increases with increasing roughness magnitude d. For fields $H > \mathrm{H}_\mathrm{depin}$ the roughness affects the DW trajectories. In the steady-state regime below the Walker breakdown the roughness leads to a significantly prolonged initial depinning process and introduces local decelerations in the DW motion, resulting in sporadic distortions

of the trajectory which otherwise remains largely unchanged (Fig. 3.9 (a)). In the oscillatory regime the individual DW cycles can be markedly altered in size and shape (Fig. 3.10 (a)).

The presence of edge distortions can also lead to dynamic pinning during the DW motion. This is a process which is stochastic in nature. We find that dynamic pinning above the Walker breakdown is only likely to happen when the magnetisation angle ϕ is aligned with, or perpendicular to, the long wire-axis, as these are the points in the trajectory where the domain wall couples most strongly to the roughness distortions. Somewhat counterintuitively, this means that dynamic pinning above the Walker breakdown is more likely to happen for *stronger* fields because these result in faster and shorter oscillation cycles so that the DW has more opportunity to interact with the edge roughness profile at the beginning and end of a cycle.

We studied the influence of the roughness on the domain wall velocity, and computed two different observables: the mean velocity and the asymptotic velocity. The results have shown that in a nanowire with edge roughness the mean velocity of the domain wall during the simulation can be significantly lower than in the smooth system (Fig. 3.11 (b)). This slowdown occurs for fields slightly above the depinning field and is the result of the prolonged initial depinning process in the presence of rough edges (Fig. 3.9 (a)). However, the asymptotic DW velocity, which ignores the initial depinning, is essentially unaltered by the presence of roughness (Fig. 3.11 (a)), in spite of the noticeable influence of the roughness on the DW trajectories. In contrast to the mean velocity observable, the data obtained for the asymptotic velocity does not depend on the length of the simulated time.

Finally, we studied the dependence of the depinning field on the roughness parameters in our model. We find that $\mathrm{H}_{\mathrm{depin}}$ increases approximately linearly with the roughness amplitude d, which controls the vertical size of the edge distortions. We showed that the effectiveness of pinning increases considerably if the width of the roughness peaks and troughs correlates with the domain wall width.

Chapter 4

Resonant Modes in Magnetic Nanosystems

Oscillations and resonances are ubiquitous in nature, and micromagnetic systems are no exception. This is evident from the LLG equation (Eq. (2.1)): its first term describes a continuous oscillation around the magnetic field axis due to Larmor precession. Whenever one studies a system with oscillating parts, it makes sense to study its normal modes because these tell us how the system can be efficiently excited or destabilised out of a local equilibrium state using external driving forces (for example, oscillating magnetic fields).

The term "normal mode" refers to an oscillation pattern where all components of the system under consideration oscillate with the same frequency, and thus at a fixed relative phase relation with respect to each other. A prototypical example is given by coupled harmonic oscillators, such as a series of masses connected with ideal springs obeying Hooke's force law ($F = k\Delta x$). In this example the restoring force depends linearly on the perturbation Δx from an equilibrium state and the resulting equations of motion lead directly to a set of to oscillatory solutions at different frequencies – the normal modes of the system.
For a general system, in the vicinity of a local equilibrium the restoring force will still be approximately linear.[1] As a consequence, if the perturbation from the equilibrium state is small, the dynamics can be studied through the *linearised* equations of motion and described approximately as a superposition of normal mode oscillations.

This insight makes normal modes a powerful tool applicable to many different situations also in a micromagnetic context. For example, the peak power frequencies in a spin-torque nano-oscillator (STNO) are determined by its resonance frequencies, and

[1] The reason for this is that at an equilibrium state the energy has a local minimum and can therefore locally be written as a quadratic function in Δx; thus the restoring force, which is the derivative of the energy, depends linearly on Δx in the vicinity of the equilibrium.

understanding these resonances is crucial for the design of STNOs suitable for applications, e.g. by maximising the power output. In later chapters we present several studies of resonant modes in magnetic nanosystems. In this chapter we start with the theoretical foundations.

Section 4.1 introduces the two main approaches to computing normal modes in micromagnetic systems – the *ringdown method* and the *eigenvalue method* – with a discussion of the specific advantages and drawbacks of each. While the ringdown method can be used with virtually any micromagnetic framework, the eigenvalue method requires a special implementation. A key contribution of this work was to implement the eigenvalue method in the micromagnetic software `Finmag`, developed at the University of Southampton, and apply it to the study of resonant modes in different kinds of magnetic nanosystems. The main focus of subsequent sections will therefore be on the eigenvalue method.
Section 4.2 explains the mathematical background for the eigenvalue method. We discuss how to linearise the LLG equation and how to formulate the resulting linearised equation as an eigenvalue problem which can be solved numerically to compute the resonance frequencies and oscillation patterns of the micromagnetic system under study.
There are multiple choices to make regarding the numerical solution of the resulting eigenvalue problem. Section 4.3 discusses these alternatives, the specific problems encountered in the context of a finite element micromagnetic code and the choices made in our implementation as well as their implications for efficiency and performance.
Later, in Chapter 5, we will present a case study to illustrate the differences between the ringdown and eigenvalue method with a real-world example. This also provides a numerical verification of the implementation of the eigenvalue method in `Finmag`.

4.1 Approaches to Computing Resonant Modes in Magnetic Nanosystems

This section introduces the two main methods for computing resonant modes in magnetic nanosystems: the ringdown method and the eigenvalue method. It provides a high-level overview of these methods and discusses their particular characteristics. These will later be illustrated with a comparative case study (see Chapter 5).

Some of the material in Section 4.1.1 is based on recent a joint publication [43] which proposes a micromagnetic standard problem for ferromagnetic resonance (FMR) simula-

tions, in order to facilitate the implementation of the ringdown method and verification of results.

4.1.1 The Ringdown Method

4.1.1.1 Overview

The traditional way to compute normal modes of a micromagnetic system is the so-called *ringdown method*. [44, 45] The idea is to apply a small excitation – for example, a short constant or time-varying field pulse – to slightly perturb the system out of its equilibrium state and then let it relax again. This is similar to how resonant mode oscillations can be excited in an experiment. [46]

During the relaxation phase the spatially resolved magnetisation is recorded at regular intervals. This results in a time series of the magnetisation dynamics at the location of each node in the finite element mesh (or each discretised cell in the case of finite difference simulations). A typical trajectory of an individual magnetisation degree of freedom is shown in Fig. 4.1(a), illustrating the superposition of oscillations at multiple resonant frequencies and the slow decay of the oscillations due to damping. Using a discrete Fourier transform we can extract and plot the intensity of each frequency contribution to this ringdown oscillation, resulting in a power spectrum plot such as in Fig. 4.1(b).

The resonant modes of the system correspond to peaks in this power spectrum. Once the frequency of a mode has been identified, the ringdown dynamics can be filtered to retain only the contribution of this particular mode frequency to the dynamics, by discarding the Fourier coefficients belonging to all other frequencies. Applying this procedure to the spatially resolved magnetisation data allows extracting and visualising the spatial mode profile, i.e. its magnetisation oscillation pattern across the sample.[2]

4.1.1.2 Details of the procedure

We now explain the computational details of this prodecure. Let $t_k = k \cdot \Delta t$ be the timesteps at which the magnetisation is sampled during the simulation ($k = 1, \ldots, N$), with Δt the size of the sampling interval and $T = N \cdot \Delta t$ the total duration of the recorded

[2] The Github repository [47] accompanying our proposal [43] of a new micromagnetic standard problem for ferromagnetic resonance simulations contains explicit example code illustrating how to do this.

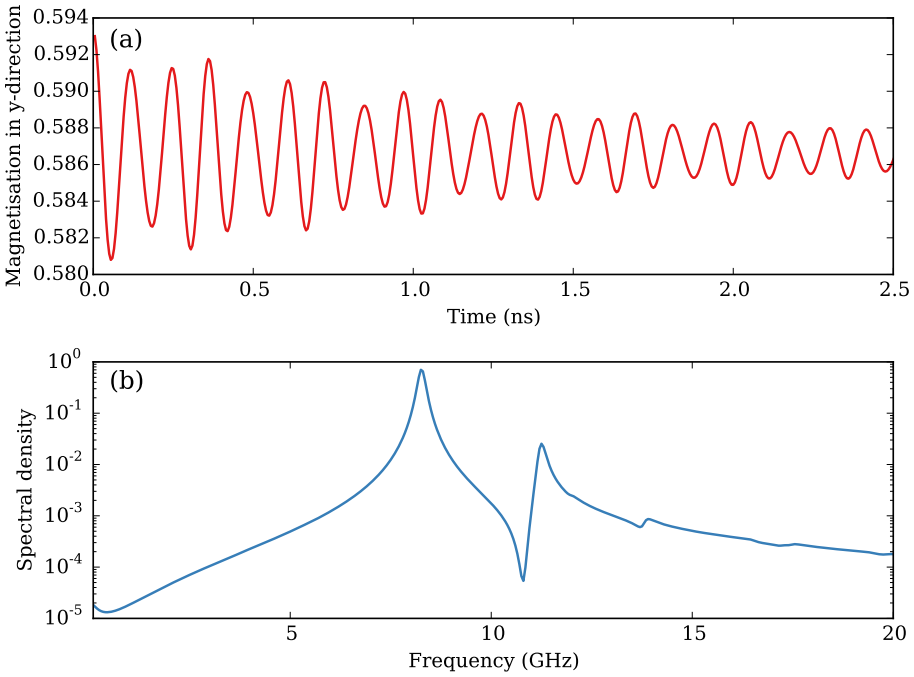

Figure 4.1: (a) Sample ringdown dynamics in a thin film permalloy sample of dimensions $120\,\mathrm{nm} \times 120\,\mathrm{nm} \times 10\,\mathrm{nm}$. The plot shows the y-component of the spatially averaged magnetisation, using the simulation setup described in a recently proposed micromagnetic standard problem for ferromagnetic resonance simulations. [43]
(b) Power spectrum obtained from the Fourier transform of the data shown in (a), computed using Eq. (4.2) in Section 4.1.1.2.

ringdown. The sampling interval determines the maximum frequency contribution to the signal that is resolvable by the discrete Fourier transform. It is given by the *Nyquist frequency*, $f_{\mathrm{N}} = 1/(2\Delta t)$. [40, Sect. 12.1] Similarly, the attainable frequency resolution in the resulting power spectrum is given by $\Delta f = 1/T$.

For each timestep t_k the spatially resolved magnetisation $\mathbf{M}(\mathbf{r}_j, t_k)$ is recorded at a number of spatial sampling locations $\mathbf{r}_j$ (these would typically be the mesh vertices in a finite element simulation or the centres of the discretised cells in a finite difference approach). At each sampling location $\mathbf{r}_j$ this yields a time series for each of the three magnetisation components. For example, in the case of M_x:

$$M_x(\mathbf{r}_j, t_k), \qquad k = 1, \ldots, N. \tag{4.1}$$

The equations in this section are only stated for M_x because they are identical for all three magnetisation components. However, depending on the geometry of the sample and the excitation used, the actual ringdown dynamics of each component may be significantly different due to the way in which the magnetisation couples to the excitation. It is therefore important to analyse the power spectra from all three components in order to capture all information.

There are two different ways in which the power spectrum can be computed from the time series in Eq. (4.1). The first approach is to calculate the spatial average of M_x across the sample at each timestep, resulting in a single time series $\langle M_x \rangle_{\mathbf{r}}(t_k)$ (we use $\langle . \rangle_{\mathbf{r}}$ to denote a spatial average across all sampling locations). From this time series the power spectrum $S_x(f)$ can be computed as follows.

$$S_x(f) = |\mathcal{F}_x(f)|^2 \qquad \text{with} \tag{4.2}$$

$$\mathcal{F}_x(f) = \sum_{k=1}^{N} \langle M_x \rangle_{\mathbf{r}}(t_k)\, e^{-i\,2\pi f t_k}. \tag{4.3}$$

We refer to this approach as *method 1*. It results in power spectra similar to what would be measured in an experiment, where only the spatially averaged magnetisation can be sampled at a time rate suitable for resolving high-frequency dynamics. However, it has the significant disadvantage that it will miss many eigenmodes with spatial symmetries because they are lost from the signal during the averaging process. An example of this is shown in the next chapter Fig. 5.1 (spectrum at the bottom left) where the only visible mode is the fundamental mode of the nanodisc.

This problem can be avoided by using a different method, which first computes the *local*

power spectra $S_x(\mathbf{r}_j, f)$ at each sampling point $\mathbf{r}_j$ from the time series of the magnetisation at that point.

$$S_x(\mathbf{r}_j, f) = \left|\mathcal{F}_x(\mathbf{r}_j, f)\right|^2 \qquad \text{with} \tag{4.4}$$

$$\mathcal{F}_x(\mathbf{r}_j, f) = \sum_{k=1}^{N} M_x(\mathbf{r}_j, t_k)\, e^{-i\,2\pi f t_k}. \tag{4.5}$$

By averaging these local power spectra across the sample we obtain the global spectrum,

$$\widetilde{S}_x(f) = \langle S_x(\mathbf{r}_j, f)\rangle_{\mathbf{r}}. \tag{4.6}$$

We refer to this approach as *method 2*. It overcomes the problem of missing modes with spatial symmetries and typically results in spectra with many more peaks than those obtained via *method 1*. An example is again shown in Fig. 5.1, where the three spectra on the top left are computed using *method 2*.

For a fixed resonant frequency f, the spatial oscillation profile of the corresponding eigenmode can be obtained from the local power spectral density coefficients $S_x(\mathbf{r}_j, f)$ in Eq. (4.5). Namely, the amplitude of the magnetisation oscillation at this location is given by the absolute value of the (complex) coefficient, whereas the argument of the coefficient (in the complex polar representation) contains the phase information.[3]

4.1.1.3 Advantages and drawbacks of the ringdown method

The major advantage of the ringdown method is that it does not require any special implementation and can thus be performed with any micromagnetic software package. The only additional code required is for the Fourier transform, for which readily available implementations exist (for example in `numpy/scipy` [48]).

However, the ringdown method also comes with a number of drawbacks. Firstly, it is very difficult to find *all* normal modes in this way. This is because the symmetry of the excitation determines which modes will be excited[4] and thus not all modes will couple to a specific excitation. An example of this for eigenmodes of a domain wall in a nanowire

[3] As mentioned previously, the Github repository [47] contains example code to to produce plots of spatial mode profiles obtained in this way.

[4] In experimental studies, this can be used to selectively excite certain modes, for example with high-frequency time-varying fields of the correct frequency. [49]

is discussed in Chapter 6 where an in-plane field excitation in the transversal direction (i.e., across the wire) only excites the "breathing mode" (Fig. 6.1) of the domain wall but no other modes.
There are workarounds for this issue. For example, one can use multiple excitations with different symmetries, but this requires multiple simulation runs and is thus more computationally expensive. Alternatively, one can use a field pulse which varies as a suitably scaled sinc function ($\mathrm{sinc}(x) = \frac{\sin x}{x}$) in both time and space. Because the Fourier transform of the sinc function is a rectangular pulse, this results in an excitation at all spatial wavelengths and uniformly across the frequency spectrum (both within a certain range defined by scaling of the sinc function). It can therefore be used to excite most or all eigenmodes. [50] An interesting alternative approach is used in a study by Carlotti et al. [51] where they introduce stochastic noise caused by thermal excitations in order to excite all the modes. However, neither of these approaches is trivial to implement and there is still a chance to miss certain eigenmodes.

Another disadvantage comes from the fact that many systems possess multiple eigenmodes with identical or very similar frequencies, for example caused by symmetries in the geometry. These modes cannot be distinguished using the ringdown method because they will show up as a single peak in the power spectrum. This issue is illustrated in Chapter 5 where it is demonstrated that certain modes of an elliptical nanodisc are not captured by the ringdown approach used by Carlotti et al. [51], but they can be detected using our calculations using the eigenvalue method (described in the next section).

Moreover, it can be difficult or impossible to use the ringdown method in situations where small changes in the external field can destabilise the system – for example, close to the depinning field of a domain wall, or near the coercive field of a nanodisc at which magnetisation reversal is triggered. In these cases the ringdown method breaks down because the external field pulse necessary to excite the modes triggers a phase transition. On the other hand, the eigenvalue method does not suffer from these problems because it considers excitations in the infinitesimal limit which are already part of the equations being solved. We use it in Chapters 5 and 6 to study the above-mentioned examples (see results in Figs. 5.3 and 6.6).

Lastly, the frequency resolution obtainable by the ringdown method depends on the length of the ringdown phase, thus requiring potentially very long simulation times in order to obtain a fine resolution. Similarly, the maximum resolvable frequency in

the spectrum depends on how often snapshots of the magnetisation are sampled during the simulation. Thus, if eigenmodes with large frequencies are present this may result in potentially large storage requirements (due to frequent sampling of the magnetisation) and slower simulation runs caused by the increased I/O operations. By contrast, the eigenvalue method does not have these issues because the numerical can compute eigenfrequencies of any magnitude, irrespective of the eigenfrequencies of other modes.

Within its limitations the ringdown method is a useful tool for computing resonant modes of magnetic nanosystems. However, despite its conceptual simplicity there is considerable margin for error in the implementation due to the variety of design choices (such as spatial discretisation, relaxation time, sampling timestep, choice of damping constant α). It is therefore desirable to have a good test case against which new implementations can be calibrated. Therefore a new micromagnetic standard problem was recently proposed [43] with a detailed specification and analysis of a sufficiently simple problem that can be simulated by micromagnetic simulation packages with varying capabilities. The effects of initial conditions and simulation parameters on the observed resonance modes are explored, which is useful for the debugging and verification of new implementations. Detailed instructions and code are provided in an accompanying `GitHub` repository [47] to allow other researchers to reproduce our results and to help with numerical calculation of ferromagnetic resonance spectra and modes in general.

My main contributions to this publication include co-design of the proposed system setup (for example, the idea of applying a canted external field in order to avoid mode degeneracies), verification of results using my implementation of the eigenvalue method in `Finmag` (see next section), continued discussions/feedback with co-authors during the write-up phase as well as major work on the `GitHub` repository which provides code to reproduce our results.

4.1.2 The Eigenvalue Method

The second approach for computing normal modes of a magnetic nanosystem is to use a (semi-)analytical method which we refer to as the *eigenvalue method*. It is a general approach that works for any system of coupled oscillators (not just micromagnetic systems), although the details of the implementation vary with the underlying equations of the interactions. In this section we explain the method in the context of micromagnetics.

The basic underlying idea is that the energy of a system attains a local minimum at a stable or metastable equilibrium, with vanishing first derivative of the energy. In the vicinity of a local equilibrium the potential can therefore be approximately described as a quadratic function and therefore to first order the restoring force (given by the derivative of the energy) which acts on a small perturbation depends linearly on this perturbation, resulting in harmonic oscillations if the system is perturbed slightly out of equilibrium.

In the case of the LLG equation, it can be shown rigorously that in the vicinity of a stable equilibrium the nonlinear magnetisation dynamics are well approximated by the linearised version of the LLG equation. [52] Using a finite element (or finite difference) discretisation the linearised equation of motion can be written as a system of ordinary differential equations (ODEs) describing the dynamics of the magnetisation components at each node in the finite element mesh. This linear system of ODEs has a full set of solutions representing the normal modes of the micromagnetic system. These solutions can be computed numerically by reformulating the problem as a large eigenvalue problem. The resulting eigenvalues represent the resonant frequencies of the micromagnetic system, and the eigenvectors encode the oscillation patterns of the magnetisation at the mesh nodes. The details of this process are described in Section 4.2.

The eigenvalue method solves the main problems with the ringdown method mentioned in Section 4.1.1 because it computes the eigenmodes directly (using the governing equations to determine the coupling and interactions between individual magnetic moments), instead of relying on an external excitation and subsequent postprocessing of the system's response. This makes it possible to compute *all* eigenmodes of a micromagnetic sample (or a selected subset, for example the first n modes with the lowest frequencies) without having to worry about accidentally missing any modes.

Similarly, degenerate modes with identical frequencies do not pose a problem – they simply show up as eigenvectors belonging to the same eigenvalue. However, depending on the numerical eigensolver the returned eigenvectors may be linear superpositions of the expected eigenmodes. An example of this is discussed in Chapter 6 where we observed a frequency crossing of two eigenmodes while one parameter of the system (the width of the nanowire) was varied continuously. For the parameter value where both eigenmodes attained the same frequency the numerical solver appeared to return "hybrid" modes, but these turned out to be just superpositions of the "pure" modes (see Section 6.A).

The major drawback of the eigenvalue method is that it is non-trivial to implement and requires a considerable amount of upfront mathematical preparation and code implementation. Moreover, depending on the formulation of the eigenproblem and the numerical solver used there can be issues with numerical stability (see discussion in Section 4.3).

However, once this is work is done and the numerical issues are addressed, the results are much cleaner and more complete, and the simulations do not require as much experimentation during setup and manual inspection/postprocessing of the results.

Therefore the trade-off between the ringdown and the eigenvalue method could be described as "no upfront work needed but potentially tricky to use in practice" vs. "lots of upfront work needed but elegant and much less painful to use in practice".

We will describe the details of the eigenvalue method in Section 4.2 and discuss in Section 4.3 how to deal with implementation issues.

4.2 The Eigenvalue Method: Theoretical Background

In this section we describe the mathematical details of the eigenvalue method. There are two main steps. Firstly, we need to linearise the LLG equation. This is done in Section 4.2.1 for the conservative (i.e., undamped) LLG equation, i.e. $\alpha = 0$. The linearised LLG equation with damping included is given in Section 4.2.5.

In a second step, the linearised LLG equation is reformulated as an eigenvalue problem in Section 4.2.2. There are two ways to do this: as an ordinary eigenvalue problem or as a generalised eigenvalue problem. Both are discussed because they have implications for the numerical implementation (discussed in Section 4.3).

The general discussion follows d'Aquino [52], but we show the derivations so that they are directly applicable to a finite element discretisation and also discuss specific issues encountered in this context. All fields in this section are considered as discretised fields defined on a finite element mesh with N vertices and can therefore be represented as vectors in $\mathbb{R}^{3N}$. For example, the magnetisation $\mathbf{m} \in \mathbb{R}^{3N}$ can be represented as a vector with $3N$ degrees of freedom, namely, three magnetisation components for each mesh node. As a consequence, the cross product in the equations below is to be understood as a vertex-wise operation, acting separately on the three vector components associated

with each mesh node. In all equations in this section we write $\mathbf{H}$ instead of $\mathbf{H}_{\text{eff}}$ for the effective field to avoid unnecessary clutter.

4.2.1 Linearising the Conservative LLG Equation

We consider a local equilibrium state $\mathbf{m}_0$ with an infinitesimal variation $\mathbf{v}(t)$ around it, i.e. $\mathbf{m}(t) = \mathbf{m}_0 + \mathbf{v}(t)$. For the time being we allow arbitrary variations $\mathbf{v}(t) \in \mathbb{R}^{3N}$. However, due to the constraint $|\mathbf{m}| = 1$ the only permitted variations are those which are orthogonal to $\mathbf{m}_0$ at each vertex. This isue will be discussed and addressed in Section 4.2.3 below.

Inserting $\mathbf{m}(t) = \mathbf{m}_0 + \mathbf{v}(t)$ into the conservative LLG equation (Eq. (2.1) with $\alpha = 0$) results in the following differential equation governing the dynamics of $\mathbf{v}$.

$$\frac{\mathrm{d}}{\mathrm{dt}}(\mathbf{m}_0 + \mathbf{v}(t)) = -\gamma \cdot \Big(\mathbf{m}_0 + \mathbf{v}(t)\Big) \times \mathbf{H}(\mathbf{m}_0 + \mathbf{v}(t)) \tag{4.7}$$

Because $\mathbf{m}_0$ is not time-dependent, the left-hand side of Eq. (4.7) simplifies to $\frac{\mathrm{d}}{\mathrm{dt}}\mathbf{v}(t)$. On the right-hand side, we can rewrite the last term $\mathbf{H}(\mathbf{m}_0 + \mathbf{v}(t))$ using a Taylor expansion:

$$\mathbf{H}(\mathbf{m}_0 + \mathbf{v}(t)) = \mathbf{H}(\mathbf{m}_0) + \frac{\mathrm{d}\mathbf{H}}{\mathrm{d}\mathbf{m}}(\mathbf{m}_0) \cdot \mathbf{v}(t) + \mathcal{O}(|\mathbf{v}|^2). \tag{4.8}$$

Here $\frac{\mathrm{d}\mathbf{H}}{\mathrm{d}\mathbf{m}}(\mathbf{m}_0)$ denotes the matrix[5] of size $3N \times 3N$ representing the derivative of $\mathbf{H}$ with respect to $\mathbf{m}$, evaluated at $\mathbf{m}_0$.

Using the abbreviation $\mathbf{H}_0 = \mathbf{H}(\mathbf{m}_0)$ for the effective field of the equilibrium state we substitute Eq. (4.8) in Eq. (4.7) and expand the cross product.

$$\frac{\mathrm{d}}{\mathrm{dt}}\mathbf{v}(t) = -\gamma \cdot \left[\mathbf{m}_0 \times \mathbf{H}_0 + \mathbf{v}(t) \times \mathbf{H}_0 + \mathbf{m}_0 \times \left(\frac{\mathrm{d}\mathbf{H}}{\mathrm{d}\mathbf{m}}(\mathbf{m}_0) \cdot \mathbf{v}(t)\right)\right] + \mathcal{O}(|\mathbf{v}|^2).$$

The first term $\mathbf{m}_0 \times \mathbf{H}_0$ vanishes because in equilibrium no torque acts on $\mathbf{m}_0$ (see Brown's equation (2.9)). Discarding quadratic terms in $|\mathbf{v}|$ therefore results in the following *linearised LLG equation*.

$$\frac{\mathrm{d}}{\mathrm{dt}}\mathbf{v}(t) = -\gamma \cdot \left[\mathbf{v}(t) \times \mathbf{H}_0 + \mathbf{m}_0 \times \left(\frac{\mathrm{d}\mathbf{H}}{\mathrm{d}\mathbf{m}}(\mathbf{m}_0) \cdot \mathbf{v}(t)\right)\right]. \tag{4.9}$$

[5] Note that while in theory this matrix is symmetric because it represents the Hessian of the micromagnetic energy, in the context of the finite element implementation in `Finmag` this is not the case due to the use of the box scheme for the effective field computation (see Section 2.4). This is discussed in more detail in Section 4.3.2 below.

4.2.2 Formulation as an Eigenvalue Problem

In order to solve the linearised LLG equation numerically, we need to reformulate it as an eigenvalue problem. The first step is to bring Eq. (4.9) into the form $\frac{\mathrm{d}}{\mathrm{dt}}\mathbf{v}(t) = A \cdot \mathbf{v}(t)$, where the matrix A represents the linear operator on the right-hand side. Then we can make the standard ansatz with an exponential solution to eliminate the derivative and arrive at an eigenvalue problem.

We start by rearranging the right-hand side of Eq. (4.9) in order to isolate $\mathbf{v}(t)$. Using the fact that $\mathbf{m}_0$ has unit length and that $\mathbf{H}_0$ is parallel to $\mathbf{m}_0$ everywhere (because $\mathbf{m}_0$ is an equilibrium state), we can write $\mathbf{H}_0 = h_0\mathbf{m}_0$, where $h_0 = |\mathbf{H}_0|$ is the magnitude of the effective field. We can thus rewrite the first term in Eq. (4.9) as follows:

$$\mathbf{v}(t) \times \mathbf{H}_0 = \mathbf{v}(t) \times h_0\mathbf{m}_0 = h_0\mathbf{v}(t) \times \mathbf{m}_0 = -\mathbf{m}_0 \times h_0\mathbf{v}(t)$$

This has the two-fold advantage of bringing $\mathbf{v}(t)$ to the right-hand side of the cross product and writing this expression in terms of a cross product with $\mathbf{m}_0$ instead of $\mathbf{H}_0$, enabling further manipulations below. Substituting this last expression in Eq. (4.9) enables us to rearrange that equation as follows, first factoring out the cross product with $\mathbf{m}_0$ and subsequently the dot product with $\mathbf{v}_0$.

$$\begin{aligned}
\frac{\mathrm{d}}{\mathrm{dt}}\mathbf{v}(t) &= -\gamma \cdot \left[-\mathbf{m}_0 \times h_0\mathbf{v}(t) \; + \; \mathbf{m}_0 \times \left(\frac{\mathrm{d}\mathbf{H}}{\mathrm{d}\mathbf{m}}(\mathbf{m}_0) \cdot \mathbf{v}(t) \right) \right] \\
&= \gamma \cdot \mathbf{m}_0 \times \left[h_0\mathbf{v}(t) - \frac{\mathrm{d}\mathbf{H}}{\mathrm{d}\mathbf{m}}(\mathbf{m}_0) \cdot \mathbf{v}(t) \right] \\
&= \gamma \cdot \mathbf{m}_0 \times \left[\left(h_0 \cdot \mathbb{1} - \frac{\mathrm{d}\mathbf{H}}{\mathrm{d}\mathbf{m}}(\mathbf{m}_0) \right) \cdot \mathbf{v}(t) \right] \\
&= \gamma \cdot \mathbf{m}_0 \times \mathcal{A}_0 \cdot \mathbf{v}(t). \qquad (4.10)
\end{aligned}$$

In the last line $\mathcal{A}_0$ denotes the operator $\mathcal{A}_0 = h_0 \cdot \mathbb{1} - \frac{\mathrm{d}\mathbf{H}}{\mathrm{d}\mathbf{m}}(\mathbf{m}_0)$, where $\mathbb{1}$ is the $3N \times 3N$ identity matrix.

The final step is to find a single matrix representation which combines the action on $\mathbf{v}(t)$ of both the operators $\mathbf{m}_0 \times \ldots$ and $\mathcal{A}_0$. In order to do so we note that for any 3-vector $\widetilde{\mathbf{w}} = (w_1, w_2, w_3)$ the matrix $\Lambda(\widetilde{\mathbf{w}}) = \begin{pmatrix} 0 & -w_3 & w_2 \\ w_3 & 0 & -w_1 \\ -w_2 & w_1 & 0 \end{pmatrix}$ provides a matrix representation of the cross product with $\widetilde{\mathbf{w}}$ from the left, i.e. $\widetilde{\mathbf{w}} \times \widetilde{\mathbf{v}} = \Lambda(\widetilde{\mathbf{w}}) \cdot \widetilde{\mathbf{v}}$ for any $\widetilde{\mathbf{v}} \in \mathbb{R}^3$. Therefore we can represent the vertex-wise cross product with $\mathbf{m}_0 \in \mathbb{R}^{3N}$ as

a block-diagonal matrix of the following form, which by slight abuse of notation we denote $\Lambda(\mathbf{m}_0)$.

$$\Lambda(\mathbf{m}_0) \coloneqq \begin{pmatrix} \Lambda(\mathbf{m}_{0,1}) & & \\ & \ddots & \\ & & \Lambda(\mathbf{m}_{0,N}) \end{pmatrix}. \tag{4.11}$$

Here $\mathbf{m}_{0,i}$ denotes the 3-vector containing the magnetisation components of $\mathbf{m}_0$ at mesh vertex i.

Using this notation we define the following $3N \times 3N$ matrix, which represents the action of both the cross product $\mathbf{m}_0 \times \ldots$ and the operator $\mathcal{A}_0$.

$$A = \gamma \cdot \Lambda(\mathbf{m}_0) \cdot \left[h_0 \cdot \mathbb{1} - \frac{\mathrm{d}\mathbf{H}}{\mathrm{d}\mathbf{m}}(\mathbf{m}_0) \right]. \tag{4.12}$$

This allows us to rewrite Eq. (4.10) as follows.

$$\frac{\mathrm{d}}{\mathrm{dt}}\mathbf{v}(t) = A \cdot \mathbf{v}(t). \tag{4.13}$$

This is the desired form of the linearised LLG equation (4.9) that enables us to turn it into an eigenvalue problem.

From the theory of linear differential equations we know that Eq. (4.13) has a full set of solutions. We make the ansatz $\mathbf{v}(t) = \mathrm{Re}\{e^{i\omega t} \cdot \mathbf{v}_0\}$, where $\omega \in \mathbb{R}$ is the (unknown) angular frequency of the normal mode oscillation, $\mathbf{v}_0 \in \mathbb{C}^{3N}$ is a constant vector and $\mathrm{Re}\{\ldots\}$ denotes the real part of a complex number (i.e., we are using phasor notation). Inserting this expression into Eq. (4.13) we obtain:[6]

$$\mathrm{Re}\{i\omega \cdot e^{i\omega t} \cdot \mathbf{v}_0\} = \mathrm{Re}\{A \cdot e^{i\omega t} \cdot \mathbf{v}_0\}.$$

Dividing the inner expressions on both sides by $e^{i\omega t}$ we end up with the following.

$$A \cdot \mathbf{v}_0 = i\omega \cdot \mathbf{v}_0. \tag{4.14}$$

This equation defines an eigenproblem which can be solved numerically. Each solution $\mathbf{v}_0$ gives rise to a normal mode oscillation of the form $\mathbf{m}(t) = \mathbf{m}_0 + \mathrm{Re}\{e^{i\omega t} \cdot \mathbf{v}_0\}$ which satisfies the linearised LLG equation. The resonant frequency of the mode is given

[6] Here we use the fact that $\mathrm{Re}\{\ldots\}$ commutes with the derivative $\frac{\mathrm{d}}{\mathrm{dt}}$ because taking the real part of a complex number is a linear operation.

by $f = \frac{1}{2\pi}\omega$, and its oscillation pattern across the finite element mesh is encoded in the coefficients of $\mathbf{v}_0$: the absolute value of each (complex) coefficient represents the oscillation amplitude of the corresponding magnetisation degree of freedom, whereas the argument of the coefficient (in the complex polar representation) contains the phase information.

4.2.3 Admissible variations and reduction of dimensionality

So far we have allowed arbitrary variations $\mathbf{v}(t) \in \mathbb{R}^{3N}$. However, as a consequence of the condition $|\mathbf{m}| = 1$ the only admissible variations are those that lie in the 2-dimensional subspace orthogonal to $\mathbf{m}_0$ at each mesh node.[7] Because we have not restricted $\mathbf{v}$ in any way, Eq. (4.14) will have a number of eigensolutions which do not represent admissible variations.[8] In order to exclude those solutions we need to constrain $\mathbf{v}$ in a suitable way. This actually turns out to be an advantage because it reduces the number of degrees of freedom from $3N$ to $2N$, resulting in significantly reduced memory consumption of the matrix A of approx. $55\,\%$.

At each mesh vertex i we choose two vectors which form an orthonormal basis of the plane perpendicular to the magnetisation vector $\mathbf{m}_{0,i}$ at this node. Then any admissible variation will be a linear combination of those two vectors at each vertex. Let C be the matrix of size $3N \times 2N$ which represents the vertex-wise embedding of $\mathbb{R}^2$ into $\mathbb{R}^3$ that maps the two standard basis vectors of $\mathbb{R}^2$ onto the chosen orthonormal basis at each vertex. Similarly, we can construct a matrix D of size $2N \times 3N$ which represents the vertex-wise projection from $\mathbb{R}^3$ onto the plane perpendicular to $\mathbf{m}_0$ (by dropping the component parallel to $\mathbf{m}_0$ at each vertex and leaving the components for the other two basis vectors untouched). Both of these matrices are block matrics with blocks of size 3×2 and 2×3, respectively. It is easy to see that these operations cancel each other so that $D \cdot C = \mathbb{1}_{2N\times 2N}$.

Any admissible variation $\mathbf{v}$ can now be written as $\mathbf{v} = C \cdot \hat{\mathbf{v}}$ where $\hat{\mathbf{v}} \in \mathbb{R}^{2N}$ is an arbitrary vector. Conversely any $2N$-vector $\hat{\mathbf{v}}$ gives rise to an admissible variation in this way. Inserting this into Eq. (4.13) and multiplying by D from the left results in

$$\frac{\mathrm{d}}{\mathrm{dt}}\hat{\mathbf{v}}(t) = (D \cdot A \cdot C) \cdot \hat{\mathbf{v}}(t) = \widehat{A} \cdot \hat{\mathbf{v}}(t) \tag{4.15}$$

[7] In the continuous case the vector field $\mathbf{v}(t)$ is required to be tangential to the manifold defined by $|\mathbf{m}| = 1$.

[8] In fact, A is degenerate. For example, $\mathbf{m}_0$ is an eigenvector of A with eigenvalue zero.

This gives a well-defined eigenproblem with a non-degenerate matrix $\widehat{A} \in \mathbb{R}^{2N \times 2N}$, which we can finally solve numerically.

4.2.4 Generalised eigenvalue problem

Equation (4.10) was used to formulate the linearised LLG equation as an ordinary eigenvalue problem. Using a slight rearrangement of this equation we can also obtain a formulation as a *generalised* eigenvalue problem. The key observation is that if $\mathbf{v}(t)$ is an admissible variation (i.e., $\mathbf{v}(t)$ lies in the plane orthogonal to $\mathbf{m}_0$ at each vertex) then the operation of taking the cross product $(\mathbf{m}_0 \times \dots)$ is invertible because it represents a rotation within this plane around the axis given by $\mathbf{m}_0$. The inverse is $(-\mathbf{m}_0 \times \dots)$, which represents the rotation by the same amount in the opposite direction. Therefore, in the case of admissible variations Eq. (4.10) can be rewritten as follows.

$$-\mathbf{m}_0 \times \frac{\mathrm{d}}{\mathrm{dt}}\mathbf{v}(t) = \gamma \mathcal{A}_0 \cdot \mathbf{v}(t). \tag{4.16}$$

Using an ansatz with an exponential solution as described above results in the following generalised eigenvalue problem.

$$B \cdot \mathbf{v}_0 = \omega \cdot M \cdot \mathbf{v}_0 \tag{4.17}$$

The matrices B and M are defined as follows.

$$B = \gamma \mathcal{A}_0, \tag{4.18}$$

$$M = -i\,\Lambda(\mathbf{m}_0). \tag{4.19}$$

The matrix M is Hermitian, and in theory this should also be the case for B. However, due to the use of the box scheme (Section 2.4) for the finite element discretisation of the effective field this is not the case in `Finmag`. The implications of this will be discussed in Section 4.3 below.

4.2.5 The Linearised Non-Conservative LLG Equation

The linearisation of the non-conservative LLG equation (i.e., with $\alpha \neq 0$) can be performed in way analogous to the derivation in Section 4.2.1. The resulting linearised LLG

equation looks as follows (with $\gamma' = \gamma/(1+\alpha^2)$; see page 8).

$$\begin{aligned}\frac{\mathrm{d}}{\mathrm{dt}}\mathbf{v}(t) = &-\gamma' \cdot \left[\mathbf{v}(t) \times \mathbf{H}_0 + \mathbf{m}_0 \times \frac{\mathrm{d}\mathbf{H}}{\mathrm{d}\mathbf{m}}(\mathbf{m}_0) \cdot \mathbf{v}(t)\right] \\ &- \alpha \cdot \gamma' \cdot \left[\mathbf{m}_0 \times \left(\mathbf{m}_0 \times \frac{\mathrm{d}\mathbf{H}}{\mathrm{d}\mathbf{m}}(\mathbf{m}_0) \cdot \mathbf{v}(t)\right) + \mathbf{m}_0 \times (\mathbf{v}(t) \times \mathbf{H}_0)\right] \end{aligned} \tag{4.20}$$

The formulation of this equation as an eigenvalue problem procedes in the same way as described in Section 4.2.2, resulting in the following eigenproblem matrix.

$$A = \gamma' \cdot \Lambda(\mathbf{m}_0) \cdot \left[h_0 \cdot \mathbb{1} - \frac{\mathrm{d}\mathbf{H}}{\mathrm{d}\mathbf{m}}(\mathbf{m}_0)\right] \cdot \left[\mathbb{1} + \alpha \cdot \Lambda(\mathbf{m}_0)\right] \tag{4.21}$$

We can see that Eqs. (4.20) and (4.21) reduce to Eqs. (4.9) and (4.12), respectively, for $\alpha = 0$.

4.3 The Eigenvalue Method: Numerical Implementation

The previous section discussed the mathematical details of formulating the linearised LLG equation as an (ordinary or generalised) eigenvalue problem. In this section we explain how this eigenvalue problem can be implemented numerically. From a conceptual point of view there is a clear optimal choice for the implementation strategy, which is discussed in Section 4.3.1. In practice, however there are limitations due to the way in which the micromagnetic equations are typically implemented in finite element-based micromagnetic packages such as `Magpar`, `Nmag` and `Finmag`. We discuss the details in Section 4.3.2 and also explain the implementation used in Finmag.

Ref. [53] provides an excellent reference for the different kinds of eigenvalue problems and eigensolvers encountered in numerical applications (as briefly described in Section 4.3.1 below). It discusses the specific properties of each type of eigenvalue problem and solver and gives good guidance for the choice of a suitable solver depending on the situation.

4.3.1 Optimal Implementation Strategy

There are two general categories of numerical eigensolvers. We refer to these as *direct solvers* and *iterative solvers*.

A direct solver computes eigensolutions of a matrix A by applying a series of transformations to it in order to bring it into a form where the solutions are easy to read off directly. Typically, this uses a variant of the QR algorithm where the matrix is decomposed as $A = QR$ with an orthogonal matrix Q and an upper triangular matrix R. Due to the use of orthogonal transformations these algorithms are numerically stable. However, the fact that they operate on the matrix A directly and compute *all* eigenvalues and eigenvectors simultaneously makes them slow and memory-intensive because the entire matrix needs to be kept in memory.

By contrast, iterative solvers are able to compute only a few selected eigenvectors and eigenvalues. Starting from an initial guess $\mathbf{v}_0$ for an approximate solution, they iteratively compute a series of better approximations $\mathbf{v}_n$ until the residual error is below a given tolerance. In the simplest case, a power iteration of the form $\mathbf{v}_n = A^n \cdot \mathbf{v}_0$ converges towards an eigenvector associated with the largest-magnitude eigenvalue. More sophisticated approaches (for example, using a *shift-and-invert* method) allow the computation of eigenvectors for, say, the k smallest-magnitude eigenvalues.

Iterative methods can be numerically less stable than direct methods and it is not guaranteed that the iteration will converge. I have seen examples with micromagnetic test cases where iterative solvers failed to converge but a direct solver computed the correct solution.[9] On the other hand, iterative solvers have two main advantages over direct methods. Firstly, they are much faster due to the fact that they can selectively compute a small subset of eigensolutions (say, those for the k smallest-magnitude eigenvalues). Moreover, because they do not directly operate on the eigenproblem matrix A they do not require it to be specified explicitly. Instead, they only need to be able to compute the *action* of A on an arbitrary vector $\mathbf{v}$ (i.e., the matrix-vector product $A \cdot \mathbf{v}$). If this action can be computed without explicitly assembling the matrix A, an iterative solver can be much more memory-efficient than a direct one.

Both direct and iterative solvers can make use of special properties of the eigenproblem. For example, in case the matrix A is Hermitian[10], there are optimised numerical algorithms available which are both faster and numerically more stable than algorithms for generic eigenproblems without any symmetry properties. [53]

[9] In order to explore this in more detail and to compare both the stability and performance of different eigensolvers (e.g. Scipy, SLEPc, ...) I wrote a software package which allows convenient computation and comparison of different eigensolvers applied to the same eigenproblem. I am planning to make this available on Github.

[10] A matrix A is called *Hermitian* if $A^\dagger = A$, where $A^\dagger = \overline{A}^{\mathrm{tr}}$ denotes the transpose of the complex-conjugate of A. An Hermitian matrix with only real entries is also called *symmetric*.

As discussed previously in Section 4.2.4, the linearised LLG equation permits a formulation as a generalised eigenvalue problem of the form $B \cdot \mathbf{v}_0 = \omega \cdot M \cdot \mathbf{v}_0$ with Hermitian matrices B, M. Furthermore, the action of M and B on a vector $\mathbf{v}$ can be computed directly as follows.

$$M \cdot \mathbf{v}_0 = -i \cdot \mathbf{m} \times \mathbf{v}_0, \tag{4.22}$$

$$B \cdot \mathbf{v}_0 = \gamma \cdot \Big(h_0 \cdot \mathbf{v}_0 - \mathbf{H}(\mathbf{v}_0) \Big). \tag{4.23}$$

The second equation is derived from the definition of the operator $\mathcal{A}_0$ (see the line after Eq. (4.10)) and uses the fact the effective field $\mathbf{H}$ is *linear* in its argument and therefore coincides with its own derivative. In particular, $\frac{\mathrm{d}\mathbf{H}}{\mathrm{d}\mathbf{m}}(\mathbf{m}_0) \cdot \mathbf{v}_0 = \mathbf{H}(\mathbf{v}_0)$.

An optimal implementation of the eigenvalue method would therefore be based on the formulation as a generalised eigenvalue problem with Hermitian matrices in Eq. (4.17). It would use an iterative solver specialised for Hermitian problems and would avoid assembling the matrices B and M explicitly by passing functions to the solver which implement the actions given in Eqs. (4.22) and (4.23).[11] Such an implementation would yield all three advantages mentioned above: speed, memory-efficiency and numerical stability.

4.3.2 Complications Due to Finite Element Formulation in Finmag

Unfortunately, there are two major complications in the context of a finite element implementation such as the one in `Finmag`.

Firstly, the derivation of Eq. (4.23) relies on the fact that $\mathbf{H}(\mathbf{m})$ is a *linear* function in $\mathbf{m}$ because it requires the simplification $\frac{\mathrm{d}\mathbf{H}}{\mathrm{d}\mathbf{m}}(\mathbf{m}_0)(\mathbf{v}) = \mathbf{H}(\mathbf{v})$. While this equality holds mathematically, it is only approximately satisfied in `Finmag`. This is because the implementation of the demag field computation via the Fredkin-Koehler method [54] requires the solution of a linear system as a sub-step, which is done via an iterative linear solver that introduces small numerical inaccuracies and prevents the effective field $\mathbf{H}$ from being exactly linear in $\mathbf{m}$ (up to machine precision). As a consequence, in my experiments with iterative eigensolvers that calculate the action of B via Eq. (4.23) they failed to converge in all test cases. Therefore it is necessary to assemble the eigenproblem matrix explicitly and compute the action using the expression $\frac{\mathrm{d}\mathbf{H}}{\mathrm{d}\mathbf{m}}(\mathbf{m}_0)(\mathbf{v})$ instead of $\mathbf{H}(\mathbf{v})$.

[11] For example, the solver `scipy.sparse.linalg.eigsh` from the `scipy` package meets all of these criteria.

This results in two major bottlenecks for computing resonant modes of micromagnetic systems in `Finmag`: the memory consumption of the eigenproblem matrix and the time needed to assemble it.[12]

The computation of the eigenproblem matrix B involves the partial derivatives of $\mathbf{H}$ with respect to each magnetisation component. This should result in a symmetric matrix because it represents the Hessian of the micromagnetic energy. However, due to the use of the box scheme (Section 2.4) in `Finmag` the resulting matrix is asymmetric due to the division by the nodal volumes V_i in Eq. (2.14). As a result, we cannot use a specialised Hermitian eigensolver and must use a generic one instead. In fact, given that the matrices are not Hermitian there is no advantage in using the formulation as a generalised eigenproblem at all – this only doubles the memory requirements because two matrices must be kept in memory instead of a single one. Therefore the implementation in `Finmag` uses the formulation as an ordinary eigenvalue problem (Eq. (4.14)). The matrix A itself is assembled according to Eq. (4.12) by numerically computing the derivative of the effective field with respect to the magnetisation, $\mathbf{H}'(\mathbf{m})$, via a finite difference scheme.

[12] The size of the eigenproblem matrix scales quadratically with the number vertices in the finite element mesh, limiting mesh sizes to ca. 15,000 vertices for which the matrix occupies ca. 7 GB of memory.

Chapter 5

Resonant Modes of an Elliptical Nanodisc

In order to illustrate the differences between the ringdown and eigenvalue method and to highlight their particular characteristics with a concrete example we now present a comparative case study which also provides a numerical verification of our implementation of the eigenvalue method. It consists of the computation of resonant modes in an elliptical magnetic nanodisc using these two different approaches.

The ringdown results stem from a recently published study by Carlotti et al. [51]. Their simulation setup together with a summary of the main results are presented in Section 5.1. The eigenmode calculations were performed using our implementation in `Finmag`. These results are discussed in Section 5.2 and compared with those by Carlotti et al. Despite the difference in simulation method there is excellent qualitative and quantitative agreement. Various advantages of the eigenvalue are demonstrated, including the fact that it can distinguish between frequency-degenerate modes which the ringdown method is unable to resolve.

This comparative study serves two goals. Firstly, it illustrates the differences discussed in Section 4.1 between the ringdown and eigenvalue method. In particular, it highlights some key strengths of the latter. Secondly, it verifies our implementation of the eigenvalue method in `Finmag` because the ringdown results were obtained using a independent code base developed by a third-party group.

5.1 Ringdown Results by Carlotti et al.

We start by summarising the simulation setup and results by Carlotti et al. The studied system is an elliptical nanodisc with dimensions $100\,\mathrm{nm} \times 60\,\mathrm{nm} \times 5\,\mathrm{nm}$. Simula-

Quantity	Symbol	Value (CGS-emu)	Value (SI)
Saturation magnetisation	M_s	$860\,\mathrm{emu/cm^3}$	$860\,\mathrm{kA/m}$
Gyromagnetic ratio	γ	$1.76 \times 10^7\,1/(\mathrm{Oe\ s})$	$2.212 \times 10^6\,\mathrm{m/(A\,s)}$
Exchange stiffness constant	A	$1.3 \times 10^{-6}\,\mathrm{erg/cm}$	$13\,\mathrm{pJ/m}$
Uniaxial anisotropy constant (anisotropy axis: x-axis)	K_1	$1 \times 10^5\,\mathrm{erg/cm^3}$	$10\,\mathrm{kJ/m^3}$

Table 5.1: Material parameters used by Carlotti et al. and their equivalents in SI units.

tions were performed with the finite difference-based commercial software package `MicroMagus` [55] using the material parameters[1] for polycristalline permalloy given in Table 5.1.

Carlotti et al. employ a variant of the ringdown approach in which the system is excited via small, random thermal fluctuations. This results in a uniform excitation of all modes both spatially and across the frequency spectrum, overcoming the major problem encountered when using a field pulse that only modes with an appropriate symmetry couple to the excitation (see Section 4.1.1).

During the simulation the spatially resolved magnetisation dynamics are recorded for a duration of $T = 200\,\mathrm{ns}$ (resulting in a frequency resolution of $1/T = 0.005\,\mathrm{GHz}$ for the computed spectra). A local Fourier transform is applied to the data collected for each discretised cell and the resulting local power spectra are averaged to obtain the global power spectrum. This is the procedure referred to as *method 2* in Section 4.1.1.2, which avoids the problem with *method 1* that eigenmodes with particular spatial symmetries may not be captured in the spectrum.

Applying a uniform magnetic field $\mathbf{H}$ to the nanodisc will result in a shift of the resonance frequencies. Examples of the global power spectrum for three different strengths of $\mathbf{H}$ are shown on the left-hand side of Fig. 5.1. The peaks in each spectrum correspond to the resonant modes of the nanodisc. By extracting the spatially resolved Fourier coefficients for a particular resonant frequency the associated spatial eigenmode profile can be extracted. The profiles for the first few modes are shown on the right-hand side of Fig. 5.1.

[1] In their paper Carlotti et al. report that they used a value of $M_\mathrm{s} = 860\,\mathrm{G}$ for the saturation magnetisation. However, the unit G (= Gauss) is most likely a misprint and the value should be $860\,\mathrm{emu/cm^3}$ instead, which is a standard value for permalloy. In our simulations we therefore used $M_\mathrm{s} = 860\,\mathrm{kA/m} = 860\,\mathrm{emu/cm^3}$, leading to excellent agreement with their results.

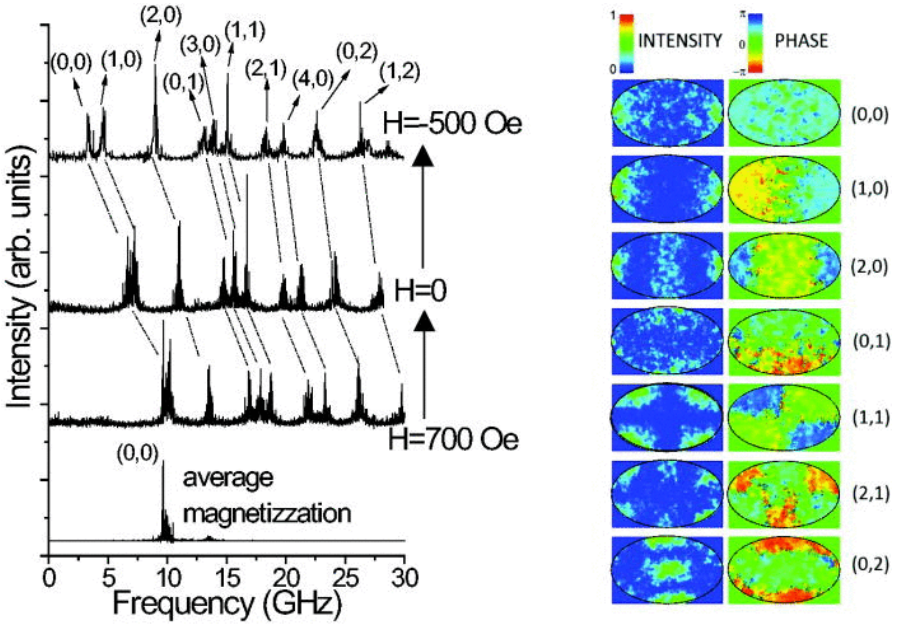

Figure 5.1: Original Fig. 1 from Carlotti et al. [51]

Left: Spectra obtained for different strengths of the applied field H. The top three spectra are computed using spatially resolved ringdown data (*method 2* in Section 4.1.1.2). The bottom one uses the spatially averaged magnetisation data (*method 1*) and shows only a single peak for the fundamental mode.

Right: Spatial profiles (amplitude and phase) of the first few eigenmodes.

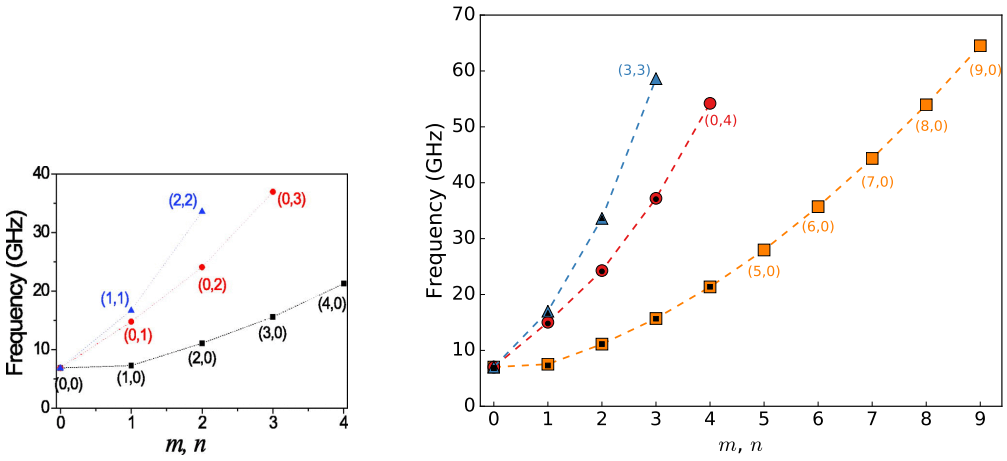

Figure 5.2:

Left: Original Fig. 2 from Carlotti et al. showing the evolution of the eigenmode frequencies in absence of any external field as a function of the mode index m and/or n.

Right: The same results produced using eigenmode computations in `Finmag` (coloured markers and lines). For better comparison the data from Carlotti et al. is also shown (black markers). The eigenvalue method produces a series of additional modes at virtually no extra computational cost (labelled data points without corresponding black markers).

Note that the fourth spectrum shown in Fig. 5.1 (at the bottom left) is obtained from the Fourier transform of the spatially *averaged* instead of the spatially resolved magnetisation (i.e., using *method 1* described in Section 4.1.1.2). It shows only a single peak corresponding to the fundamental mode (plus an almost imperceptible one for mode $(2, 0)$), illustrating the fact that most information is lost if the global spectrum is computed from the spatially averaged magnetisation.

Carlotti et al. introduce a numbering scheme to classify the eigenmodes of the nanodisc. Each mode is labelled (m, n), where m and n are the number of nodal lines perpendicular to the major and minor axis of the nanodisc, respectively. For example, the fundamental mode $(0, 0)$ consists of in-phase precession of the magnetisation in the entire disc and thus possesses no nodal lines. On the other hand, for mode $(1, 0)$ the magnetic moments in the left and right half of the nanodisc exhibit out-of-phase precession with respect to each other, separated by a nodal line of zero precession amplitude through the centre (see mode profiles in Figs. 5.1 and 5.4). The dependence of the computed eigenmode frequencies on the mode indices m and n is shown in Fig. 5.2 (left).

During the ringdown simulations Carlotti et al. apply a constant external field along the

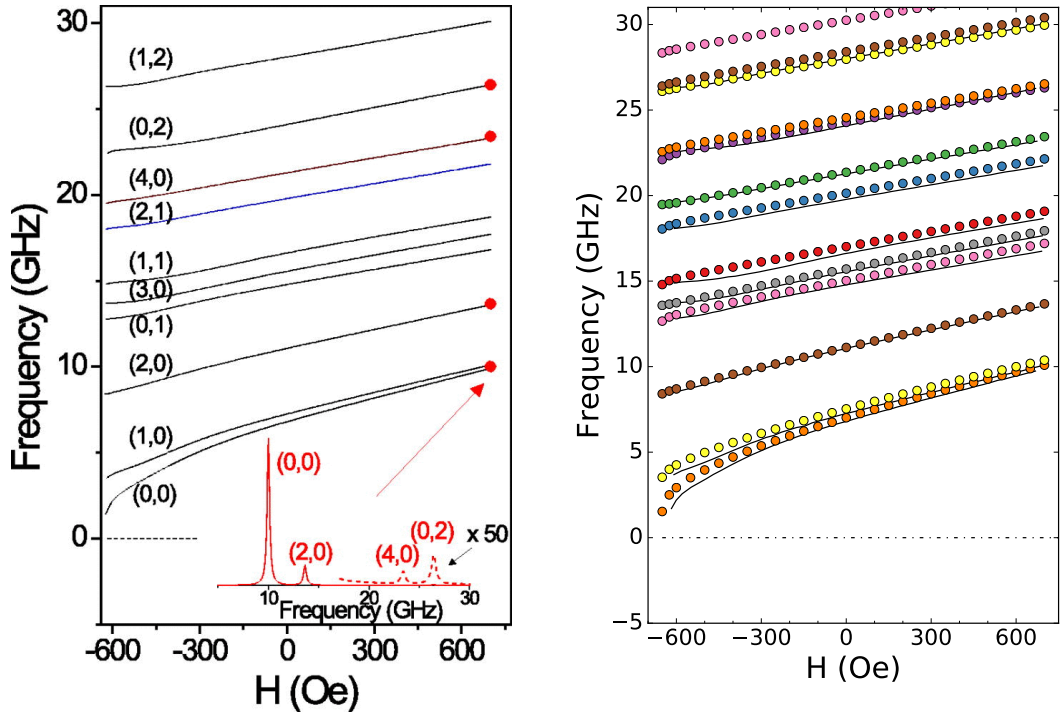

Figure 5.3:

Left: Original Fig. 3 from Carlotti et al. showing the frequencies of the first ten eigenmodes as a function of the external field strength H, computed using the ringdown approach.

Right: The same results produced using eigenmode computations in `Finmag` (coloured dots). For better comparison the data from Carlotti et al. is also shown (black lines).

major axis of the ellipse, at a slight angle of $2°$ (to avoid artifacts caused by unstable equilibrium states). The evolution of the resonant frequencies with varying field strength is shown in Fig. 5.3 (left). Almost all modes exhibit an effectively linear dependence on the field strength. However, as the applied field approaches the coercive field for which magnetisation reversal in the nanodisc is triggered ($H_x \approx -630\,\mathrm{Oe}$), the fundamental mode $(0, 0)$ softens and its frequency approaches zero.

5.2 Eigenmode Results Computed With `Finmag` and Discussion

Based on the geometry and material parameters reported by Carlotti et al. (see Table 5.1) we re-implemented the simulation setup using `Finmag` and computed the resonant modes using our implementation of the eigenvalue method described in Section 4.3. The spatial profiles for the first few eigenmodes computed by the eigenvalue method

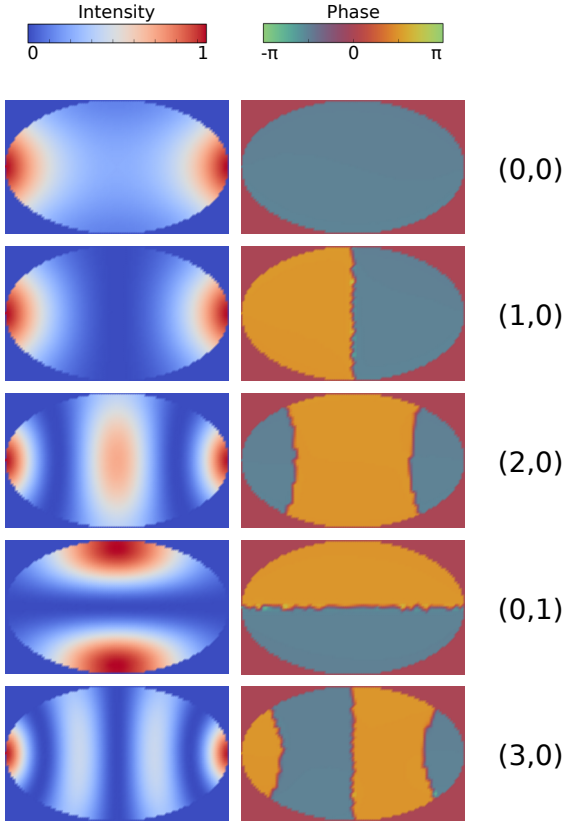

Figure 5.4: Spatial profiles of the first few modes computed using the implementation of the eigenvalue value method in `Finmag`. Compared to the profiles computed by Carlotti et al. using the ringdown method (Fig. 5.1) these do not suffer from noise.

are shown in Fig. 5.4. There is a clear correspondence with the ringdown modes in Fig. 5.1, but the profiles do not suffer from noise introduced by the random fluctuations in the ringdown method (which is needed to excite and thus detect all resonant modes).

Using the computed eigenfrequencies in the absence of an applied field the plot in Fig. 5.2 (left) was recreated using our own values, shown in Fig. 5.2 (right). For better comparison, the original data values from Carlotti et al. are also displayed as small black markers. (The values were extracted using the Open Source tool WebPlotDigitizer. [56])

There is remarkable agreement between both methods, despite the vastly different simulation appproaches. The figure also contains a number of additional data points computed by the eigenvalue method (shown with labels indicating the mode indices (m, n)). These correspond to modes that have not been computed by Carlotti et al. , either because they

have a higher frequency or because they could not be resolved from other modes with a similar frequency, as is likely the case for mode $(5, 0)$, which is part of the broad peak around $28\,\mathrm{GHz}$ at $\mathbf{H} = 0$ in Fig. 5.1.

Similar to Carlotti et al., we performed a series of simulations with different strengths of the external field $\mathbf{H}$, varying from $-650\,\mathrm{Oe}$ to $700\,\mathrm{Oe}$ in steps of $50\,\mathrm{Oe}$. A few additional simulations were performed to obtain better resolution around the coercive field, which in our case was at $H_x = -652\,\mathrm{Oe}$. The dependence of the eigenfrequencies on the field strength for the twelve lowest-frequency eigenmodes is shown in Fig. 5.3 (right). For convenience, the mode frequencies computed by Carlotti et al. (extracted from their plot using WebPlotDigitizer) are included as black lines.

Again, the agreement between both methods is excellent. The most noticeable difference occurs at small field values for the fundamental mode $(0, 0)$ and the mode $(1, 0)$. For both eigenmodes the agreement is very good for $H_x > -300\,\mathrm{Oe}$, but for values close to the coercive field ($H_x = -652\,\mathrm{Oe}$) the frequencies computed by Carlotti et al. are lower than the ones computed by the eigenvalue method, and the fundamental mode softens more quickly as the applied field approaches the coercive field. This is expected because the simulations in `Finmag` do not take temperature effects into account, whereas the ringdown simulations include thermal effects. The temperature fluctuations result in a reduced coercive field and therefore the softening of the fundamental mode occurs sooner in the ringdown simulations than in the eigenvalue simulations, accounting for the discrepancy seen in Fig. 5.3.

In Section 4.1.1.3 we discussed the fact that the ringdown method has difficulties resolving multiple resonant modes with similar frequencies. The comparison in Fig. 5.3 illustrates this. In their original plot (Fig. 5.3, left) Carlotti et al. show only the single eigenmode $(0, 2)$ in the frequency range $20 - 25\,\mathrm{GHz}$. Similarly, in Fig. 5.1 the spectra only exhibit a single (if broad) peak for this mode. However, our eigenvalue computations show that there exist in fact *two* distinct modes with very similar frequencies: mode $(0, 2)$ at $24.28\,\mathrm{GHz}$ and mode $(3, 1)$ at $24.56\,\mathrm{GHz}$ (frequency values for zero applied field). A similar situation occurs for mode $(1, 2)$ at $28.41\,\mathrm{GHz}$, which has a "companion mode" with indices $(5, 0)$ at the slightly lower frequency $27.97\,\mathrm{GHz}$ that is also not reported by Carlotti et al. (and is not distinguishable from it in the relatively noisy spectrum).

These examples illustrate the distinct advantage of the eigenvalue method over the ringdown method when dealing with frequency-degenerate modes. This property will be crucial again in Chapter 6 where we present a study of domain wall resonant modes in

a magnetic nanowire. As the width of the nanowire is varied, two of the eigenmodes exhibit a frequency crossing, which would not have been possible to study effectively with a ringdown approach.

5.3 Conclusion

In this section we presented a study of resonant modes in an elliptical magnetic nanodisc, reproducing recently published results by Carlotti et al. [51] which were computed using a ringdown approach. There is excellent agreement with the eigenmode results computed in `Finmag`, with minor discrepancies due to thermal effects in the ringdown simulations that are not taken into account in our simulations. A few key advantages of the eigenvalue method are illustrated, including the fact that frequency-degenerate eigenmodes can be easily distinguished and that modes up to much higher frequencies can be computed at no additional cost.

Chapter 6

Resonant translational, breathing and twisting modes of transverse magnetic domain walls pinned at notches

The work described in this chapter was published in Ref. [57]. The contents of the paper are reproduced below. This work has been carried out in collaboration with Dr Peter Metaxas from the University of Western Australia. All the simulations for this publication were carried out using my implementation of the eigenvalue method in `Finmag`, using simulation code that I wrote and adapted based on ideas by Dr Metaxas. Most of the simulation runs and data evaluation were performed by Dr Metaxas and the paper manuscript was mostly written by him, with my continual input and discussions about the contents of the paper, as well as advice regarding technical aspects of running the simulations and analysing the results. I also performed the analysis of the hybrid modes described in Sections 6.A and 6.3.2.

The eigenvalue method described in Chapter 4 was used to study various types of resonant modes (namely, translational, breathing and twisting modes) of transverse magnetic domain walls pinned at notches in ferromagnetic nanostrips. We demonstrate that a mode's sensitivity to notches depends strongly on the mode's characteristics. For example, the frequencies of modes that involve lateral motion of the domain wall are the most sensitive to changes in the notch intrusion depth, especially at the narrow, more strongly confined end of the domain wall. In contrast, the breathing mode, whose dynamics are concentrated away from the notches is relatively insensitive to changes in the notches' sizes. We also demonstrate a sharp drop in the translational mode's frequency towards zero when approaching depinning which is confirmed, using a harmonic oscil-

lator model, to be consistent with a reduction in the local slope of the notch-induced confining potential at its edge.

6.1 Introduction

Domain walls (DWs) are (typically nano-scale) transition regions which separate oppositely oriented magnetic domains in ferromagnetic materials. Many promising future applications of DWs rely on the current-driven displacement or resonant excitation of DWs in ferromagnetic nanostrips, the latter representing a type of DW conduit. The range of DW applications is broad and includes spintronic memristors which use DW displacements to control device resistances [58, 59], next generation data storage devices relying on DW-based shift registers [15] and even devices for the capture and transport of magnetic microbeads with envisioned use in biotechnology [60, 61]. Resonant DW excitations [62] refer to resonant precessional magnetization dynamics localized at a DW [45, 62–74]. These excitations have been shown to have the potential to be exploited in numerous areas of device-focused research, including the design of radiofrequency electronic oscillators [75], enabling control over spin wave propagation in magnonic devices [76, 77] and assisting with DW motion [78–82] and DW depinning [65, 66, 83–85], the latter via resonant excitation of a DW within a pinning (or 'trapping') potential.

The ability to exploit resonant phenomena in applications will however rely on successful control of the resonant modes of DWs. It is known that large geometrical constrictions such as notches (also widely used for positional control [15, 26, 86–88]) in micron-scale strips can be used to tune the frequency of a DW's translational mode [75]. For smaller [89] device geometries however, uniform fabrication of small notches may become challenging since the notches' dimensions will likely become comparable to those characteristic of edge roughness or lithographic defects.

In this work we show how different DW resonances have different sensitivities to notches and that these sensitivities can be linked to the nature of the mode and the structure of the DW. For example, modes which involve either local or global translation of the wall can be highly sensitive to the presence, size and position of the notch. Our work focuses in particular on the resonant properties of pinned head-to-head transverse domain walls (TDWs, Fig. 6.1(a)) which arise in thin, narrow, in-plane magnetized strips [90]. Here, the TDWs are pinned at triangular notches located on the edges of the strip. We use a

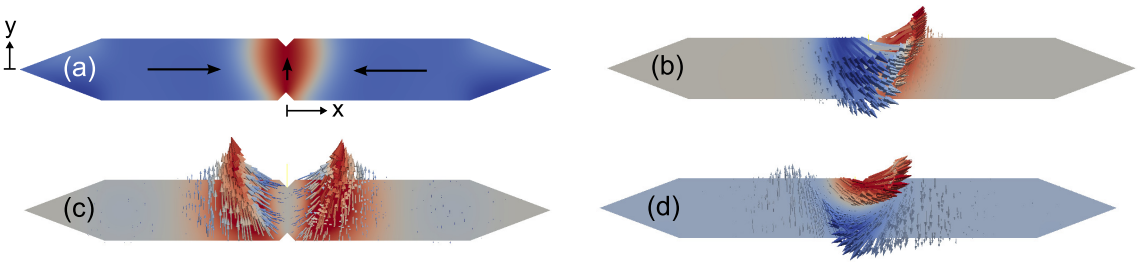

Figure 6.1: (a) Zero-field equilibrium magnetization configuration, $\mathbf{m}_0(\mathbf{r})$, in a 75 nm wide NiFe strip with symmetric notches ($w_{\text{notch}} = 20$ nm, $d_{\text{notch}} = 10$ nm) containing a head-to-head TDW with m_y color scaling. The black arrows indicate the local magnetization direction. The x and y axis origins are also shown. (b-d) Snapshots of the translational, breathing and twisting modes showing the dynamic component only ($\mathbf{dm}(\mathbf{r})$). The translational mode snapshot (b) uses m_y color scaling and is taken when the TDW is displaced to the right ($+x$) at which point there is a significant dynamic $+m_x$ component. The breathing mode snapshot (c) also uses m_y color scaling and is taken at the point during the TDW width oscillation when the width is larger than its equilibrium value. There is thus a large dynamic $+m_y$ component at the TDW edges which broadens the TDW. The twisting mode snapshot (d) uses m_x color scaling and is taken at the point when the wide end of the TDW ($+y$) is displaced to the right and the narrow end of the TDW ($-y$) is displaced to the left. See also animations of the modes at http://link.aps.org/supplemental/10.1103/PhysRevB.93.054414.

numerical eigenmode method to study three TDW resonances, corresponding to translational [64, 65, 75, 91], twisting [45, 92] and breathing [64, 93–97] excitations of the TDW. The latter mode has recently been studied for oscillator applications [98] and we demonstrate that this mode has the lowest sensitivity to changes in notch depths, making it an appealing choice for devices. The eigenmode method we use also enables the study of the translational mode in the vicinity of the static depinning field where we find a sharp drop off in this mode's frequency. This dramatic change in frequency can be linked directly to the position-dependence of the slope of the notch-induced confining potential which, as done in experiment [67, 99], we probe by field-induced displacements of the TDW within the potential.

6.2 Micromagnetic simulation method

Many numerical studies of resonant modes in confined geometries use time domain ('ringdown') methods in which Fourier analysis of precessional magnetization dynamics is employed to extract resonant mode frequencies and spatial profiles. These methods require the system to be subjected to an external excitation [44, 45, 92, 100, 101], often a pulsed magnetic field. In contrast, eigenmode methods [52, 102] enable a direct calcu-

lation of resonant magnetic modes from a system's equilibrium magnetic configuration, $\mathbf{m}_0(\mathbf{r})$ (as do dynamical matrix methods [103]). This enables the observation of the full mode spectrum without requiring careful choice of the ringdown excitation's symmetry. It also enables us to study DW modes at fields which are in the close neighborhood of the static depinning field where excited translational resonances could otherwise resonantly depin [65, 66, 83–85] the wall.

Our simulations were run on a Permalloy strip having saturation magnetization $M_S = 860$ kA/m and exchange stiffness $A_{\text{ex}} = 13$ pJ/m. The strip has tapered ends and two central notches for TDW pinning (Fig. 6.1(a)). Unless otherwise noted, the notches are located at $x = 0$, the strip thickness is 5 nm and the total length is 750 nm. Simulations were run using the finite element micromagnetic package, Finmag, which is the successor to Nmag [19] and is based on a similar design.

Magnetic eigenmodes are determined from $\mathbf{m}_0(\mathbf{r})$ with Finmag using a method similar to that described by d'Aquino *et. al.* [52] It is valid for small time-dependent oscillations, $\mathbf{dm}(\mathbf{r}, t)$, around $\mathbf{m}_0(\mathbf{r})$ and has been used recently to model ferromagnetic resonances in magnonic crystals [104]. The basic principle is to linearize the (undamped) LLG equation around the equilibrium state $\mathbf{m}_0(\mathbf{r})$, resulting in a linear system of ordinary differential equations (ODEs) for the oscillations $\mathbf{dm}(\mathbf{r}, t)$ which has has the form $\frac{\partial}{\partial t}\mathbf{dm}(\mathbf{r}, t) = A \cdot \mathbf{dm}(\mathbf{r}, t)$ with a matrix $A \in \mathbb{R}^{3N\times 3N}$, where N is the number of nodes in the finite element mesh[1]. This system of ODEs has a full set of solutions of the form $\mathbf{dm}(\mathbf{r}, t) = \text{Re}\{()e^{i2\pi ft}\mathbf{v}(\mathbf{r}))$. Each solution vector $\mathbf{v} \in \mathbb{C}^{3N}$ represents an eigenmode of the nanostrip corresponding to the frequency f; its complex coefficients encode the local amplitudes and relative phases of the eigenmode at the mesh nodes. In theory, the eigenfrequencies f are purely real. However, due to the formulation of the problem as a non-Hermitian eigenvalue problem the eigensolver returns complex solutions with a small imaginary component due to numerical inaccuracies. We quote the real parts of f. Eigenmodes localized at the TDW can be identified by visual inspection of the spatially resolved eigenvectors. Either the dynamic component, $\mathbf{dm}(\mathbf{r}, t)$, may be inspected alone or it can be scaled and added to $\mathbf{m}_0(\mathbf{r})$, enabling a visualization of the actual TDW dynamics for

[1] The matrix A has the form $A = \gamma \cdot \Lambda(\mathbf{m}_0) \cdot (H_0 - \mathbf{H}'_{\text{eff}}(\mathbf{m}_0))$, where γ is the gyromagnetic ratio, $\Lambda(\mathbf{m}_0)$ is a block-diagonal matrix representing the point-wise cross product with $\mathbf{m}_0$ at each mesh node (i.e., it is defined such that $\Lambda(\mathbf{m}_0) \cdot \mathbf{w} = \mathbf{m}_0 \times \mathbf{w}$ holds for any $\mathbf{w} \in \mathbb{R}^{3N}$), and H_0 is a block-diagonal matrix where each block is a 3×3 identity matrix multiplied by the dot product $\mathbf{H}_{\text{eff}} \cdot \mathbf{m}_0$ evaluated at the mesh node corresponding to this block. The matrix A can be derived by starting from the undamped LLG equation $\frac{\partial \mathbf{m}}{\partial t} = -\gamma \cdot \mathbf{m} \times \mathbf{H}_{\text{eff}}$, making the ansatz $\mathbf{m}(\mathbf{r}, t) = \mathbf{m}_0 + \mathbf{dm}(\mathbf{r}, t)$, multiplying out the cross product, neglecting any higher-order terms and applying suitable rearrangements to the equation in order to isolate $\mathbf{dm}(\mathbf{r}, t)$. See Eq. (95) in Ref. [52].

each mode (e.g. see mode animations[2]).

To find $\mathbf{m}_0(\mathbf{r})$, the system was initialized with a trial head-to-head TDW configuration centered on $x = 0$ and allowed to relax with damping parameter $\alpha = 1$, typically until $\frac{\mathrm{d}\mathbf{m}}{\mathrm{dt}} < 1^\circ/\mathrm{ns}$ at all points in the strip. For a strip width of 75 nm and a thickness of 5 nm, using the stricter criterion $\frac{\mathrm{d}\mathbf{m}}{\mathrm{dt}} < 0.1^\circ/\mathrm{ns}$ resulted in changes in the mode frequencies of 1.1 Mhz or less ($\leq 0.04\%$). The relaxed configuration was a pinned TDW for all studied geometries [90]. Note that the TDW (Fig. 6.1(a)) is wider at the $+y$ side of the strip which will be important for determining TDW-notch interactions.

We used a non-uniform finite element meshing with a characteristic internode length of $l_{\mathrm{mesh}} = 3$ nm at $x = 0$ (less than the NiFe exchange length [105] of 5.7 nm). There was a smooth transition to $l_{\mathrm{mesh}} = 8$ nm at the ends of the strip. This reduces computational time and memory use. However, a post-relaxation mesh coarsening [104] could potentially be applied to future studies. We note that except for those simulations in which magnetic fields close to the DW depinning field are applied, the error in the mode frequency associated with the non-uniform meshing was less than 1%. However, as a result of the non-uniform mesh, we present results only on those modes which are localized on the TDW near the center of the strip since modes associated with the domains themselves will be in regions with l_{mesh} close to or larger than the exchange length. This said, such modes (typically multiple GHz) can also be excited in experiment together with the DW modes [74].

6.3 TDW modes

The three lowest frequency TDW modes correspond to translational, breathing or twisting deformations. In Figs. 6.1(b-d) these three calculated modes are shown (as a snapshot of the mode's dynamic component, $\mathbf{dm}(\mathbf{r}, t)$ at a time such that $\mathbf{dm}(\mathbf{r}, t)$ is large) for a 75 nm strip with symmetric, triangular notches, each with width, $w_{\mathrm{notch}} = 20$ nm and a depth of intrusion into the strip, $d_{\mathrm{notch}} = 10$ nm. The translational mode (2.70 GHz) corresponds to an oscillatory, side-to-side motion of the TDW away from the notches (Fig. 6.1(b)). For the breathing mode [64, 92–97] (6.57 GHz, Fig. 6.1(c)), dynamics are concentrated at the edges of the domain wall with the excitations mirrored around $x = 0$. The dynamics of this mode result in an oscillatory change in the TDW's width as a

[2]See supplemental material at https://journals.aps.org/prb/supplemental/10.1103/PhysRevB.93.054414 for animated .GIF files which show the full resonant TDW dynamics, $\mathbf{m}_0(\mathbf{r}) + \mathbf{dm}(\mathbf{r}, t)$, for each of the three TDW modes at a strip width of 75 nm with $d_{\mathrm{notch}} = 10$ nm and $w_{\mathrm{notch}} = 20$ nm.

function of time. For this strip width, the highest frequency mode is the 7.03 GHz twisting mode (Fig. 6.1(d)). This mode involves the TDW's two ends (near the top/bottom of the strip) moving laterally but in opposite directions. Idealizing the TDW as a string crossing the nanostrip, this mode has similarities to a standing wave with a zero-displacement node ($\mathbf{dm} \approx 0$) near $y = 0$. As shown below, and in contrast to what is observed for the translational mode, a finite frequency for the breathing and twisting modes is non-reliant on confinement (i.e. they are intrinsic $f > 0$ TDW excitations). Indeed, Wang *et al.* [92] have observed what appear to be similar breathing and twisting modes for unpinned TDWs.

We now confirm that the frequencies of the translational and breathing modes obtained using the eigenmode method have good consistency with those obtained via a time domain ringdown method. To do this, we applied external excitation fields to the system which had the correct symmetry to couple to each of these two modes (we note however that we were not able to efficiently excite the twisting mode either with uniform or non-uniform excitations[3]). For the translational mode, we applied pre-ringdown excitation field in the x direction: x-fields will displace the wall and thus can be used to couple to the transaltional mode. For the breathing mode, we applied a field in the y direction which acts to increase the TDW width, thus coupling to the breathing mode's width oscillation. Fourier analysis of the resultant ringdown dynamics ($m_x(t)$ for f_{trans} and $m_y(t)$ for f_{breathe}) at a strip width of 80 nm demonstrated successful field-induced excitation of the translational and breathing modes at $f_{\mathrm{trans}} = 2.6 \pm 0.1$ GHz and $f_{\mathrm{breathe}} = 6.4 \pm 0.1$ GHz. These frequencies are in good agreement with the eigenmode results of $f_{\mathrm{trans}} = 2.61$ GHz and $f_{\mathrm{breathe}} = 6.38$ GHz for $w = 80$ nm (as per Fig. 6.2 which will be discussed later with regards to strip-width dependence of the mode frequencies).

Although this work does not attempt to address spin torque driven auto-oscillations associated with the TDW modes, radiofrequency magnetic fields (or effective fields associated with spin torques) having symmetries as discussed above can be used experimentally to drive the breathing and translational modes. This could be achieved using x or y oriented (real or effective) magnetic fields generated by striplines [71] (x or y), Oersted fields due to in-plane current injection [106] (y) or tailorable [107] Slonczewski or field-like spin torques (x or y) under perpendicular current injection in magnetic tunnel junctions (MTJs) [74, 108–110] and all-metallic magnetoresistive stacks [111]. Indeed, Lequeux *et al* [74] recently observed the translational mode under microwave frequency

[3] To do this, we attempted both spatially uniform excitations along the x, y and diagonal axes an non-uniform excitation, the latter having a field parallel to the x-axis everywhere but with a strength proportional to the y-position; i.e. pointing in positive (negative) x-direction at positive (negative) y as per Fig. 6.1(a).

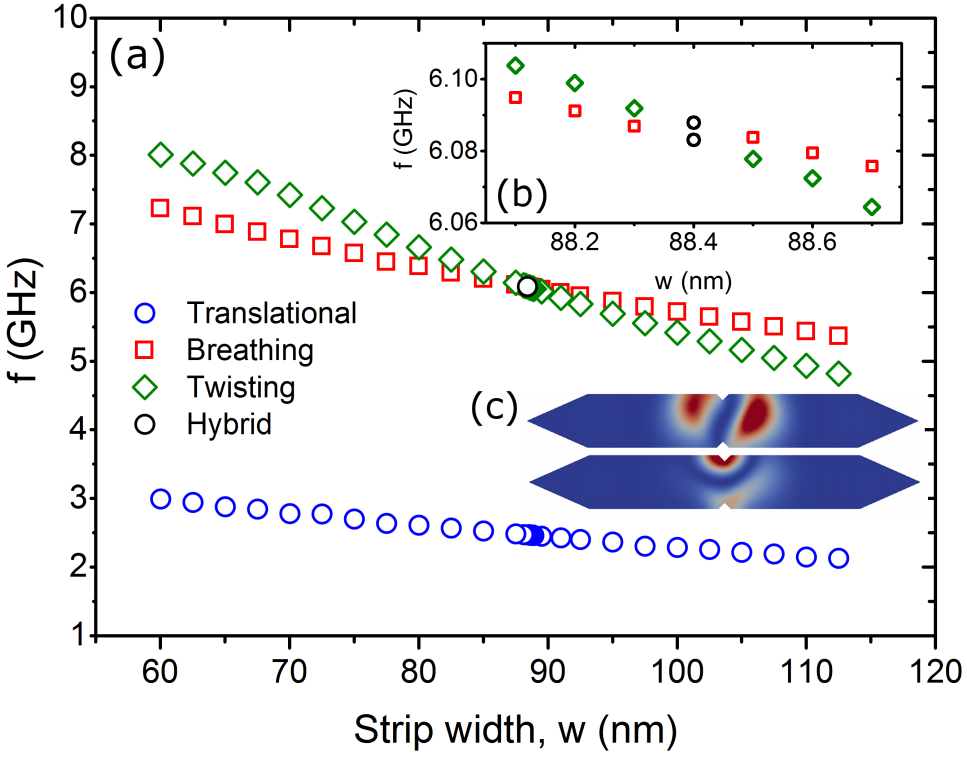

Figure 6.2: (a) Frequencies of the three TDW eigenmodes as a function of strip width, w. The notches are symmetric ($d_{\text{notch}} = 10$ nm, $w_{\text{notch}} = 20$ nm). At $w = 88.4$ nm the calculated modes are 'hybrid' breathing-twisting modes (see inset, b). (c) shows snapshots of the amplitude of the dynamic component (red) of the hybrid modes found for $w = 88.2$ nm at 6.091 GHz (upper, primarily a breathing mode) and 6.099 GHz (lower, primarily a twisting mode).

current injection in a MTJ. Numerous other studies have also demonstrated the excitation of the translational mode using spin torques due to in-plane current injection [62, 65, 75] and new possibilities exist with regards to the use of spin-orbit torques [112–114].

6.3.1 Notch dependence

We now examine the dependence of the modes on the size of the notches used to pin the TDW. The translational and twisting modes both involve some movement of the TDW away from the energetically favorable $x = 0$ position. This can either be a global side-to-side movement of the TDW (as for the translational mode) or a local side-to-side movement (as for the twisting mode where out of phase lateral TDW movements arise at opposite edges of the strip). Lateral movement has strong implications for notch sensitivity: both the twisting and translational modes have a strong dependence on the notch size. In contrast, dynamics of the breathing mode are concentrated at the lateral edges of the TDW structure (and thus away from the central notches) which results in a much weaker sensitivity to the notch and changes to it.

To demonstrate the different sensitivities of each mode to notch size, we have plotted each TDW eigenfrequency in Figs. 6.3(a,b) as a function of the notches' intrusion depths for a 75 nm wide strip with a 20 nm ($= w_{\mathrm{notch}}$) wide notch. Here, both notches have the same geometry on the two sides of the strip. One will notice immediately that the twisting and translational modes (i.e. those with a translational nature) are highly dependent on d_{notch}. The translational mode's frequency, f_{trans}, decreases smoothly with d_{notch}, going to zero at $d_{\mathrm{notch}} = 0$ (Fig. 6.3(a)). This latter result is consistent with the wall being free to translate laterally at $f_{\mathrm{trans}} = 0$ in the absence of pinning (i.e. $d_{\mathrm{notch}} = 0$ corresponds to a smooth-edged strip with no notches). The twisting mode frequency, f_{twist}, also depends quite strongly on d_{notch}, reducing by ∼40% ($\sim$ 2 GHz) when changing d_{notch} from 20 nm to 0 nm (Fig. 6.3(b)). In contrast, the breathing mode frequency, f_{breathe}, changes by only 1.5% over the same range of d_{notch} values (Fig. 6.3(b)). Note also in Fig. 6.3(b) that f_{breathe} and f_{twist} remain finite at $d_{\mathrm{notch}} = 0$, consistent with these modes being intrinsic TDW excitations for which the observation of a finite eigenfrequency is non-reliant on notch-induced, lateral TDW confinement.

Despite both notches being geometrically identical, one can see from the mode snapshots in Figs. 6.1(b,d) that both the twisting and translational modes' dynamics are largest at the wide end of the TDW. This suggests that this end of the TDW has a weaker lateral

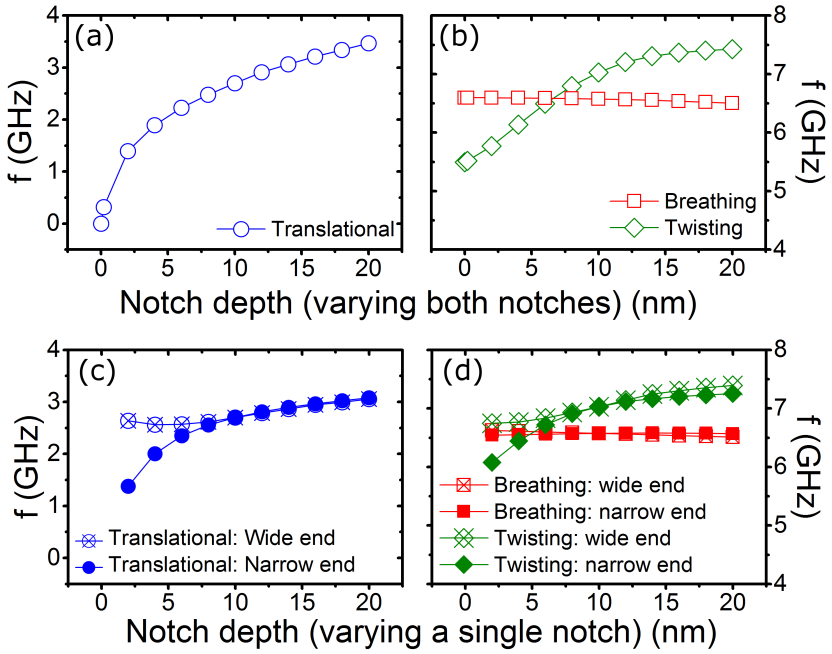

Figure 6.3: (a,b) TDW eigenfrequencies versus d_{notch} when varying d_{notch} for both notches simultaneously. (c,d) Eigenfrequencies when varying d_{notch} only at one side of the strip, either at the wide end or narrow end of the wall while keeping the other notch with $d_{\mathrm{notch}} = 10$ nm. For all data $w_{\mathrm{notch}} = 20$.

confinement than the narrow end of the TDW. This is confirmed in Fig. 6.4 which shows a TDW being pushed away from the notches under the action of a magnetic field, H, applied along the x axis ($H < H_{\mathrm{depin}}$, the static depinning field). It is indeed the less strongly pinned wide end of the TDW which is displaced furthest from the notch. To see what effect notches at each end of the wall have on the modes, we show in Figs. 6.3(c,d) results obtained while varying d_{notch} on only one side of the strip (either at the wide end or at the narrow end of the TDW) while keeping the other notch's intrusion depth fixed at 10 nm. We indeed find that f_{trans} is most sensitive to changes of d_{notch} at the narrow end of the wall, that notch being dominant in determining f_{trans}. For example, reducing d_{notch} from 10 nm to 2 nm at the narrow end of the wall (filled circles in Fig. 6.3(c)) generates a very strong, 40% reduction in f_{trans}. This reduction in f_{trans} is accompanied by a transition to a more pure translation of the TDW structure in its entirety rather than an excitation in which the highest amplitude dynamics occur at the wide end of the TDW (as in Fig. 6.1(a)) since now both ends of the wall are experiencing a relatively weak pinning. If we change d_{notch} only at the wide end of the wall however, we observe much weaker changes in f_{trans} (crossed open circles in Fig. 6.3(c)) with similar trends seen for f_{twist}. The d_{notch}-dependence of f_{breathe} again remains very weak.

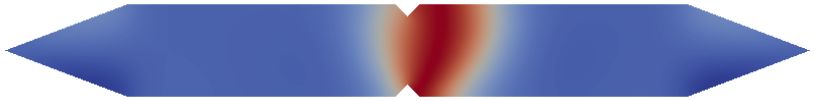

Figure 6.4: Deformed domain wall in a 75 nm strip for $H_x = 5530$ A/m.

To test the limits of the d_{notch}-insensitivity of f_{breathe}, simulations were run with the notch at the wide end of the wall displaced away from $x = 0$ for the 75 nm wide strip. This did lead to small changes in f_{breathe} ($d_{\text{notch}} = 10$ nm, $w_{\text{notch}} = 20$ nm) with some distortion of the breathing mode observed when the notch was right at the edge of the TDW. However the maximum frequency change still remained within 3% of the value observed for two laterally centered notches. We also looked at the percentage variation of f_{breathe} for two other strip widths for centrally located notches (60 nm and 100 nm wide strips again having a 5 nm thickness). We found the lowest sensitivity occurred for larger strip widths where the notch intrudes comparatively less far into the strip and thus presumably generates the weakest change to the energy landscape that is experienced by the TDW (confirmed in Sec. 6.3.3 for the translational mode). Reducing the thickness of the layer also led to a further reduced sensitivity. This can be seen in Fig. 6.5(b) where we again plot resonance data for 60 nm and 75 nm wide strips but this time with a reduced (2.5 nm) strip thickness. An important point to note from Fig. 6.5 is that the breathing mode remains highly insensitive to changes in the d_{notch} of small notches for all studied strip widths. Indeed, we see the largest changes in f_{breathe} when d_{notch} becomes larger than about 12 nm suggesting that small defects should have only a very minor effect on the breathing mode. In contrast, the other two modes exhibit the highest sensitivity to changes in d_{notch} when d_{notch} is small (Fig. 6.3).

We briefly note that changes in the *width* of the notch (for a fixed notch depth of 10 nm) yielded only weak changes for f_{breathe} and f_{twist}. Over a range of notch widths from 5 nm to 50 nm we observed $\Delta f_{\text{twist}} \leq 3$ % and $\Delta f_{\text{breathe}} \leq 2$ %. The change in f_{trans} was also quite small when reducing the notch width below 20 nm ($\Delta f_{\text{trans}} \leq 6$ %). However, broadening the notch to 50 nm led to a strong reduction in f_{trans} of > 60 %, presumably due to a strongly reduced confinement by the broader notches (the effect of confinement on f_{trans} is discussed further below).

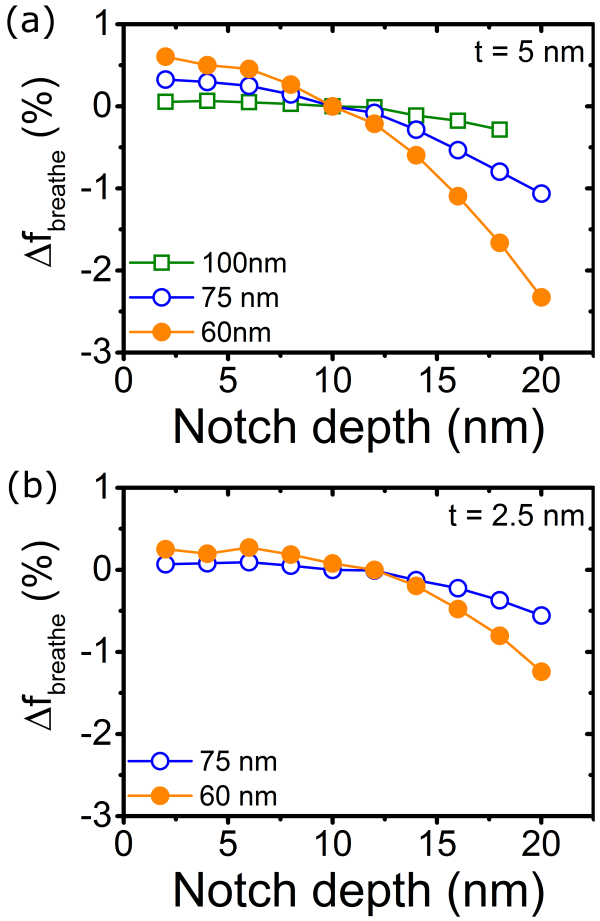

Figure 6.5: Percentage change in f_{breathe} with respect to f_{breathe} at $d_{\mathrm{notch}} = 10$ plotted against d_{notch} for (a) 5 nm thick strips and (b) 2.5 nm thick strips at various strip widths (see legends).

6.3.2 Strip width dependence

When holding the notch geometry constant ($w_{\mathrm{notch}} = 20$ nm and $d_{\mathrm{notch}} = 10$ nm), an increasing the strip width generates an reduction in each of the TDW mode frequencies (Fig. 6.2(a)). The breathing and twisting modes remain highest in frequency and their similar frequencies, coupled with slightly different width dependencies, results in a mode crossing which occurs at $w = w_{\mathrm{c}} \approx 88.4$ nm for this 5 nm thick strip (Figs. 6.2(b)). At $w \approx w_{\mathrm{c}}$, a translational mode as well as two other distinct TDW modes are found with the latter appearing as 'hybrid' twisting-breathing modes (e.g. Fig. 6.2(c)). However, their hybrid nature is due to the arbitrary basis chosen by the eigensolver: each hybrid mode can in fact be shown to be a linear combination of the 'pure' orthogonal twisting and breathing eigenmodes (see Appendix 6.A). Indeed, we expect no coupling between different modes due to the exclusion of damping and non-linear terms in our approach [52]. The hybrid nature of the modes remains clearly identifiable via visual inspection for $|w - w_{\mathrm{c}}| \lesssim 1.5$ nm. However, as $|w - w_{\mathrm{c}}|$ increases, the computed modes become more 'pure' (i.e. a dominant breathing or twisting characteristic). In Fig. 6.2(b), all modes at $w \neq 88.4$ nm are labeled either as twisting or breathing with the label corresponding to the mode which is dominant. Analogous hybrid modes were also calculated for a similar geometry using the mode solver in the SpinFlow3D simulation packag. Some details on this solver have been given previously [102].

6.3.3 Width dependent confinement and its effect on the translational mode

We now turn specifically to the width dependence of the translational mode which will be shown to be linked to the width-dependence of the notch-induced confinement of the TDW. Note that some qualitative models for the higher frequency breathing and twisting mode frequencies as a function of strip width are given in Appendix 6.B.

The frequency of the translational mode of the pinned TDW, f_{trans}, as a function of $H < H_{\mathrm{depin}}$ is shown for a number of strip widths in Fig. 6.6 (again we use $w_{\mathrm{notch}} = 20$ nm and $d_{\mathrm{notch}} = 10$ nm). Note that for fields above the depinning field (i.e. $H > H_{\mathrm{depin}}$), the system's relaxed configuration is that of a quasi-uniformly magnetized strip with the TDW having been displaced towards the end of the strip and annihilated during the simulation's relaxation stage (i.e. the moment where we first determine $\mathbf{m}_0(\mathbf{r})$). As

such, there is no TDW mode data above H_{depin} (since no TDW is present). For all strip widths, f_{trans} shows a weak negative monotonic dependence on H for small H/H_{depin}. However, f_{trans} drops sharply to zero (i.e. again going toward the case of a free TDW) as $H \to H_{\mathrm{depin}}$. DW resonant frequency *reductions* near depinning have been previously observed experimentally [67, 99]. Note that for $H \approx H_{\mathrm{depin}}$, f_{trans} exhibits a stronger sensitivity to the relaxation parameters of the simulation, requiring the use of a smaller $\frac{\mathrm{d}\mathbf{m}}{\mathrm{dt}}$ near H_{depin}. f_{trans} as well as the determined value of H_{depin} itself is also more sensitive to the non-uniform meshing than the undeformed TDW at $H = 0$. For example, a slightly higher H_{depin} ($< 1\%$ relative change) was found when using $l_{\mathrm{mesh}} = 3$ nm throughout the structure at $w = 60$ nm. Thus, there is some influence of the meshing on the pinning of the wall here.

As H_{depin} is approached, f_{twist} also drops in frequency (Fig. 6.6(b)) which may, in part, be due to the wide part of the TDW being away from the upper notch (as per Fig. 6.4). This shifts the concentration of the dynamics at the upper edge of the strip away from the notch (Fig. 6.6(c)). We have already seen that strongly reducing the size of the upper notch for an undisplaced wall reduces f_{twist} (Fig. 6.3(d)) and the case of the displaced wall is somewhat analogous as the upper part of the wall is now far from the notch (i.e. we effectively have $d_{\mathrm{notch}} \to 0$ at the location of the upper end of the TDW). Unlike f_{trans}, f_{twist} remains finite near depinning, analogous to the finite f_{twist} observed for $d_{\mathrm{notch}} = 0$ in Fig. 6.3(b). The breathing mode again shows a very weak change in its frequency even near depinning where the spatial profile of the mode is strongly deformed (Fig. 6.6(d)) with respect to the case of a non-displaced wall (Fig. 6.1(c)). Once again this highlights the robustness of f_{breathe} (to notch geometry and now in-plane-field-induced deformation).

In Fig. 6.6 an increased f_{trans} can be observed at small strip widths (a trend which has already been seen in Fig. 6.2(a)) and this is accompanied by an increased H_{depin}. To understand this, we will take the previously used approach of modeling a parabolic, notch-induced TDW confining potential [33, 66, 75, 84, 115]. This results in a spring like behavior of the DW with a restoring force of $-k_N x$ where k_N is the pinned TDW's spring constant and x its displacement from the center of the strip. The equilibrium position of the TDW at a given H is determined by a balance between this restoring force and the effective force due to the applied magnetic field [33, 84]. This force can be estimated from the x-derivative of the change in Zeeman energy for the displaced TDW: $2\mu_0 wtM_S H$ where $t = 5$ nm is the strip thickness and $\mu_0 = 4\pi \times 10^{-7}$ T·m/A. Note that we neglect the locally altered strip width at the notch.

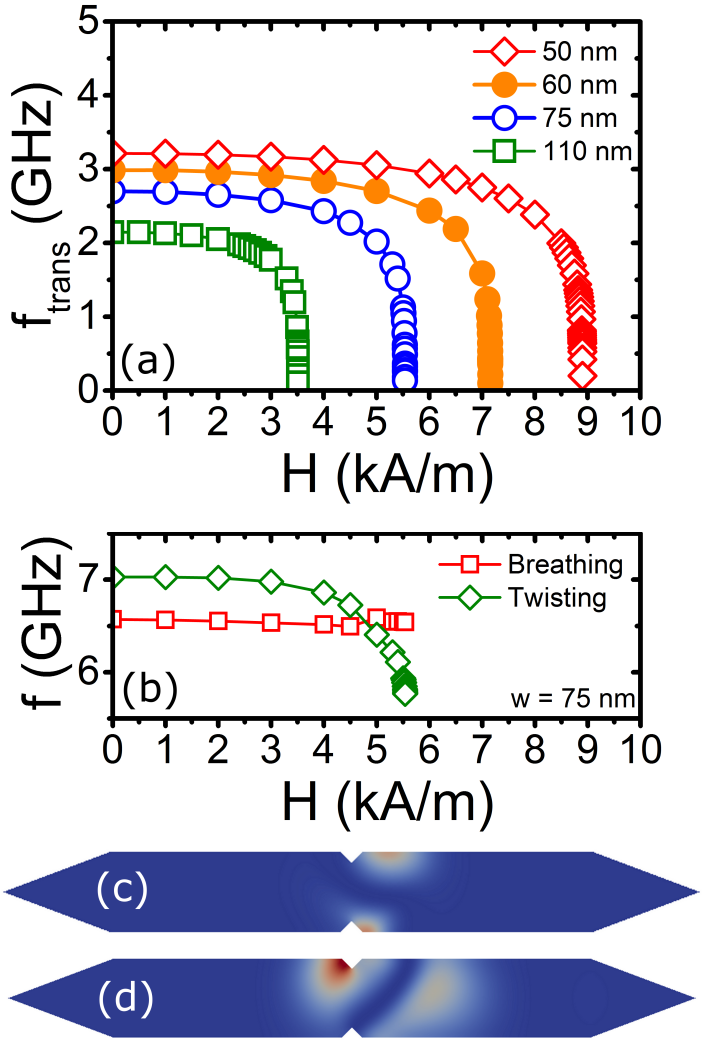

Figure 6.6: (a) f_{trans} versus in-plane field, H (oriented along $+x$), for strip widths of 50, 60, 75 and 110 nm ($d_{\mathrm{notch}} = 10$ nm and $w_{\mathrm{notch}} = 20$ nm). (b) f_{breathe} and f_{twist} versus H at a strip width of 75 nm. (c,d) Snapshots of the amplitude of the dynamic component (red) of the magnetization for the (c) twisting and (d) breathing modes at a strip width of 75 nm for $H = 5530$ A/m (i.e. close to depinning).

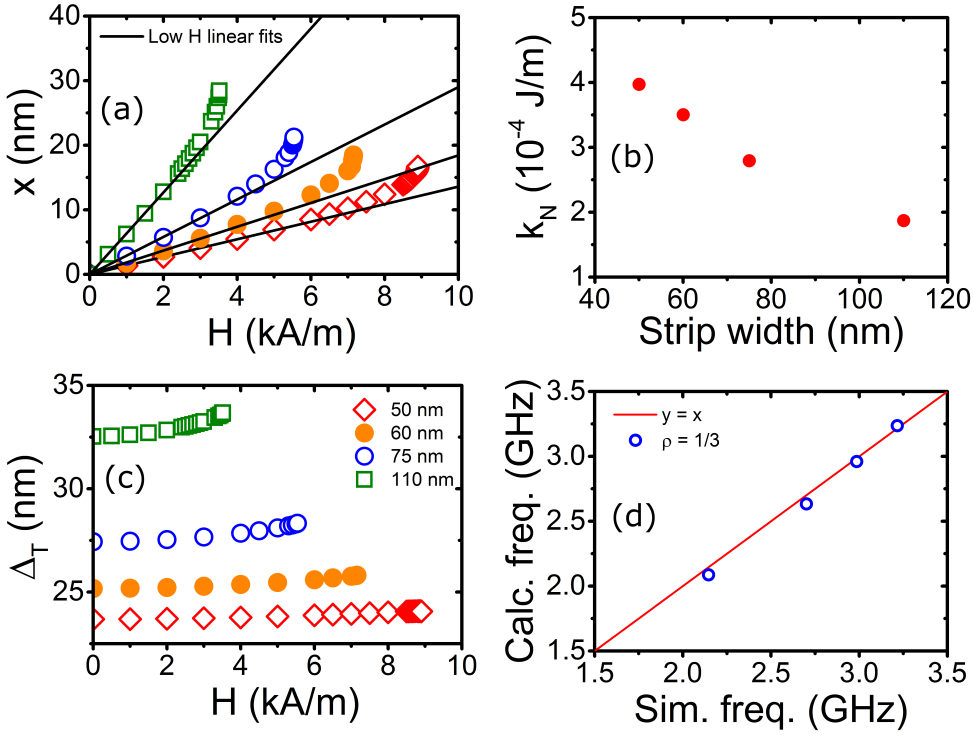

Figure 6.7: (a) Equilibrium TDW position versus H applied along the $+x$ direction. Solid lines are linear fits to the low field data (typically the first four to five points). (b) TDW spring constant versus strip width calculated from the linear fits in (a) using Eq. (6.1). (c) Thiele domain wall width of the H-deformed TDWs versus H. (d) Calculated $f_{\rm trans}$ (calculated as per the text using the data in (a,c) and Eqs. (6.1-6.3)) versus the simulated $f_{\rm trans}$ taken from the data in Fig. 6.6.

To extract k_N, in Fig. 6.7(a) we plot the equilibrium position for the domain wall versus H for the data shown in Fig. 6.6. The position of the field-deformed TDW (see, e.g., Fig. 6.4), x, was determined from the spatially averaged x-component of the magnetization along the strip [33, 84]. For low field, there is good linearity between x and H, indicative of a close-to-parabolic pinning potential. At larger fields however, there is a faster than linear growth in the $x_{\rm TDW}$, the effect of which will be discussed further below. From the data in the linear region (which has slope $dx/dH = g_{\rm linear}$), we can estimate a value for k_N:

$$k_N = (2\mu_0 wtM_S)(x/H)^{-1} = (2\mu_0 wtM_S)g_{\rm linear}^{-1}. \tag{6.1}$$

k_N, plotted in Fig. 6.7(b) versus the strip width, reduces with increasing strip width. At small widths, this results in a stiffer domain wall where the notch, which has a fixed size here, makes a larger *relative* intrusion into the strip.

We can now use the values of k_N to estimate f_{trans} at $H = 0$ and compare to the data in Fig. 6.2 [33, 84]:

$$f_{\text{trans}} = \frac{1}{2\pi}\sqrt{\frac{k_N}{m_w}}. \tag{6.2}$$

Here, m_w is the mass (e.g. [62, 91, 116]) of the TDW. Note that an increased resonant frequency is observed for smaller widths (Fig. 6.6) where k_N is higher (Fig. 6.7(b)). Thus we can immediately see that our results are qualitatively consistent with the trend suggested by Eq. (6.2), at least under the assumption of a w-independent mass. To obtain numerical values for f_{trans} however, we must estimate the mass for which we use the damping-free ($\alpha = 0$) expression [33, 84] (a similar expression is given by Krüger [117]):

$$m_w = \frac{2\mu_0 wt}{\gamma^2(N_z - N_y)\Delta}\ . \tag{6.3}$$

$\gamma = 2.210713 \times 10^5$ m/A.s and $\Delta = \Delta_T$ is the Thiele DW width [118] (field dependent, as per Fig. 6.7(c)) which is defined by $2/\Delta_T = 1/(wt)\int_V (dm/dx)^2$ where V is the nanostrip volume. N_y and N_z are the demagnetizing factors for the TDW in the y and z directions. To calculate these factors, we used expressions given by Aharoni [119], treating the TDW as a uniformly magnetized slab with a length in the y direction equal to the strip width, a height in the z direction equal to the strip thickness and a width in the x direction of $\rho\Delta_T(H = 0)$. ρ, a scaling factor, is the only free parameter since the strip width and strip thickness are fixed. It sets the width of the rectangular prism used for the demagnetizing field calculation as a fraction of the Thiele width.

As can be seen in Fig. 6.7(d), good agreement between the eigenmode simulation at $H = 0$ and the spring model (Eq. (6.2)) is found for the four studied thicknesses when using $\rho = \frac{1}{3}$. This means that the slab used for the demagnetizing factor calculation is ~ 10 nm wide in the x direction, essentially covering a central narrow slice of the TDW structure where the magnetization is quasi-uniformly magnetized in the y-direction (Fig. 6.8(a)) and thus close to our original model of a uniformly magnetized slab. Note that the magnetization undergoes an almost complete rotation from being aligned along $+x$ to $-x$ over a much larger distance $\sim \pi\Delta_T$ (Fig. 6.8(a)). It is however the central region of the TDW which appears to be the relevant part in this approach.

The effective width of the pinning potential, L_{pin}, defined here as the maximum displacement of the TDW measured before depinning (Fig. 6.7(a)), increases with Δ_T (read from Fig. 6.8(b)) and thus with strip width. However, the depinning field (the field at which the wall can escape from the pinning potential) is smallest in these wide strips (Fig. 6.6(a)) which are characterized by a larger L_{pin}. Thus, although the pinning potential has a larger

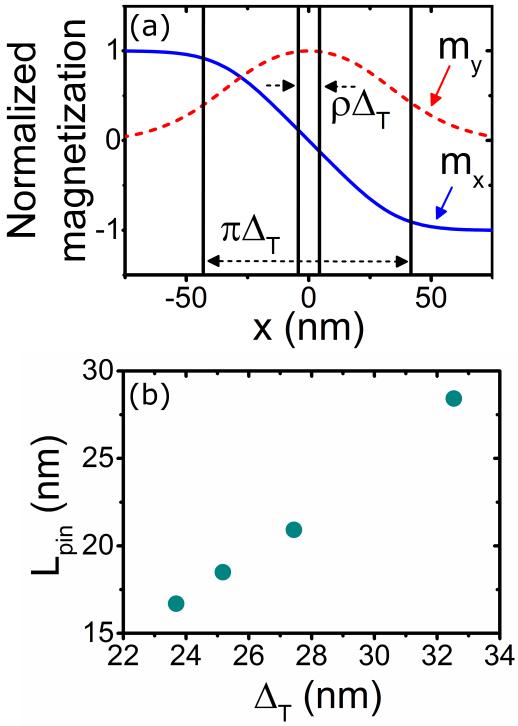

Figure 6.8: (a) x-dependence of the x and y components of the magnetization taken at $y = 0$ (at the center of the strip). Δ_T is the Thiele DW width and ρ is a scaling factor used in the demagnetizing field calculation. (b) Effective width of the pinning potential ($L_{\rm pin}$) estimated from the maximum displacement of the TDW before depinning (taken from Fig. 6.7(a)) plotted against Δ_T for strip widths of 50, 60, 75 and 110 nm. The largest width strip has the largest Δ_T.

effective width when the strip width is larger (increasing by a factor of ∼1.4, Fig. 6.7(c)), it appears to be the reduced k_N (which changes more strongly, reducing by a factor of ∼2, Fig. 6.7(b)) which is dominant in determining the strength of the depinning field (i.e. leading to a reduced H_{depin} (and f_{trans}) at larger strip widths).

Finally, we address the faster than linear growth in the TDW position versus H (Fig. 6.7(a)) which is a result of the pinning potential having a reduced steepness near its edge [99]. We can show that Eq. (6.2) remains valid in describing f_{trans} at $x \neq 0$ (i.e. even in the non-parabolic [67, 99] part of the potential) if we replace k_N by a local effective spring constant

$$k_{N,\mathrm{eff}}(x(H)) = \frac{2\mu_0 wtM_S}{dx/dH}. \tag{6.4}$$

In Fig. 6.9 $\sqrt{(dx_{\mathrm{TDW}}/dH)^{-1}}$ ($\propto f_{\mathrm{trans}}$ as per Eq. (6.2)) has been plotted versus the simulated values of f_{trans} for all studied strips. We have neglected any field-induced change in the TDW mass ($m_w = m_w(H = 0)$) and have used a numerical derivative of the data in Fig. 6.7(a) to determine dx_{TDW}/dH. We find a high degree of linearity over the full field range for all strip widths. This confirms the continued validity of Eq. (6.2) and demonstrates that the sharp drop-off in f_{trans} near H_{depin} (Fig. 6.6) can be linked with a change in the local gradient of the pinning potential at its edge, the latter determining the resonant frequency of the displaced TDW in the small oscillation limit. Note that from Eq. (6.2), we expect that the slope of the data in Fig. 6.9 will be $2\pi\sqrt{m_w(H=0)/2\mu_0 wtM_s}$. We have plotted the ratio of the predicted slope to the fitted slope in the inset of Fig. 6.9(d) where we indeed find consistency to within 2.5%.

6.4 Conclusion

We have numerically calculated eigenmodes of transverse domain walls (TDWs) which are pinned at triangular notches in in-plane magnetized nanostrips. This enabled the study of translational, twisting and breathing resonances of TDWs and the effect that notch geometry and field-induced TDW displacements have on these modes.

The twisting and translational modes both involve either local or global lateral translation of the wall structure within the notch-induced pinning potential. This leads to a clear sensitivity to changes in the intrusion depth of the notches especially to that of the notch at the narrow end of the TDW structure which has a dominant role in laterally confining the TDW. The breathing mode, which is characterized by dynamics concentrated at the

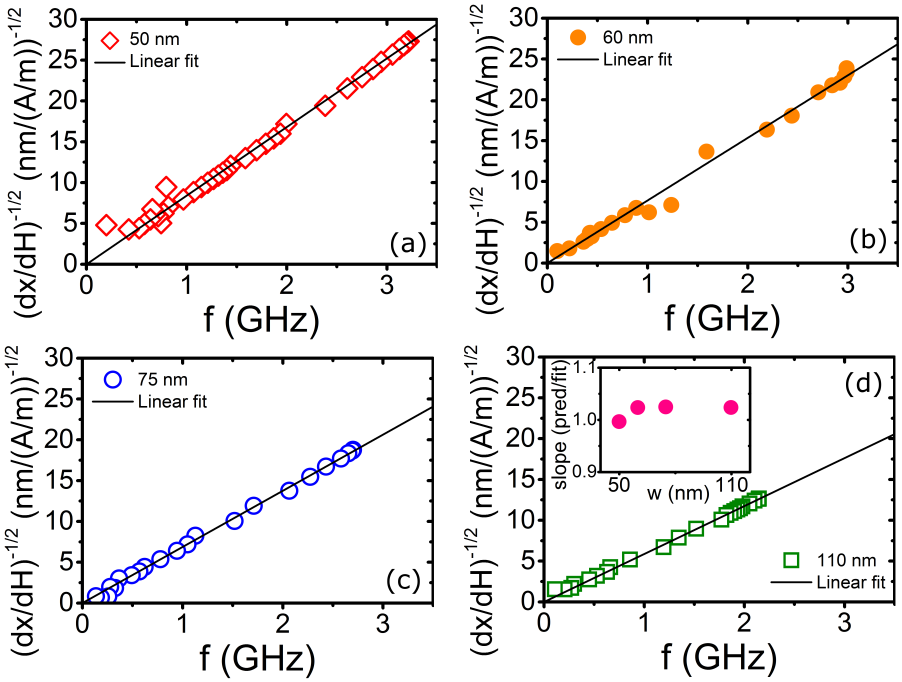

Figure 6.9: Plot of $(dx_{\mathrm{TDW}}/dH)^{-1}$, proportional to the local effective spring constant, versus f_{trans} for field-displaced TDWs in strip widths of (a) 50, (b) 60, (c) 75, and (d) 110 nm. $(dx_{\mathrm{TDW}}/dH)^{-1}$ and f_{trans} data were taken, respectively, from Figs. 6.7(a) and 6.6. Solid lines are linear fits to the data assuming a zero x-axis intercept. The inset in (d) shows the ratio of the slope of the data in (a-c) predicted from the spring model to the measured slope.

lateral edges of the TDW (and thus away from the notches), was relatively insensitive to changes in the notch intrusion depth and width. For example, when varying the notch intrusion depth from 0 to 20 nm, the largest change in the mode's frequency was 3% (observed for the narrowest studied strip width of 60 nm). Based on our results, this sensitivity could be further reduced by using a thinner or wider strip.

These results may be relevant when choosing which TDW mode to exploit in DW oscillators or when aiming to individually or simultaneously excite (multiple) DWs pinned at different positions within a strip (e.g. in shift registers [15, 98, 120]). This is because certain modes (i.e. those with a translational nature) will be more sensitive to non-uniformity of notch geometries and/or to the presence of small uncontrolled defects. Our results suggest that the breathing mode frequency will be the most robust to the introduction of small unwanted defects or non-uniformity in fabricated notch geometries, especially at larger strip widths or smaller notch depths. In contrast, having a translational or twisting mode frequency which is robust to small changes in the notch geometry appears to be reliant on having relatively large notches.

For a fixed notch geometry, the frequencies of all modes increased with decreasing strip width, making this an important device parameter to control. In the particular case of the translational mode's frequency, its width dependence could be reproduced with a spring model for notch-induced TDW confinement. Furthermore, the eigenmode method (which does *not* rely on the forced driving of the TDW's resonant dynamics) allowed us to determine the translational mode frequencies over a wide range of fields, including in the vicinity of the static depinning field where the translational mode frequency dropped sharply towards zero as the TDW was displaced to the edge of the confining potential. At low applied magnetic fields (and thus low TDW displacements), the notch-induced confining potential was parabolic, enabling us to analytically reproduce the simulated translational mode frequency at zero field. At large fields (which generated larger displacements of the TDW within the confining potential), the growth of the pinning potential's energy with displacement was sub-parabolic (as seen previously for a vortex DW [99]). Here the spring model could still be used to reproduce the translational mode frequencies as long as the local slope of the pinning potential was used to calculate the spring constant. This calculation required a DW mass determination with a good match between quasi-analytics and simulation achieved when using only the very narrow central part of the TDW for the calculation of the TDW's demagnetizing factors (critical for the determination of the TDW's mass).

Finally, we note that f_{trans} is finite only in the presence of confinement. In contrast,

f_{breathe} and f_{twist} remain large and finite even without a notch or close to the depinning field, demonstrating an intrinsic $f > 0$ characteristic, albeit with some (mode-dependent) sensitivity to the notches' presence.

Appendices

6.A Extraction of pure modes from hybrid modes

To demonstrate that each 'hybrid' mode (Fig. 6.2(c)) is a linear combination of the 'pure' orthogonal twisting and breathing eigenmodes, we let $\mathbf{v}_1, \mathbf{v}_2$ be the hybrid mode eigenvectors as returned by the solver (their complex entries encode the amplitude and relative phase of the magnetization oscillations at each mesh node). To show that these can be reduced to the 'pure' modes we need to find complex scalars a_1, a_2 such that the linear combination $\mathbf{v} = a_1\mathbf{v}_1 + a_2\mathbf{v}_2$ represents a breathing or twisting mode. The breathing mode is characterized by being fully symmetric about the y-axis, i.e. the oscillations in the left and right half of the nanostrip are out of phase by $180°$: $\mathbf{v}(x, y, z) = -\mathbf{v}(-x, y, z)$. The expression $\int |\mathbf{v}(x, y, z) + \mathbf{v}(-x, y, z)|$ thus measures the deviation from symmetry for an eigenmode $\mathbf{v}$ and we can find the 'most symmetric' linear combination by minimizing this with respect to a_1, a_2. Since each eigenvector is only determined up to a scalar, we can assume that $a_1 = 1$ (or $a_2 = 1$), reducing the dimensionality of the optimization problem. The obtained linear combination is confirmed to be an eigenvector corresponding to a breathing mode. Similarly, the twisting mode can be recovered by using the condition $\mathbf{v}_{\mathrm{twist}}(x, y, z) = \mathbf{v}_{\mathrm{twist}}(-x, y, z)$.

6.B Modeling the twisting and breathing modes

We detail here two simple qualitative models for the f_{breathe} and f_{twist} strip width dependencies seen in Fig. 6.2(a).

The general trend of decreasing f_{twist} with w for fixed notch geometry is qualitatively consistent with a string-like mode that is confined across the strip having a single node in the strip's center (i.e. with wavelength $\sim 2w$ and thus a frequency $\propto \frac{1}{w}$). We plot f_{twist} versus $\frac{1}{w}$ in Fig. 6.10(a) with reasonable linearity at larger widths.

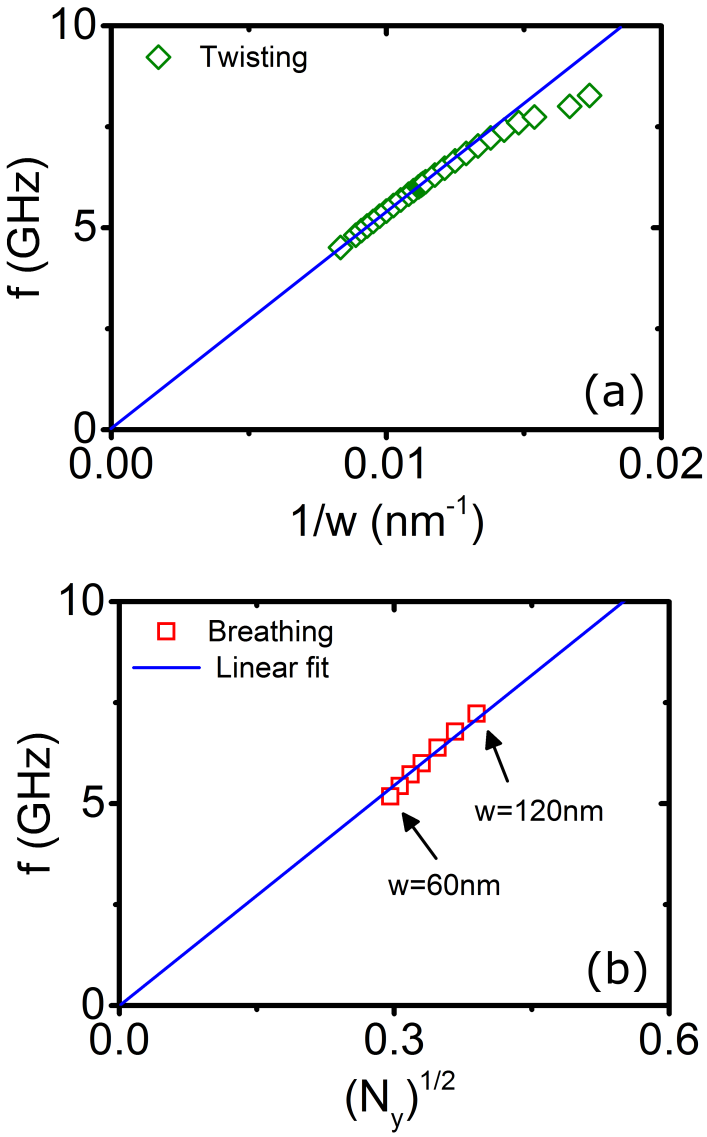

Figure 6.10: (a) f_{twist} versus the inverse strip width. (b) f_{breathe} versus $\sqrt{N_y}$ (see text for N_y calculation) for a number of strip widths. The linear fits have been obtained by constraining the x-axis intercept to zero.

Liu and Grütter have constructed a model for DW width resonances in magnetic films [94] which predicts that f_{breathe} will be proportional to $\sqrt{K_{\mathrm{eff}}}$ where K_{eff} is the effective anisotropy energy associated with the domain wall. For our static TDW (here in a confined geometry rather than a continuous layer), K_{eff} comes from the TDW's demagnetizing energy and can be written as $\frac{1}{2}\mu_0 M_S^2 N_y$ (e.g. [121]), giving $f_{\mathrm{breathe}} \propto \sqrt{N_y}$. Indeed, this relation reproduces the observed f_{breathe} trend relatively well over the entire strip width range, as calculated for a number of strip width values in Fig. 6.10. To determine N_y, we used the same slab approach as used in Sec. 6.3.2.

Chapter 7

Frequency-based nanoparticle sensing over large field ranges using the ferromagnetic resonances of a magnetic nanodisc

The contents of this chapter have been accepted for publication [122] in IOP Nanotechnology and are currently in press. The paper is reproduced below. The work was carried out in collaboration with Dr Peter Metaxas from the University of Western Australia.

In this chapter we use the eigenvalue method implemented in `Finmag` (see Section 4.1.2) to study resonant modes in a thin magnetic disc with dimensions typical of those in out-of-plane magnetized spin torque nano oscillators. In particular, we study the effect of magnetostatic coupling between magnetic nanoparticles and the disc. We identify the resonant dynamic magnetisation modes within the disc using direct magnetic eigenmode calculations and study how these modes are modified in the presence of a nearby magnetic nanoparticle. We demonstrate that particles with properties typical of those under study for biosensing applications can generate changes in the resonant frequency of the fundamental mode which exceed typical oscillator linewidths, enabling frequency-based nanoparticle detection. Furthermore, these shifts can be maintained over large field ranges (here up to 1T) since the resonance frequency responds directly to the nanoparticle stray field (i.e. detection does not rely on nanoparticle-induced changes to the magnetic ground state of the disk).

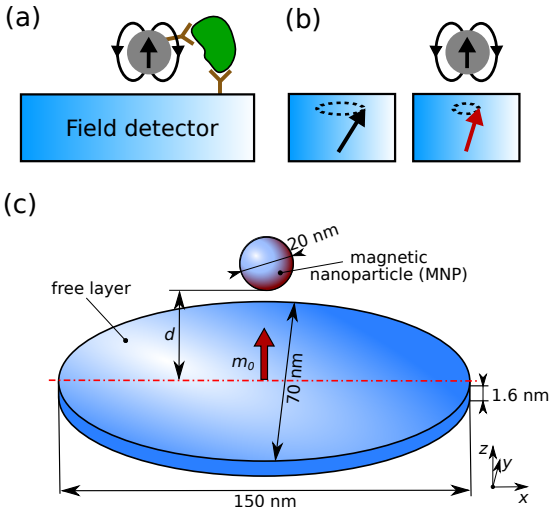

Figure 7.1: (a) Schematic of a biological entity bound to a magnetic field detection device and a magnetic nanoparticle. (b) Schematic of precessional magnetisation dynamics in a bare nano-element (left), and in the presence of a particle which changes the local field and thus the resonant dynamics (right). (c) The geometry used for the finite element simulation, composed of a magnetic nanoparticle and an elliptical magnetic disc. The red arrow indicates the equilibrium magnetisation $\mathbf{m}_0$ of the disc, which points out-of-plane due to perpendicular anisotropy. The centre of the disc is located at $(x, y) = (0, 0)$.

7.1 Introduction

Nano-magnetic and spintronic technologies find application in various sensing scenarios [123–125]. Their appeal in *biological* sensing or 'biosensing' comes partly from the fact that most biomedical samples have a negligible magnetic background enabling matrix-insensitivity [126]. This enables the use of magnetic nanoparticles (MNPs) to tag and subsequently detect biological analytes of interest reliably within a range of bodily fluids [126–128]. Common device setups [128] include sandwich assays [126, 129, 130], where the analyte is immobilised on the sensor surface and sandwiched between two antibodies which bind it to both the sensor and the MNP used for detection (Fig. 7.1(a)), and flow cytometry [131, 132], where the MNP-tagged analyte is detected as it flows through a microfluidic channel. While numerous techniques for particle detection exist [133–139], there has been a strong focus on electronic field sensing technologies employing magnetoresistive stacks [126, 127, 129–132, 140–146] or Hall effect devices [147, 148]. These devices can be used to detect small variations in magnetic field, including those generated by functionalised MNPs, converting the presence of a MNP to a change in the device resistance (typically measured as a voltage).

In conventional ferromagetic magnetoresistive sensors, MNPs induce a change in the static magnetisation configuration of the device's active sensing layer [149]. This translates to a change in the device resistance, enabling electronic nanoparticle detection. However, one may also exploit the magnetic field dependence of ferromagnetic resonance for detection of magnetic fields [150–154] and thus magnetic nanoparticles [104, 154–159]. Notably, the ferromagnetic resonance frequency within the device will respond directly to the field of the MNP (Fig. 7.1(b)), even when the underlying magnetic ground state is unchanged. This opens pathways to intrinsically frequency-based detection schemes [150, 153]. Potential advantages of a frequency-based, dynamic technique over static magnetoresistive sensing include a larger field range over which the device response is linear [150, 160, 161] (enabling larger fields to be applied and thus generate higher MNP moments), intrinsically frequency-based operation (typically at GHz frequencies and thus far from low-frequency $1/f$ contributions), the lack of d.c. voltage-level drift (when using direct frequency measurement) and excellent size scalability [150]. Electrical read-out of dynamics in isolated devices can be carried out using spin torque oscillators (STOs, where d.c. current is used to drive magnetisation dynamics that can then be detected in real time magnetoresistively [162–164]) or by using devices exploiting the inverse spin Hall effect [165] which enables voltage-level-based read-out of dynamics. Although the latter is not a direct frequency-based method (in that dynamics are sensed using a voltage), such a technique can still benefit from the reduced device sizes and larger operational field ranges which come with a switch to sensing based on magnetisation dynamics.

In this work, we use micromagnetic simulations and eigenmode evaluation to quantify the effect of a MNP on resonant modes of precessional magnetisation dynamics in an underlying, out-of-plane magnetised ferromagnetic nanodisc. The simulations demonstrate that the MNP can induce large shifts of the mode frequencies for the disc's quasi-uniform and higher order resonances. At small separations, the shifts notably depend strongly on the position of the particle relative to the regions in the disc where the dynamics associated with each particular mode are concentrated. This is a result of the non-uniform but intense field directly beneath the MNP acting on resonant dynamics within the disc which are also highly spatially non-uniform. At larger separations however, the stray field is weaker and more uniform over the length scale of the disc. This results in a weaker dependence of the frequency shift on the lateral particle position and, as a result, similar responses for all modes (despite their different localisations within the disk). We will also demonstrate that strongly increasing the external field does not significantly compromise device sensitivity (measured in terms of the magnitude of the MNP-induced frequency

shift).

The paper is organised as follows. In Sec. 7.2 we will discuss the system and the simulation method. In Sec. 7.3.1 we present the first five eigenmodes of the bare disk (without an MNP), including spatial profiles and field dependencies of the modes in the presence of *spatially uniform*, out-of-plane magnetic fields. We then present results on MNP-modified modes (Sec. 7.3.2) and show how these modifications depend on both the position of the particle and the profiles of each mode (Sec. 7.3.3). Finally, we discuss the dependence of the frequency shifts on particle parameters and external field strength (Sec. 7.3.4).

7.2 Methods

In Fig. 7.1(c) we show the simulated 1.6 nm thick elliptical nanodisc which has major and minor axis lengths of 150 nm and 70 nm, respectively. A spherical MNP is located above the disc. The separation between the upper surface of the disc and the bottom surface of the MNP is denoted by d. The nanodisc approximates the CoFeB free layer of a STO shown recently to function under low injected current and without strong external magnetic fields [11], properties which may be advantageous for low-power, portable diagnostics [146]. Indeed, exploiting precession of out-of-plane moments in STOs offers excellent potential in terms of achieving low linewidth outputs [161, 166, 167], something which is critical for distinguishing MNP-induced frequency changes. Since we look only at dynamics within the disc, our results can be equally well applied to (arrays of) discs probed using inductive techniques [104] or, as mentioned above, via the inverse spin Hall effect [165] (rather than the dynamic magnetoresistive techniques exploited in STO measurements).

We use the following simulation parameters for the nanodisc [11]: saturation magnetisation $M_\mathrm{s} = 1.1$ MA/m, exchange stiffness $A = 20$ pJ/m and perpendicular magnetic anisotropy constant $K_1 = 0.74$ MJ/m^3. The equilibrium magnetisation $\mathbf{m}_0$ in the bare disc is aligned with the (out-of-plane) $+z$-direction, due to the perpendicular anisotropy (see Fig. 7.1(c)). We also model a 'generic' spherical MNP with saturation magnetisation of 1 MA/m. This magnetisation is higher than that generally expected for saturated iron oxide MNPs (~ 0.25 MA/m) but lower than that observed in high moment FeCo systems [168] (~ 1.8 MA/m assuming a density of ~ 8.3 g/cm^3). Its diameter will be 20 nm unless otherwise specified. The dipole field of the MNP, when uniformly z-magnetised, is

shown in Fig. 7.2. The strong z-component of the MNP's field directly beneath the MNP is clearly visible. Unless otherwise noted, simulations have been run with an external $+z$ field of $0.1\,\mathrm{T}$.

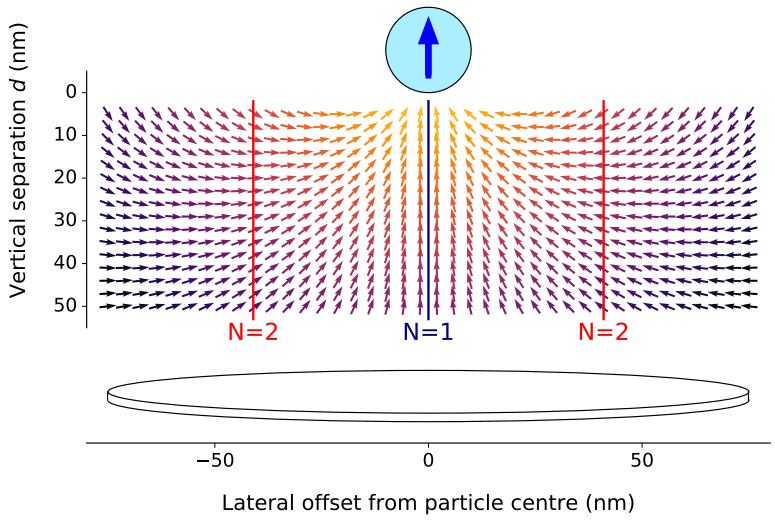

Figure 7.2: Vector field plot of the dipole field generated by a uniformly z-magnetised MNP. The vectors are scaled to uniform length with their colour indicating the field strength (orange is high and violet/black is low). The vertical lines correspond to the x-values where modes 1 and 2 have maxima in their spin precession amplitude (see Fig. 7.3(a)-(b)). A schematic of the nanodisc is shown at the bottom.

We use a finite element based micromagnetic simulation tool inspired by the Nmag package [19] and based on the FEniCS libraries [169]. Sumatra [170, 171], IPython [172], the Jupyter notebook [173], numpy/scipy [174], pandas [175], matplotlib [176] and HoloViews [177] have been used for simulation capture and data analysis. For the computation of the resonant magnetisation modes of the system we employ an eigenvalue problem-based method used recently in Refs. [57, 104] which is similar to that presented by d'Aquino *et al.* [52]. Firstly, we compute the system's equilibrium configuration $\mathbf{m}_0(\mathbf{r})$ and then linearise the Landau-Lifshitz equation for magnetisation dynamics around $\mathbf{m}_0(\mathbf{r})$. This results in a system of linear differential equations for resonant oscillations of the magnetisation, $\mathbf{dm}(\mathbf{r}, t)$, occurring around $\mathbf{m}_0(\mathbf{r})$. This system of differential equations can be written as an eigenvalue problem [57]. The eigenvectors correspond to the resonant eigenmodes [43] of the nanodisc, each occurring at a resonant frequency given by the mode's eigenvalue.

The raw data for the relevant figures in this paper, as well as Jupyter notebooks [173] to reproduce them from this data, are available in the associated electronic supplementary

material for this paper [178].

7.3 Results and discussion

7.3.1 Magnetic eigenmodes of a bare disc

We firstly compute the eigenmodes of the STO's elliptical free layer in the absence of a MNP. In the absence of an external field the obtained resonance frequencies of the first five modes (in order of frequency) are $f_1 = 1.60\,\text{GHz}$, $f_2 = 3.09\,\text{GHz}$, $f_3 = 5.09\,\text{GHz}$, $f_4 = 5.55\,\text{GHz}$ and $f_5 = 7.77\,\text{GHz}$. f_1 is of the same order as the excited mode reported by Zeng *et al.* [11] when extrapolating their data to the zero-current case. Representations of the spatial profiles of mode 1 (most relevant for STOs) as well as the next four higher order modes are shown in Fig. 7.3. The shading encodes the amplitude of the magnetisation precession for each mode, with dark regions representing high amplitude resonant oscillations.

The fundamental $N = 1$ mode (Fig. 7.3(a)) consists of an in-phase precession of all magnetic moments. The precession amplitude is largest at the disc's centre and decays in amplitude towards the boundaries of the free layer. The $N = 2$ mode (Fig. 7.3(b)) is characterised by two regions of large precession amplitude in the left/right halves of the disc, with the magnetic moments in the two parts precessing out-of-phase. Modes 3 and 5 (Figs. 7.3(c, e)) both have multiple nodal axes parallel to the short axis of the ellipse. Mode 4 (Fig. 7.3(d)) is similar to mode 2 but with a nodal axis along the long axis of the disc.

In Fig. 7.4 we show the dependence of each mode frequency on the magnitude of a spatially uniform magnetic field applied along $+z$ (aligned with $\mathbf{m}_0(\mathbf{r})$). The extracted field sensitivities (frequency shift per unit field) of all modes are consistent with one another to within 0.8% and have a value of 28.162 ± 0.108 MHz/mT. As will be shown below, however, the situation is more complex in the presence of a small MNP due to the combination of the localised MNP stray field and spatially non-uniform mode profiles. This will generate a clear dependence of the frequency shifts on the position of the MNP relative to the disc (both in the lateral and vertical directions).

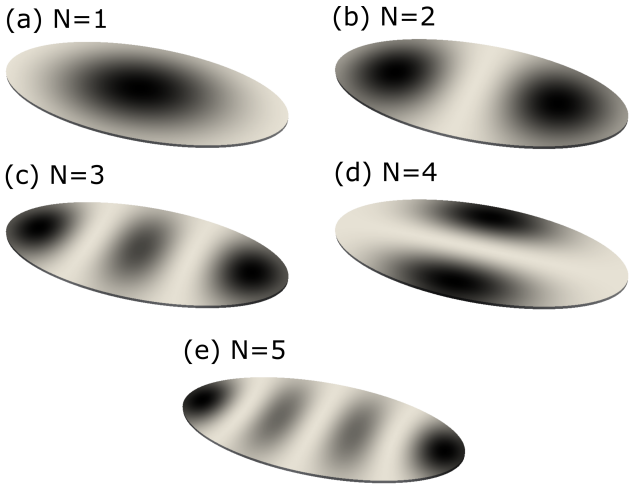

Figure 7.3: Profiles of the first five modes of the bare disc. Dark regions correspond to large-amplitude precessions of the dynamic magnetisation.

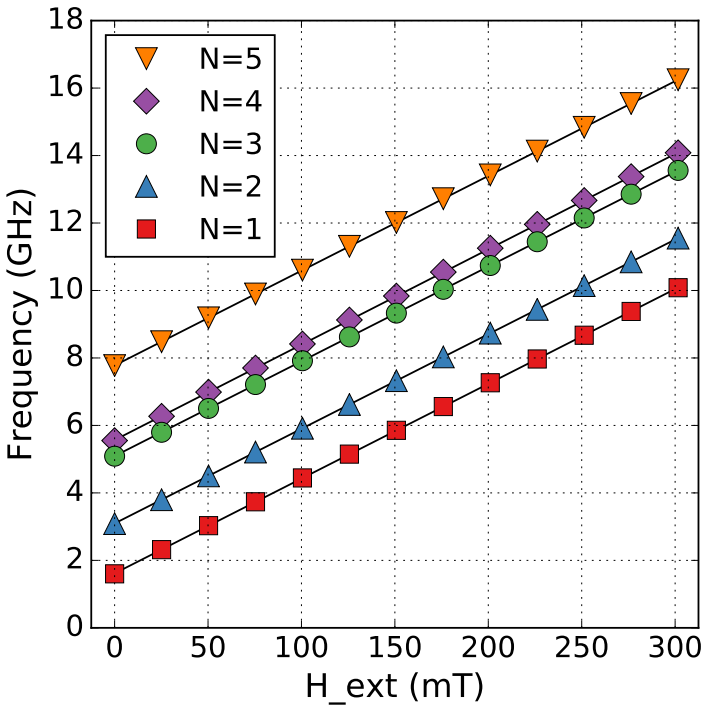

Figure 7.4: Out-of-plane ($+z$) field dependence of the frequencies of the first five modes of the bare disc. Linear regressions (black lines) fitted to the data points demonstrate that the field-induced changes in each eigenfrequency are equivalent to one another to within 0.8%.

7.3.2 MNP-modified eigenmodes

We now introduce a magnetic nanoparticle to the system as per Fig. 7.1(c). It is magnetised in the $+z$-direction, parallel to the applied external field.

In the equilibrium configuration of the bare disc, the disc's free layer magnetisation is parallel to the (out-of-plane) z-axis everywhere due to the strong perpendicular anisotropy. This is illustrated in Fig. 7.5(a), which shows the magnetisation vector field along the disc's long x-axis. If a MNP is present however, its stray field locally modifies the magnetisation. Examples of this are shown in Figs. 7.5(b) and 7.5(c) where the MNP is located at $x = -30$ nm and $x = -60$ nm, respectively, above the major axis ($y = 0$) of the disc at $d = 5$ nm. The presence of the localised MNP field results in a slight localised canting of the magnetisation towards the MNP due to the in-plane components of the stray field. Note, however, that the actual change in the magnetisation orientation is very small. For example, at separation $d = 5$ nm the spatially averaged, normalised out-of-plane magnetisation is 0.99874 and at $d = 20$ nm it is 0.99981. These are both very close to 1, which is the value expected for a perfectly out-of-plane magnetised disc. However, despite only inducing a very small change in the magnetisation configuration, the stray field from the MNP can generate strong changes in the resonant frequency (up to ~ 350 MHz for $N = 1$ at $d = 5$ nm), as will be shown below.

Beyond modifying the resonance precession frequency of the magnetisation, the non-uniformity of the MNP field can also noticeably modify the spatial profile of the eigenmode. An example for the $N = 1$ mode is shown in Fig. 7.6(a), with a MNP at $d = 5$ nm. Although the mode excitations remain in-phase over the entire disc there is a reduced oscillation amplitude directly beneath the MNP, consistent with a MNP-induced, local stiffening of the magnetic moment. This also occurs for the $N = 3$ mode (Fig. 7.6(b)), which is the only other mode studied here that has an antinode (= location of maximum oscillation amplitude) at the disc's centre. Similarly, a left displaced particle (Fig. 7.6(c)) will lead to larger oscillation amplitudes for the $N = 1$ mode on the opposing (right) side of the disc. Somewhat analogously for vortices, a localised out-of-plane field at the core of a vortex can stiffen the core, increasing the frequency of its gyrotropic mode in the small displacement limit [157].

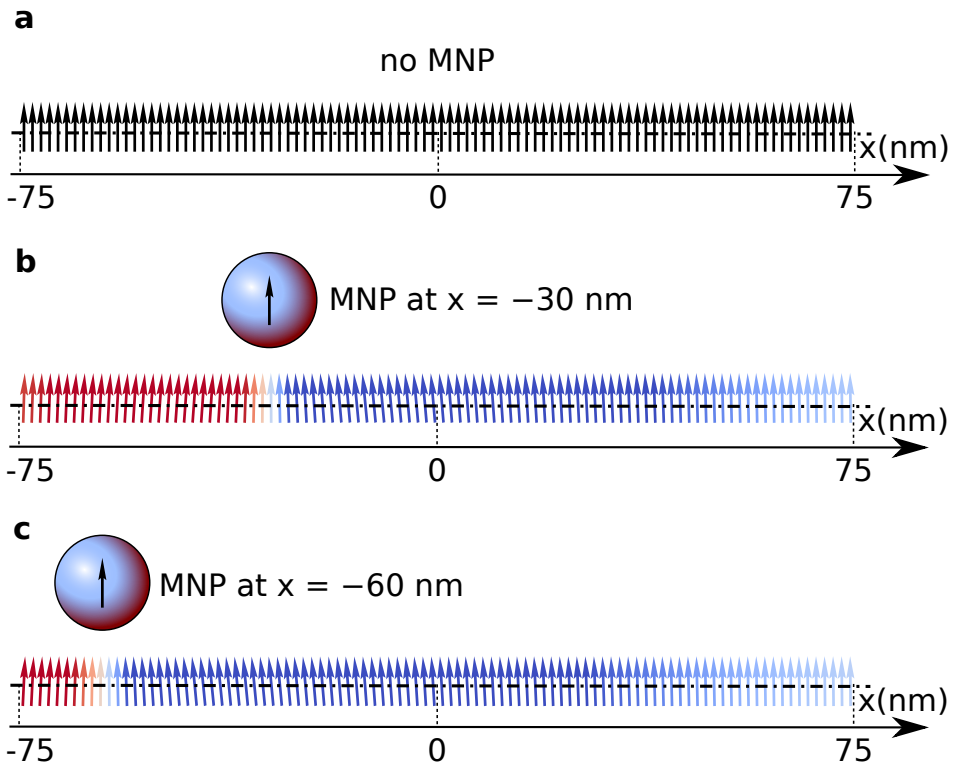

Figure 7.5: Cross section of the equilibrium magnetisation configuration along the x-axis in absence of a MNP (a), and in presence of a MNP ($d = 5$ nm) above the major axis of the disc, at $x = -30$ nm (b) and $x = -60$ nm (c). The colours represent the amount of canting of the magnetisation (magnitude and direction of the m_x-component).

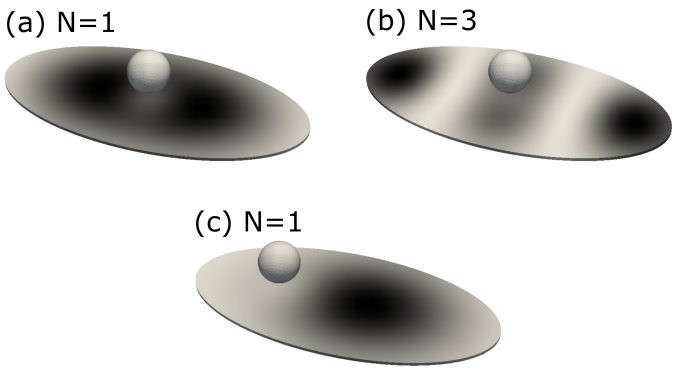

Figure 7.6: Mode profiles with a MNP centred above the disc for $N = 1$ (a) and $N = 3$ (b) as well as for an off-centre MNP for $N = 1$ (c). The MNP-disc separation, d, is 5 nm. Dark regions correspond to large-amplitude precessions of the dynamic magnetisation.

7.3.3 MNP position and height dependence

We now look more closely at the influence of the position of the MNP on the frequency shifts, Δf. In the case of small MNP-disc separations ($d \lessapprox 15$ nm), there is an intense, localised and predominantly $+z$ oriented field directly beneath the MNP (Fig. 7.2). As a result, at these small separations the effect of the MNP on a mode is determined by where the mode's dynamics are concentrated relative to the MNP's location. For MNPs directly above regions where there are high precession amplitudes, there is a frequency upshift ($\Delta f > 0$) due to the increased local z-field below the particle. This result is qualitatively consistent with that seen for uniform $+z$-fields in Fig. 7.4. However, when dynamics are occurring in a region which is laterally offset from the particle and the particle is very close to the disc, the precessing moments can be subject to a field oriented in the $-z$–direction (see again Fig. 7.2), leading to a *reduction* in the frequency ($\Delta f < 0$). We discuss these behaviours below.

Fig. 7.7 shows the Δf values observed for all five eigenmodes ($N = 1, \ldots, 5$) when shifting the MNP along the disc's long axis at vertical separations of $d = 5$, 20 and 50 nm, for lateral MNP positions of $y = 0$ nm and $y = 20$ nm. If the MNP is close to the surface of the disc ($d = 5$ nm, red lines in Fig. 7.7) then Δf closely follows the spatial mode pattern, as can be seen by comparing the red lines in Fig. 7.7 with Fig. 7.3(a)-(e). This reflects the fact that in this case the MNP stray field has a very localised influence on the underlying precessing moments. For example, for $N = 1$ there is a single, broad sensitivity peak near the centre of the disc ($x = 0$ nm) for both values of y, which mirrors that mode's spatial profile. Likewise, the $N = 2$ mode exhibits two sensitivity peaks near $x \approx \pm 40$ nm, i.e. near the locations of the mode's antinodes (see Fig. 7.3(b)). The curve for $N = 3$ shows three such peaks, with the outer ones slightly higher, reflecting the fact that the outer antinodes of this mode have a larger amplitude than the middle one (see Fig. 7.3(c)).

This pattern continues for $N = 4$ and $N = 5$, but while the modes $N = 1, 2, 3$ show fairly similar sensitivities for $y = 0$ nm and $y = 20$ nm, those for $N = 4, 5$ are quite different for both values of y, reflecting the fact that these two modes are less uniform along the short axis of the disc. This is very obvious for $N = 4$ where the mode antinodes are located at $y \approx \pm 25$ nm (Fig. 7.3(d)), leading to a large positive Δf for the laterally y-offset MNP (bottom plot for $N = 4$ in Fig. 7.7).

Comparing the curves obtained for different d values in Fig. 7.7, it is evident that with increasing disc-MNP separations, the shifts are reduced and the curves become more

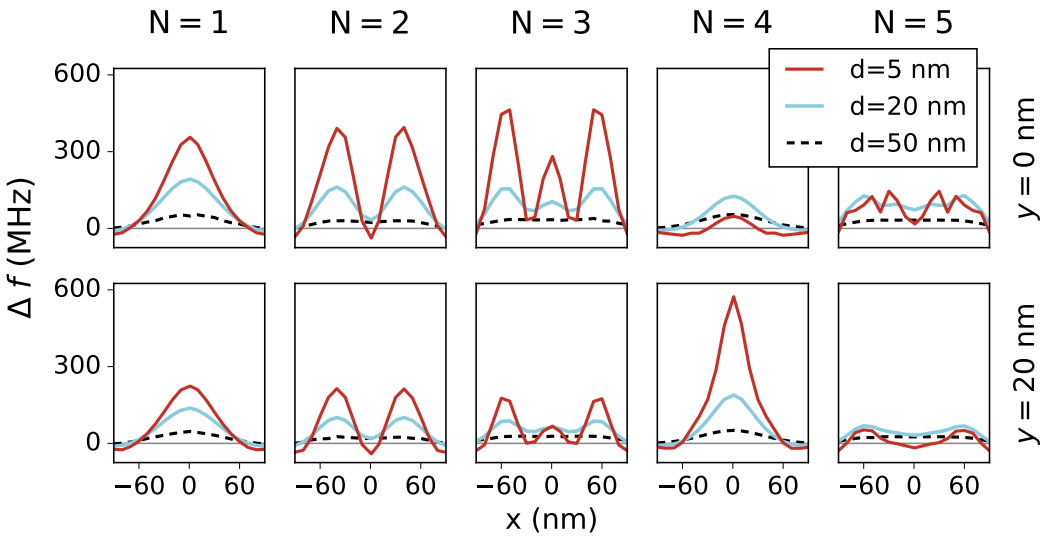

Figure 7.7: Frequency change Δf as a function of lateral particle position x for the first five eigenmodes ($N = 1 - 5$), with the MNP either above the major axis of the ellipse (top row) or shifted by 20 nm in y-direction (bottom row). The frequency change for each mode is shown for three values of the MNP-disc separation (red: $d = 5$ nm, blue: $d = 20$ nm, dashed black: $d = 50$ nm).

homogeneous and indeed comparable for each mode. For an intermediate separation of $d = 20$ nm (solid blue lines), the influence of the mode profiles on the MNP-position-dependent frequency shifts are still visible. However, at a larger separation of $d = 50$ nm (dashed black lines), the Δf curves for each mode become very similar (those for $N = 1, 4$ show a flat, broad peak around the centre of the disc whereas those for $N = 2, 3, 5$ have a more plateau-shaped profile, but the difference is small). This is consistent with two factors: (i) a much more uniform MNP field across the disc at large d (Fig. 7.2) (with a net $+z$-orientation, leading to a frequency increase); and (ii) almost identical sensitivities for each mode in a uniform $+z$-field (Fig. 7.4), leading to similar Δf values for each mode. We note that in the presence of multiple MNPs at similarly large separations (as might occur in real devices) this will likely result in a Δf that is (roughly) proportional to the number of nanoparticles present, due to the fact that all of them induce a similar frequency change, independent of their exact location above the disc.

Fig. 7.8 shows how Δf varies as the vertical separation d is varied for a laterally centred MNP (i.e., one which is laterally positioned at $(x, y) = (0, 0)$). Consistent with the $d = 5$ nm data in Fig. 7.7, the $N = 1$ and $N = 3$ modes, which both have dynamics concentrated below the centred MNP, exhibit the largest Δf at small separations. Furthermore, due to the concentration of dynamics below the MNP, the shifts are positive for

these two modes for all d values. This is because as d is varied there is no sign change in the out-of-plane component of the MNP stray field, $H^{\mathrm{Z}}_{\mathrm{MNP}}$, which acts on the central precessing moments in the disc (cf. blue vertical line in Fig. 7.2). At large distances, all other modes also exhibit a positive Δf which decreases with increasing d, again consistent with what is seen in Fig. 7.7 and discussed above. Note that although the mode $N = 3$ also has an antinode at the disc centre, its Δf is smaller than that seen for N=1 because the the N=3 dynamics are distributed amongst three antinodes (cf. Fig. 7.3(c)), with the outer antinodes being less strongly affected by the centralised MNP.

One can also see in Fig. 7.8 that the frequency shift for modes 2, 4 and 5 *decreases* as d approaches zero. This is because these modes have dynamics concentrated away from the centre of the disc and they are thus exposed to a weaker or even a negative $H^{\mathrm{Z}}_{\mathrm{MNP}}$ at small MNP-disc separations when the MNP is laterally centred above the disc. For example, the frequency shift for $N = 2$ is zero at $d \approx 10$ nm (blue triangles in Fig. 7.8). At this value of d, $H^{\mathrm{Z}}_{\mathrm{MNP}}$ is indeed ≈ 0 near the location where the mode dynamics are concentrated ($x \approx \pm 41$ nm; see the vertical red lines in Fig. 7.2). Note that the exact value of $|x|$ where $H^{\mathrm{Z}}_{\mathrm{MNP}}$ is zero is slightly smaller than 41 nm. This is however not unexpected because the frequency shift will result from what is effectively a convolution between the mode profile and the particle stray field whose magnitude is non-uniform across the disc [149]. We also note that at $x \approx \pm 41$ nm $H^{\mathrm{Z}}_{\mathrm{MNP}}$ becomes negative for values of d smaller than ≈ 15 nm (Fig. 7.2). This is consistent with the observed negative frequency shift for the N=2 mode at very small d in Fig. 7.8. Regarding the $N = 4, 5$ modes, because they have antinodes located closer to the lateral centre of the disc than the $N = 2$ mode (Fig. 7.3) they do not experience a null or negative $H^{\mathrm{Z}}_{\mathrm{MNP}}$ until even smaller MNP-disc separations (as per Fig. 7.2). This is consistent with their $\Delta f = 0$ crossing in Fig. 7.8 occurring at smaller d. Finally, we note that for a particle shifted in the y-direction (and thus lying above the antinode of the $N = 4$ mode), it is the $N = 4$ mode which exhibits the highest Δf (see purple diamonds in inset of Fig. 7.8).

7.3.4 System dependencies of Δf

For sufficiently large read-out signals, detection based on identifying changes to the resonant frequency of a device will ultimately be limited by the resonance linewidth as well as the MNP-induced Δf, with a small linewidth and large Δf being optimal. In the STO study of Zeng *et al.* [11], the minimum observed linewidth of the primary mode (corresponding to the $N = 1$ mode here) was on the order of 30 MHz, suggesting that

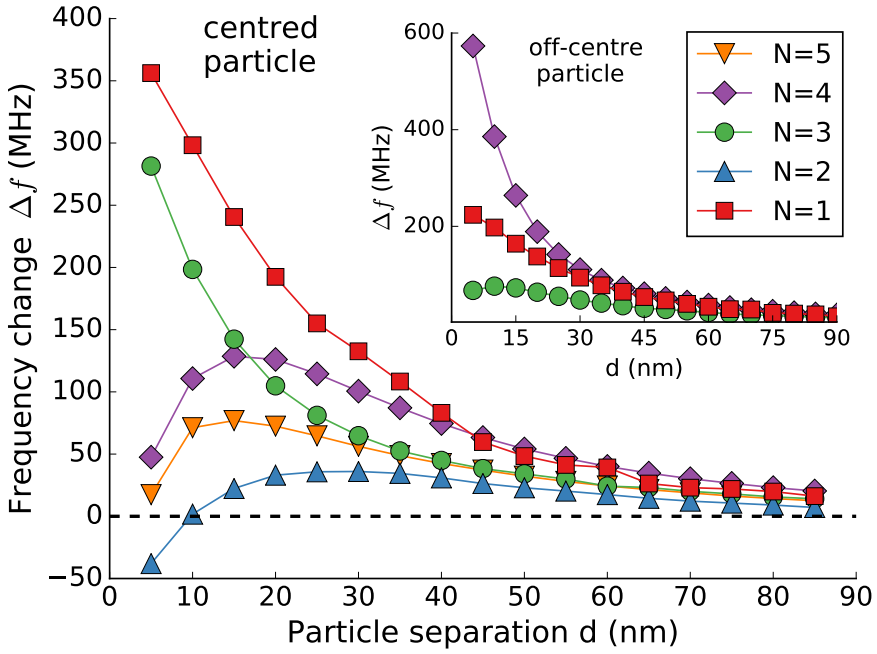

Figure 7.8: Frequency change Δf as a function of particle separation d for a MNP located above the centre of the free layer at $(x, y) = (0, 0)$. The inset shows Δf for the first three modes as a function of d for an off-centre particle at $(x, y) = (0, 20\,\text{nm})$.

detection could be realised for d up to ~ 50 or 60 nm (based on the Δf values shown in Fig. 7.8). This assumes however that such linewidths can be maintained under the fields required to magnetise the MNP and that passivation layers and/or upper contacts can be made sufficiently thin (this is potentially achievable given that typical passivation layers are on the order of 30-50 nm thick [128, 130] and coating layers for MNP biofunctionalisation can be made very thin, on the order of 2-5 nm [128, 179]). We note that lower linewidths [167] (e.g. 6 MHz full-width-half-maximum [161]) have been observed in out-of-plane magnetised STOs. We also note that oscillators based on magnetic vortices can offer even lower linewidths [10, 180, 181], but they also typically have lower field sensitivities, highlighting the need to optimise the sensitivity-to-linewidth ratio if sensing is to be done by directly identifying changes to the frequency. The sensitivity of the specific resonance of the device to *localised* fields [157] is also critical of course.

There are a number of ways to increase Δf without modifying the properties of the nanodisc that is being used as a detector. For example, one can attempt to engineer particles with higher moments (see Fig. 7.9(a), which shows Δf versus particle moment) or increase the size of the particles (see Fig. 7.9(b), showing Δf versus particle diame-

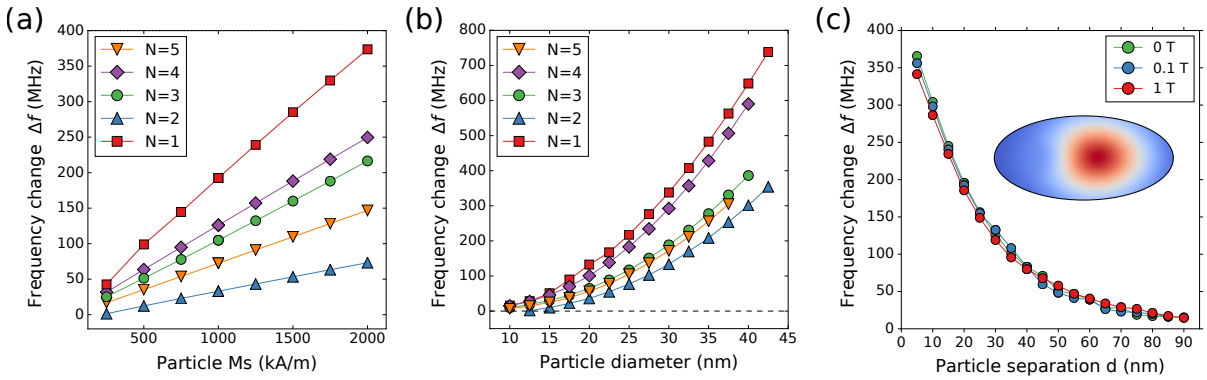

Figure 7.9: (a) Dependence of Δf on the particle's saturation magnetisation M_s for the first five modes, with a particle located above the centre of the disc at separation $d = 20$ nm. (b) Dependence of Δf on particle size for the first five modes, with the separation between the bottom of the particle and the disc surface held constant at $d = 30$ nm. (c) Δf for $N = 1$ for different out-of-plane fields (other simulation parameters unchanged from Fig. 7.8). Inset shows the profile of the fundamental mode $N = 1$ in an external field of strength $\mu_0 H = 1$ T with a particle (not shown) off-centre at $x = -30$ nm, $d = 5$ nm.

ter). In both cases, this increases the MNP-generated magnetic stray fields and thus the resultant shifts. However, oft-used iron-oxide particles will have lower moments and thus generate lower shifts. We note that in contrast to the case of magnetic vortices [157], for this system we saw monotonic increases in Δf when increasing the particle size (and moment).

The time-averaged moment of superparamagnetic particles can also be increased by increasing the applied field. Thanks to the continued linearity of Δf as a function of the external field strength $\mathbf{H}_\mathrm{ext}$ over a large range of field values (Fig. 7.4), the external field can be increased without significantly compromising Δf. Indeed, we see good consistency between the calculated Δf values obtained at vastly differing fields of 0 T, 0.1 T and 1 T (shown for $N = 1$ in Fig. 7.9(c)). Note that here we (unphysically) assume the same particle moment at each field to enable direct comparison of the Δf values. We note that at high field (1 T), the particle still clearly modifies the distribution of the dynamics of the $N = 1$ mode (shown for a laterally offset particle in the inset of Fig. 7.9(c)). The retained sensitivity of this system even in large external fields is in contrast to magnetoresistive sensors whose sensitivities will be almost nil when the magnetisation is (quasi-)uniform in a sufficiently high field.

7.4 Conclusion

Using finite element micromagnetic simulations, we have shown how localised magnetic fields generated by magnetic nanoparticles (typically having diameters of 20 nm) modify the spatial profiles and frequencies of confined ferromagnetic resonances in underlying out-of-plane-magnetised ferromagnetic nanodiscs. By electrically detecting these resonances, nanoparticle-induced modifications to the resonances can be exploited to create nano-scale, frequency-based nanoparticle detectors for applications such as solid-state bio-detection [150].

Due to the non-uniform spatial profiles of resonant mode dynamics, the observed shifts (exceeding 300 MHz in some cases) can depend strongly on the position of the nanoparticle. This is most obvious for small disc-particle separations, where small regions of the disc will be subject to the intense magnetic field localised directly beneath the particle. In this case, the shifts are maximised when the particle is above those regions where the spins are undergoing the highest amplitude precessional dynamics. At larger separations, the disc will be subject to a weaker but more uniform field, which leads to shifts that are smaller (~ 20 MHz at an 80 nm vertical separation) but also less dependent on the lateral particle position. It was also shown that it is possible to maintain large nanoparticle-induced frequency shifts over a wide range of external fields, exploiting the fact that detection is dependent on the action of the field on the resonant dynamics rather than a change to the static magnetisation configuration within the device. The ability to detect frequency changes experimentally will depend on the linewidth of the measured signal relative to the nanoparticle-induced frequency changes. The latter can be optimised by having small particle-disc separations and/or large particle moments (with the moment being maximised when the external field is large, for optimised nanoparticle compositions, and/or of course for larger particles).

Chapter 8

Summary and Conclusions

In this work we have used the micromagnetic software packages `Nmag` and `Finmag`, developed at the University of Southampton, to model different kinds of magnetic nanostructures. The main focus has been on domain walls in nanowires and resonant modes of magnetic nanodiscs, with applications to magnetic storage and nano-sensing devices.

In Chapter 3 a new model was developed in order to study edge roughness in magnetic nanowires in a more systematic and more realistic way than has previously been possible with other simulation packages. The classical Walker breakdown was observed, but additional phenomena occurred in rough geometries that do not exist in smooth nanowires, such as dynamic domain wall pinning at constrictions. The asymptotic behaviour of the domain wall was largely unaffected by the roughness, despite the fact that it introduced marked local alterations to the domain wall trajectories, especially in the oscillatory regime above the Walker breakdown where the length and shape of individual oscillation cycles was altered due to the interaction of the domain wall with the roughness features. As a somewhat surprising consequence, in this regime stronger applied fields are *more* likely to dynamically pin the domain wall because the resulting shorter oscillation cycles give it more opportunity to interact with the roughness. It was found that the effective pinning strength of roughness features is strongest when their size is comparable with that of the domain wall. One limitation of the presented model is that it only considers edge roughness, whereas real nanowires also exhibit other types, such as surface roughness. Studying those effects could be the topic of future work.

In Chapter 4 we presented a detailed discussion of the two main methods for computing resonant modes in magnetic nanostructures: the ringdown method and an eigenvalue-based method. The implementation of the latter in a finite element context was explained in detail, including the key advantages over the ringdown method. We also discussed

certain limitations with respect to memory requirements and speed of the implementation in `Finmag` caused by the finite element discretisation scheme. Further optimisation of our implementation would be a promising topic for further research because it could potentially lead to a significant speed-up and a greatly reduced memory footprint, enabling the simulation of much larger systems. However, it would involve working around the issues posed by the standard algorithms in use for finite element micromagnetics (in particular, the way in which the demagnetising field is computed and the use of the box scheme for the approximation of the effective field). Despite these minor limitations, the implementation of the eigenvalue method in `Finmag` has been successfully applied to a variety of different magnetic nanosystems and resulted in multiple publications described in later chapters.

Our implementation of the eigenvalue method was verified by reproducing results from an independent study by Carlotti et al. [51] Despite the different simulation methods – Carlotti et al. use a ringdown approach with a finite difference micromagnetic solver, whereas our calculations use a finite element-based implementation of the eigenvalue method – there is excellent agreement in the results. Minor discrepancies in the computed eigenfrequencies are due to the use of thermal excitations in the ringdown simulations, which are not present in our simulations.

In Chapter 6 the eigenvalue method was applied to a study of different kinds of resonant modes (translational, breathing and twisting) occurring in domain walls pinned at notches in a magnetic nanowire. It was shown that these different kinds of modes exhibit different sensititivies to alterations in the notch shapes and to changes in the nanowire geometry, and these are discussed in detail. As the width of the nanowire is varied, the breathing and twisting modes become frequency-degenerate. The eigenvalue method enabled us to study the behaviour at this frequency-crossing, which would not have been possible with a ringdown approach. Similarly, computing the eigenfrequencies in applied fields close to the depinning field of the domain wall was only possible using this eigenvalue-based approach.

In Chapter 7 we presented a study of resonant modes of an elliptical nanodisc resembling the free layer in a spin-torque nano-oscillator. We explored how these modes are altered in the presence of a magnetic nanoparticle, which has applications for the development of novel biosensing devices. The results show that there is a strong modification of the eigenmode frequencies and spatial mode profiles caused by the stray field of the particle. The resulting eigenfrequency shifts can be maintained over large external field ranges because they do not rely on a modification of the magnetic ground state of the disc but are rather

a direct response to the nanoparticle stray field. For the studied particle characteristics these frequency alterations are larger than achievable linewidths in state-of-the-art spin-torque oscillators, assuming that devices can be fabricated with sufficiently thin contacts and capping layers to allow the particle to be close enough to the disc. As we showed, changing the particle characteristics (for example, increasing the size or choosing a material with higher saturation magnetisation) will increase the frequency shifts and thus make detection easier. These results have promising applications for the development of nanosensors with better sensitivity than existing devices.

Bibliography

[1] S. Hettrick. *It's impossible to conduct research without software, say 7 out of 10 UK researchers | Software Sustainability Institute*. Software Sustainability Institute Blog. 2014. URL: http://www.software.ac.uk/blog/2014-12-04-its-impossible-conduct-research-without-software-say-7-out-10-uk-researchers (accessed on 03/24/2016).

[2] V. E. Demidov, S. Urazhdin, and S. O. Demokritov. "Direct observation and mapping of spin waves emitted by spin-torque nano-oscillators". In: *Nature Materials* 9.12 (2010), pp. 984–988.

[3] S. I. Kiselev et al. "Microwave oscillations of a nanomagnet driven by a spin-polarized current". In: *Nature* 425.6956 (2003), pp. 380–383.

[4] H. Kubota et al. "Quantitative measurement of voltage dependence of spin-transfer torque in MgO-based magnetic tunnel junctions". In: *Nature Physics* 4.1 (2008), pp. 37–41.

[5] C. Wang et al. "Time-resolved measurement of spin-transfer-driven ferromagnetic resonance and spin torque in magnetic tunnel junctions". In: *Nature Physics* 7.6 (2011), pp. 496–501.

[6] X. W. Yu et al. "Images of a Spin-Torque-Driven Magnetic Nano-Oscillator". In: *Physical Review Letters* 106.16 (2011), p. 167202.

[7] C. Serpico et al. "Nonlinear Magnetization Dynamics in Nanomagnets". In: *Handbook of Magnetism and Advanced Magnetic Materials*. John Wiley & Sons, Ltd, 2007.

[8] E. C. Stoner and E. P. Wohlfarth. "A mechanism of magnetic hysteresis in heterogeneous alloys". In: *IEEE Transactions on Magnetics* 27.4 (1991), pp. 3475–3518.

[9] W. F. Brown. *Micromagnetics*. New York: Interscience Publishers, 1963.

[10] V. S. Pribiag et al. "Magnetic vortex oscillator driven by d.c. spin-polarized current". In: *Nature Physics* 3.7 (2007), pp. 498–503.

[11] Z. Zeng et al. “Ultralow-current-density and bias-field-free spin-transfer nano-oscillator”. In: *Scientific Reports* 3 (2013), p. 1426.

[12] N. L. Schryer and L. R. Walker. “The motion of 180° domain walls in uniform dc magnetic fields”. In: *Journal of Applied Physics* 45.12 (1974), pp. 5406–5421.

[13] J. C. Slonczewski. “Current-driven excitation of magnetic multilayers”. In: *Journal of Magnetism and Magnetic Materials* 159.1–2 (1996), pp. L1–L7.

[14] L. Berger. “Emission of spin waves by a magnetic multilayer traversed by a current”. In: *Physical Review B* 54.13 (1996), pp. 9353–9358.

[15] S. S. P. Parkin, M. Hayashi, and L. Thomas. “Magnetic Domain-Wall Racetrack Memory”. In: *Science* 320.5873 (2008), pp. 190–194.

[16] A. Aharoni. *Introduction to the Theory of Ferromagnetism*. 2 edition. Oxford ; New York: Oxford University Press, 2001.

[17] W. Scholz et al. “Scalable parallel micromagnetic solvers for magnetic nanostructures”. In: *Computational Materials Science*. Proceedings of the Symposium on Software Development for Process and Materials Design 28.2 (2003), pp. 366–383.

[18] J. Fidler and T. Schrefl. “Micromagnetic modelling - the current state of the art”. In: *Journal of Physics D: Applied Physics* 33.15 (2000), R135.

[19] T. Fischbacher et al. “A Systematic Approach to Multiphysics Extensions of Finite-Element-Based Micromagnetic Simulations: Nmag”. In: *IEEE Transactions on Magnetics* 43.6 (2007), pp. 2896–2898.

[20] M. Albert et al. “Domain wall motion in perpendicular anisotropy nanowires with edge roughness”. In: *Journal of Physics: Condensed Matter* 24.2 (2012), p. 024219.

[21] Y. Nakatani, A. Thiaville, and J. Miltat. “Faster magnetic walls in rough wires”. In: *Nature Materials* 2.8 (2003), pp. 521–523.

[22] P. J. Metaxas et al. “Creep and Flow Regimes of Magnetic Domain-Wall Motion in Ultrathin Pt/Co/Pt Films with Perpendicular Anisotropy”. In: *Physical Review Letters* 99.21 (2007), p. 217208.

[23] K.-J. Kim et al. “Interdimensional universality of dynamic interfaces”. In: *Nature* 458.7239 (2009), pp. 740–742.

[24] G. Rodríguez-Rodríguez et al. “Interplay between collective pinning and artificial defects on domain wall propagation in Co/Pt multilayers”. In: *Journal of Physics D: Applied Physics* 43.30 (2010), p. 305002.

[25] M. Kläui et al. “Controlled and Reproducible Domain Wall Displacement by Current Pulses Injected into Ferromagnetic Ring Structures”. In: *Physical Review Letters* 94.10 (2005), p. 106601.

[26] M. Hayashi et al. “Influence of Current on Field-Driven Domain Wall Motion in Permalloy Nanowires from Time Resolved Measurements of Anisotropic Magnetoresistance”. In: *Physical Review Letters* 96.19 (2006), p. 197207.

[27] M.-Y. Im et al. “Direct Observation of Stochastic Domain-Wall Depinning in Magnetic Nanowires”. In: *Physical Review Letters* 102.14 (2009), p. 147204.

[28] L. Bocklage et al. “Dependence of Magnetic Domain-Wall Motion on a Fast Changing Current”. In: *Physical Review Letters* 103.19 (2009), p. 197204.

[29] A. Vogel et al. “Domain-Wall Pinning and Depinning at Soft Spots in Magnetic Nanowires”. In: *IEEE Transactions on Magnetics* 46.6 (2010), pp. 1708–1710.

[30] A. Vogel et al. “Field- and current-induced domain-wall motion in permalloy nanowires with magnetic soft spots”. In: *Applied Physics Letters* 98.20 (2011), p. 202501.

[31] H. Min et al. “Effects of Disorder and Internal Dynamics on Vortex Wall Propagation”. In: *Physical Review Letters* 104.21 (2010), p. 217201.

[32] G. Tatara et al. “Threshold Current of Domain Wall Motion under Extrinsic Pinning, ß-Term and Non-Adiabaticity”. In: *Journal of the Physical Society of Japan* 75.6 (2006), p. 064708.

[33] E. Martinez et al. “Thermal effects in domain wall motion: Micromagnetic simulations and analytical model”. In: *Physical Review B* 75.17 (2007), p. 174409.

[34] J. Ryu and H.-W. Lee. “Current-induced domain wall motion: Domain wall velocity fluctuations”. In: *Journal of Applied Physics* 105.9 (2009), p. 093929.

[35] A Thiaville et al. “Micromagnetic understanding of current-driven domain wall motion in patterned nanowires”. In: *Europhysics Letters (EPL)* 69.6 (2005), pp. 990–996.

[36] *Nmag - A micromagnetic simulation environment*. URL: http://nmag.soton.ac.uk/ (accessed on 03/24/2016).

[37] H. Tanigawa et al. “Domain Wall Motion Induced by Electric Current in a Perpendicularly Magnetized Co/Ni Nano-Wire”. In: *Applied Physics Express* 2.5 (2009), p. 053002.

[38] C. Burrowes et al. “Non-adiabatic spin-torques in narrow magnetic domain walls”. In: *Nature Physics* 6.1 (2010), pp. 17–21.

[39] T. Fischbacher et al. “Parallel execution and scriptability in micromagnetic simulations”. In: *Journal of Applied Physics* 105.7 (2009), p. 07D527.

[40] W. H. Press et al. *Numerical Recipes in C: The Art of Scientific Computing, Second Edition*. 2 edition. Cambridge ; New York: Cambridge University Press, 1992.

[41] B. A. Lilley. “LXXI. Energies and widths of domain boundaries in ferromagnetics”. In: *The London, Edinburgh, and Dublin Philosophical Magazine and Journal of Science* 41.319 (1950), pp. 792–813.

[42] H. Kronmüller and M. Fähnle. *Micromagnetism and the Microstructure of Ferromagnetic Solids*. 1 edition. New York: Cambridge University Press, 2003.

[43] A. Baker et al. “Proposal of a micromagnetic standard problem for ferromagnetic resonance simulations”. In: *Journal of Magnetism and Magnetic Materials* 421 (2017), pp. 428 –439.

[44] R. D. McMichael and M. D. Stiles. “Magnetic normal modes of nanoelements”. In: *Journal of Applied Physics* 97.10 (2005), 10J901.

[45] P. E. Roy, T. Trypiniotis, and C. H. W. Barnes. “Micromagnetic simulations of spin-wave normal modes and the resonant field-driven magnetization dynamics of a 360° domain wall in a soft magnetic stripe”. In: *Physical Review B* 82.13 (2010), p. 134411.

[46] M. Buess et al. “Fourier Transform Imaging of Spin Vortex Eigenmodes”. In: *Physical Review Letters* 93.7 (2004), p. 077207.

[47] M. Albert et al. *Code and data for micromagnetic standard problem on ferromagnetic resonance*. 2016. URL: http://dx.doi.org/10.5281/zenodo.59714.

[48] T. E. Oliphant. “Python for Scientific Computing”. In: *Computing in Science & Engineering* 9.3 (2007), pp. 10–20.

[49] I. Neudecker et al. “Spatially Resolved Dynamic Eigenmode Spectrum of Co Rings”. In: *Physical Review Letters* 96.5 (2006), p. 057207.

[50] G. Venkat et al. “Proposal for a Standard Micromagnetic Problem: Spin Wave Dispersion in a Magnonic Waveguide”. In: *IEEE Transactions on Magnetics* 49.1 (2013), pp. 524–529.

[51] G. Carlotti et al. “Exchange-dominated eigenmodes in sub-100 nm permalloy dots: A micromagnetic study at finite temperature”. In: *Journal of Applied Physics* 115.17 (2014), p. 17D119.

[52] M. d'Aquino et al. "A novel formulation for the numerical computation of magnetization modes in complex micromagnetic systems". In: *Journal of Computational Physics* 228.17 (2009), pp. 6130–6149.

[53] Z. Bai et al., eds. *Templates for the Solution of Algebraic Eigenvalue Problems: A Practical Guide*. Software, Environments and Tools. SIAM, 2000.

[54] D. Fredkin and T. Koehler. "Hybrid method for computing demagnetizing fields". In: *IEEE Transactions on Magnetics* 26.2 (1990), pp. 415–417.

[55] *MicroMagus*. MicroMagus: Software package for micromagnetic simulations. URL: http://www.micromagus.de/ (accessed on 03/22/2016).

[56] *WebPlotDigitizer - Extract data from plots, images, and maps*. URL: http://arohatgi.info/WebPlotDigitizer/ (accessed on 02/22/2016).

[57] P. J. Metaxas et al. "Resonant translational, breathing, and twisting modes of transverse magnetic domain walls pinned at notches". In: *Physical Review B* 93.5 (2016), p. 054414.

[58] X. Wang et al. "Spintronic Memristor Through Spin-Torque-Induced Magnetization Motion". In: *IEEE Electron Device Letters* 30.3 (2009), pp. 294–297.

[59] N. Locatelli, V. Cros, and J. Grollier. "Spin-torque building blocks". In: *Nature Materials* 13.1 (2014), pp. 11–20.

[60] M. Donolato et al. "On-Chip Manipulation of Protein-Coated Magnetic Beads via Domain-Wall Conduits". In: *Advanced Materials* 22.24 (2010), pp. 2706–2710.

[61] E. Rapoport, D. Montana, and G. S. D. Beach. "Integrated capture, transport, and magneto-mechanical resonant sensing of superparamagnetic microbeads using magnetic domain walls". In: *Lab on a Chip* 12.21 (2012), p. 4433.

[62] E. Saitoh et al. "Current-induced resonance and mass determination of a single magnetic domain wall". In: *Nature* 432.7014 (2004), pp. 203–206.

[63] J. Winter. "Bloch wall excitation. Application to nuclear resonance in a Bloch wall". In: *Physical Review* 124.2 (1961), p. 452.

[64] A. Rebei and O. Mryasov. "Dynamics of a trapped domain wall in a spin-valve nanostructure with current perpendicular to the plane". In: *Phys. Rev. B* 74 (1 2006), p. 014412.

[65] D Bedau et al. "Detection of Current-Induced Resonance of Geometrically Confined Domain Walls". In: *Physical Review Letters* 99 (2007), p. 146601.

[66] L Thomas et al. “Resonant Amplification of Magnetic Domain-Wall Motion by a Train of Current Pulses”. In: *Science* 315 (2007), pp. 1553–1556.

[67] R. Moriya et al. “Probing vortex-core dynamics using current-induced resonant excitation of a trapped domain wall”. In: *Nat Phys* 4.5 (2008), pp. 368–372.

[68] C. W. Sandweg et al. “Modification of the thermal spin-wave spectrum in a $Ni_{81}Fe_{19}$ stripe by a domain wall”. In: *J. Phys. D: Appl. Phys.* 41 (2008), p. 164008.

[69] L. Bocklage et al. “Analytical modeling and x-ray imaging of oscillations of a single magnetic domain wall”. In: *Phys. Rev. B* 81.5 (2010), p. 054404.

[70] L. O’Brien et al. “Dynamic Oscillations of Coupled DomainWalls”. In: *Phys. Rev. Lett.* 108 (2012), p. 187202.

[71] L. Bocklage et al. “Spin waves and domain wall modes in curved magnetic nanowires”. In: *J. Phys.: Condens. Matter* 26.26 (2014), p. 266003.

[72] A. T. Galkiewicz et al. “Resonance in magnetostatically coupled transverse domain walls”. In: *Phys. Rev. B* 90.2 (2014).

[73] S. Sangiao and M. Viret. “Electrical detection of internal dynamical properties of domain walls”. In: *Phys. Rev. B* 89.10 (2014), p. 104412.

[74] S. Lequeux et al. “Increased magnetic damping of a single domain wall and adjacent magnetic domains detected by spin torque diode in a nanostripe”. In: *Appl. Phys. Lett.* 107 (2015), p. 182404.

[75] S Lepadatu et al. “Domain-wall spin-torque resonators for frequency-selective operation”. In: *Physical Review B* 81 (2010), 060402(R).

[76] C Bayer et al. “Phase Shift of Spin Waves Traveling Through a 180° Bloch-Domain Wall”. In: *IEEE Trans. Mag.* 41 (2005), p. 3094.

[77] S. J. Hermsdoerfer et al. “A spin-wave frequency doubler by domain wall oscillation”. In: *Appl. Phys. Lett.* 94.22 (2009), p. 223510.

[78] Y. Le Maho, J.-V. Kim, and G. Tatara. “Spin-wave contributions to current-induced domain wall dynamics”. In: *Phys. Rev. B* 79.17 (2009), p. 174404.

[79] D. S. Han et al. “Magnetic domain-wall motion by propagating spin waves”. In: *Appl. Phys. Lett* 94 (2009), p. 112502.

[80] M Jamali, H Yang, and K. J. Lee. “Spin wave assisted current induced magnetic domain wall motion”. In: *Appl. Phys. Lett.* 96 (2010), p. 242501.

[81] A. Janutka. “Resonance of Spin Waves and Domain-Wall Excitations in Ferromagnetic Stripes”. In: *IEEE Mag. Lett.* 4 (2013), pp. 4000104–4000104.

[82] X. G. Wang et al. “Microwave-assisted domain-wall motion induced by alternating spin-polarized current”. In: *Phys. Rev. B* 89.14 (2014), p. 144418.

[83] T Nozaki et al. “Substatial reduction in the depinning field of vortex domain walls triggeredby spin-transfer induced resonance”. In: *Applied Physics Letters* 91 (2007), p. 082502.

[84] E Martinez et al. “Resonant domain wall depinning induced by oscillating spin-polarized currentsin thin ferromagnetic strips”. In: *Physical Review B* 77 (2008), p. 144417.

[85] P. J. Metaxas et al. “Current-induced resonant depinning of a transverse magnetic domain wall in a spin valve nanostrip”. In: *Appl. Phys. Lett.* 97 (2010), p. 182506.

[86] D Petit et al. “Domain wall pinning and potential landscapes created by constrictions and protrusions in ferromagnetic nanowires”. In: *Journal of Applied Physics* 103 (2008), p. 114307.

[87] L. Bogart et al. “Dependence of domain wall pinning potential landscapes on domain wall chirality and pinning site geometry in planar nanowires”. In: *Phys. Rev. B* 79.5 (2009), p. 054414.

[88] A Kunz and J. D. Priem. “Dynamic Notch Pinning fields for Domain Walls in Ferromagnetic Nanowires”. In: *IEEE Trans. Mag.* 46 (2010), p. 1559.

[89] J. A. Currivan et al. “Polymethyl methacrylate/hydrogen silsesquioxane bilayer resist electron beam lithography process for etching 25 nm wide magnetic wires”. In: *J. Vac. Sci. Technol. B* 32.2 (2014), p. 021601.

[90] Y Nakatani, A Thiaville, and J Miltat. “Head-to-head domain walls in soft nanostrips: a refined phase diagram”. In: *Journal of Magnetism and Magnetic Materials* 290 (2005), p. 750.

[91] J. Rhensius et al. “Imaging of Domain Wall Inertia in Permalloy Half-Ring Nanowires by Time-Resolved Photoemission Electron Microscopy”. In: *Physical Review Letters* 104.6 (2010), p. 067201.

[92] X.-G. Wang et al. “Spin-transfer torque induced domain wall ferromagnetic resonance in nanostrips”. In: *Journal of Magnetism and Magnetic Materials* 332 (2013), pp. 56–60.

[93] R. L. Stamps, A. S. Carriço, and P. E. Wigen. “Domain-wall resonance in exchange-coupled magnetic films”. In: *Physical Review Letters* 55 (1997), p. 6473.

[94] Y Liu and P Grütter. “Theory of magnetoelastic dissipation due to domain wall width oscillation”. In: *Journal of Applied Physics* 83 (1998), p. 5922.

[95] A. L. Dantas, M. S. Vasconcelos, and A. S. Carriço. “Breathing domain wall mode of an interface pinned Néel wall”. In: *J. Magn. Magn. Mater* 226 (2001), p. 1604.

[96] K. Matsushita et al. “AC-Driven Breathing Mode of Confined Magnetic Domain Wall”. In: *J. Phys. Soc. Jpn* 81.4 (2012), p. 043801.

[97] M Mori et al. “Possible method to observe the breathing mode of magnetic domain wall in the Josephson junction”. In: *J. Phys.: Condens. Matter* 26 (2014), p. 255702.

[98] K. Matsushita, M. Sasaki, and T. Chawanya. “Swing Casting Boost for Confined Domain Wall Breathing”. In: *J. Phys. Soc. Jpn.* 83.1 (2014), p. 013801.

[99] D Bedau et al. “Quantitative Determination of the Nonlinear Pinning Potential for a Magnetic Domain Wall”. In: *Physical Review Letters* 101 (2008), p. 256602.

[100] M. Grimsditch et al. “Normal modes of spin excitations in magnetic nanoparticles”. In: *Physical Review B* 69.17 (2004), p. 174428.

[101] M. Dvornik et al. “Collective magnonic modes of pairs of closely spaced magnetic nano-elements”. In: *Journal of Applied Physics* 109.7 (2011), 07B912.

[102] V. V. Naletov et al. “Identification and selection rules of the spin-wave eigenmodes in a normally magnetized nanopillar”. In: *Physical Review B* 84.22 (2011), p. 224423.

[103] R. Zivieri and G. Consolo. “Hamiltonian and Lagrangian Dynamical Matrix Approaches Applied to Magnetic Nanostructures”. In: *Adv. Cond. Matt. Phys.* 2012 (2012), p. 1.

[104] P. J. Metaxas et al. “Sensing magnetic nanoparticles using nano-confined ferromagnetic resonances in a magnonic crystal”. In: *Applied Physics Letters* 106.23 (2015), p. 232406.

[105] G. S. Abo et al. “Definition of Magnetic Exchange Length”. In: *IEEE Trans. Mag.* 49 (2013), p. 4937.

[106] V. Uhlir et al. “Direct observation of Oersted-field-induced magnetization dynamics in magnetic nanowires”. In: *Phys. Rev. B* 83 (2011), 020406R.

[107] A. Khvalkovskiy et al. “High Domain Wall Velocities due to Spin Currents Perpendicular to the Plane”. In: *Physical Review Letters* 102 (2009), p. 067206.

[108] A Chanthbouala et al. “Vertical-current-induced domain-wall motion in MgO-based magnetic tunnel junctions with low current densities”. In: *Nat. Phys.* 7 (2011), p. 626.

[109] P. J. Metaxas et al. “High domain wall velocities via spin transfer torque using vertical current injection”. In: *Sci. Rep.* 3 (2013), p. 1829.

[110] J. Sampaio et al. “Time-resolved observation of fast domain-walls driven by vertical spin currents in short tracks”. In: *Applied Physics Letters* 103.24 (2013), p. 242415.

[111] C. T. Boone et al. “Rapid Domain Wall Motion in Permalloy Nanowires Excited by a Spin-Polarized Current Applied Perpendicular to the Nanowire”. In: *Physical Review Letters* 104 (2010), p. 097203.

[112] A. V. Khvalkovskiy et al. “Matching domain-wall configuration and spin-orbit torques for efficient domain-wall motion”. In: *Physical Review B* 87.2 (2013).

[113] K.-S. Ryu et al. “Chiral spin torque at magnetic domain walls”. In: *Nat. Nanotechnol.* 8.7 (2013), pp. 527–533.

[114] S. Emori et al. “Current-driven dynamics of chiral ferromagnetic domain walls”. In: *Nat Mater* 12.7 (2013), pp. 611–616.

[115] L Thomas et al. “Oscillatory dependence of current-driven magnetic domain wall motion oncurrent pulse length”. In: *Nature* 443 (2006), p. 197.

[116] G. Tatara and H. Kohno. “Theory of Current-Driven Domain Wall Motion: Spin Transfer versus Momentum Transfer”. In: *Physical Review Letters* 92.8 (2004), p. 086601.

[117] B Krüger. “Current-Driven Magnetization Dynamics: Analytical Modeling and Numerical Simulation”. PhD thesis. Universität Hamburg, 2011.

[118] A. Thiaville et al. “Transient domain wall displacement under spin-polarized current pulses”. In: *Eur. Phys. J. B* 60.1 (2007), pp. 15–27.

[119] A Aharoni. “Demagnetizing factors for rectangular ferromagnetic prisms”. In: *Journal of Applied Physics* 83 (1998), p. 3432.

[120] J.-S. Kim et al. “Synchronous precessional motion of multiple domain walls in a ferromagnetic nanowire by perpendicular field pulses”. In: *Nat. Commun.* 5 (2014), p. 1.

[121] M. T. Bryan et al. “Transverse and vortex domain wall structure in magnetic nanowires with uniaxial in-plane anisotropy”. In: *J. Phys.: Condens. Matter* 24.2 (2012), p. 024205.

[122] M. Albert et al. “Frequency-based nanoparticle sensing over large field ranges using the ferromagnetic resonances of a magnetic nanodisc”. In: *Nanotechnology* (in press) (2016).

[123] S. A. Wolf et al. “Spintronics: A Spin-Based Electronics Vision for the Future”. In: *Science* 294.5546 (2001), pp. 1488–1495.

[124] A. A. Tulapurkar et al. “Spin-torque diode effect in magnetic tunnel junctions”. In: *Nature* 438.7066 (2005), pp. 339–342.

[125] M. Diegel et al. “A New Four Bit Magnetic Domain Wall Based Multiturn Counter”. In: *IEEE Transactions on Magnetics* 45.10 (2009), pp. 3792–3795.

[126] R. S. Gaster et al. “Matrix-insensitive protein assays push the limits of biosensors in medicine”. In: *Nature Medicine* 15.11 (2009), pp. 1327–1332.

[127] B. Srinivasan et al. “A Three-Layer Competition-Based Giant Magnetoresistive Assay for Direct Quantification of Endoglin from Human Urine”. In: *Analytical Chemistry* 83.8 (2011), pp. 2996–3002.

[128] H. Lee et al. “Recent Developments in Magnetic Diagnostic Systems”. In: *Chemical Reviews* 115.19 (2015), pp. 10690–10724.

[129] B. Srinivasan et al. “A Detection System Based on Giant Magnetoresistive Sensors and High-Moment Magnetic Nanoparticles Demonstrates Zeptomole Sensitivity: Potential for Personalized Medicine”. In: *Angewandte Chemie International Edition* 48.15 (2009), pp. 2764–2767.

[130] V. D. Krishna et al. “Giant Magnetoresistance-based Biosensor for Detection of Influenza A Virus”. In: *Infectious Diseases* (2016), p. 400.

[131] M Helou et al. “Time-of-flight magnetic flow cytometry in whole blood with integrated sample preparation”. In: *Lab Chip* 13 (2013), pp. 1035–1038.

[132] J. Loureiro et al. “Magnetoresistive chip cytometer”. In: *Lab Chip* 11.13 (2011), pp. 2255–2261.

[133] Y. R. Chemla et al. “Ultrasensitive magnetic biosensor for homogeneous immunoassay”. In: *Proceedings of the National Academy of Sciences* 97.26 (2000), pp. 14268–14272.

[134] M. M. Miller et al. “Detection of a micron-sized magnetic sphere using a ring-shaped anisotropic magnetoresistance-based sensor: A model for a magnetoresistance-based biosensor”. In: *Applied Physics Letters* 81.12 (2002), pp. 2211–2213.

[135] L. Ejsing et al. “Magnetic microbead detection using the planar Hall effect”. In: *Journal of Magnetism and Magnetic Materials* 293.1 (2005), pp. 677–684.

[136] P. I. Nikitin, P. M. Vetoshko, and T. I. Ksenevich. “New type of biosensor based on magnetic nanoparticle detection”. In: *Journal of Magnetism and Magnetic Materials*. Proceedings of the Sixth International Conference on the Scientific and Clinical Applications of Magnetic CarriersSCAMC-06 311.1 (2007), pp. 445–449.

[137] M Donolato et al. “Nanosized corners for trapping and detecting magnetic nanoparticles”. In: *Nanotechnol* 20 (2009), p. 385501.

[138] H. J. Chung et al. “A magneto-DNA nanoparticle system for rapid detection and phenotyping of bacteria”. In: *Nature Nanotechnology* 8.5 (2013), pp. 369–375.

[139] J. Devkota et al. “Magneto-Impedance Biosensor With Enhanced Sensitivity for Highly Sensitive Detection of Nanomag-D Beads”. In: *IEEE Transactions on Magnetics* 49.7 (2013), pp. 4060–4063.

[140] D. R. Baselt et al. “A biosensor based on magnetoresistance technology1”. In: *Biosensors and Bioelectronics* 13.7–8 (1998), pp. 731–739.

[141] S. J. Osterfeld et al. “Multiplex protein assays based on real-time magnetic nanotag sensing”. In: *Proceedings of the National Academy of Sciences* 105.52 (2008), pp. 20637–20640.

[142] D. A. Hall et al. “GMR biosensor arrays: a system perspective”. In: *Biosensors & Bioelectronics* 25.9 (2010), pp. 2051–2057.

[143] V. C. Martins et al. “Challenges and trends in the development of a magnetoresistive biochip portable platform”. In: *Journal of Magnetism and Magnetic Materials*. Proceedings of the Joint European Magnetic Symposia 322.9–12 (2010), pp. 1655–1663.

[144] P. P. Freitas et al. “Spintronic platforms for biomedical applications”. In: *Lab Chip* 12.3 (2012), pp. 546–557.

[145] W. Wang et al. “Surface Modification for Protein and DNA Immobilization onto GMR Biosensor”. In: *IEEE Transactions on Magnetics* 49.1 (2013), pp. 296–299.

[146] Y. Li et al. “External-field-free magnetic biosensor”. In: *Applied Physics Letters* 104.12 (2014), p. 122401.

[147] P.-A. Besse et al. “Detection of a single magnetic microbead using a miniaturized silicon Hall sensor”. In: *Applied Physics Letters* 80.22 (2002), pp. 4199–4201.

[148] L. Di Michele et al. “Detection and susceptibility measurements of a single Dynal bead”. In: *J. Appl. Phys.* 110.6 (2011), p. 063916.

[149] J.-R. Lee et al. “Experimental and theoretical investigation of the precise transduction mechanism in giant magnetoresistive biosensors”. In: *Scientific Reports* 6 (2016), p. 18692.

[150] P. M. Braganca et al. “Nanoscale magnetic field detection using a spin torque oscillator”. In: *Nanotechnology* 21.23 (2010), p. 235202.

[151] M. Inoue et al. “Investigating the use of magnonic crystals as extremely sensitive magnetic field sensors at room temperature”. In: *Applied Physics Letters* 98.13 (2011), p. 132511.

[152] S. Atalay et al. “One-Dimensional Magnonic Crystal for Magnetic Field Sensing”. In: *Journal of Superconductivity and Novel Magnetism* 28.7 (2015), pp. 2071–2075.

[153] K. Mizushima et al. “Signal-to-noise ratios in high-signal-transfer-rate read heads composed of spin-torque oscillators”. In: *J. Appl. Phys.* 107.6, 063904 (2010), p. 063904.

[154] “Magnetic oscillator based biosensor”. Pat. US8053244 B2. P. J. Ryan, H. Xi, and I. Jin. 2011.

[155] M. Sushruth et al. “Resonance-based Detection of Magnetic Nanoparticles and Microbeads Using Nanopatterned Ferromagnets”. In: *arXiv:1604.05835* (2016).

[156] P. Wohlhüter et al. “Nanoscale switch for vortex polarization mediated by Bloch core formation in magnetic hybrid systems”. In: *Nature Communications* 6 (2015), p. 7836.

[157] J. Fried and P. Metaxas. “Localized magnetic fields enhance the field-sensitivity of the gyrotropic resonance frequency of a magnetic vortex”. In: *Physical Review B* 93.6 (2016).

[158] T. Srimani et al. “High Sensitivity Biosensor using Injection Locked Spin Torque Nano-Oscillators”. In: *arXiv:1511.09072* (2015).

[159] A. Manzin et al. “Influence of lattice defects on the ferromagnetic resonance behaviour of 2D magnonic crystals”. In: *Scientific Reports* 6 (2016), p. 22004.

[160] J. R. Petrie et al. “Using a spin torque nano-oscillator to read memory based on the magnetic permeability”. In: *Journal of Physics D: Applied Physics* 47.5 (2014), p. 055002.

[161] W. H. Rippard et al. “Spin-transfer dynamics in spin valves with out-of-plane magnetized CoNi free layers”. In: *Phys. Rev. B* 81.1 (2010), p. 014426.

[162] I. N. Krivorotov et al. “Time-Domain Measurements of Nanomagnet Dynamics Driven by Spin-Transfer Torques”. In: *Science* 307.5707 (2005), pp. 228–231.

[163] Z. Zeng et al. “High-Power Coherent Microwave Emission from Magnetic Tunnel Junction Nano-oscillators with Perpendicular Anisotropy”. In: *ACS Nano* 6.7 (2012), pp. 6115–6121.

[164] E. Grimaldi et al. “Response to noise of a vortex based spin transfer nano-oscillator”. In: *Physical Review B* 89.10 (2014), p. 104404.

[165] E. Saitoh et al. “Conversion of spin current into charge current at room temperature: Inverse spin-Hall effect”. In: *Applied Physics Letters* 88.18 (2006), p. 182509.

[166] H. Kubota et al. “Spin-Torque Oscillator Based on Magnetic Tunnel Junction with a Perpendicularly Magnetized Free Layer and In-Plane Magnetized Polarizer”. In: *Appl. Phys. Express* 6.10 (2013), p. 103003.

[167] H. Maehara et al. “High Q factor over 3000 due to out-of-plane precession in nano-contact spin-torque oscillator based on magnetic tunnel junctions”. In: *Appl. Phys. Express* 7.2 (2014), p. 023003.

[168] J. Bai and J.-P. Wang. “High-magnetic-moment core-shell-type FeCo–Au Ag nanoparticles”. In: *Applied Physics Letters* 87.15 (2005), p. 152502.

[169] M. S. Alnæs et al. “The FEniCS Project Version 1.5”. In: *Archive of Numerical Software* 3.100 (2015), pp. 9–23.

[170] A. Davison. “Automated Capture of Experiment Context for Easier Reproducibility in Computational Research”. In: *Computing in Science Engineering* 14.4 (2012).

[171] *Sumatra: automated tracking of scientific computations*. URL: http://neuralensemble.org/sumatra/ (accessed on 02/22/2016).

[172] F. Perez and B. E. Granger. “IPython: A System for Interactive Scientific Computing”. In: *Computing in Science Engineering* 9.3 (2007), pp. 21–29.

[173] *Project Jupyter: Open source, interactive data science and scientific computing across over 40 programming languages*. https://jupyter.org/. Accessed: 2016-04-20.

[174] E. Jones et al. *SciPy.org — SciPy.org*. SciPy: Open source scientific tools for Python. 2001–. URL: https://www.scipy.org/ (accessed on 03/24/2016).

[175] W. McKinney. “Data Structures for Statistical Computing in Python”. In: Proceedings of the 9th Python in Science Conference. 2010, pp. 51–56.

[176] J. D. Hunter. “Matplotlib: A 2D Graphics Environment”. In: *Computing in Science Engineering* 9.3 (2007), pp. 90–95.

[177] Jean-Luc R. Stevens, Philipp Rudiger, and James A. Bednar. “HoloViews: Building Complex Visualizations Easily for Reproducible Science”. In: *Proceedings of the 14th Python in Science Conference*. Ed. by Kathryn Huff and James Bergstra. 2015, pp. 61–69.

[178] M. Albert, P. J. Metaxas, and H. Fangohr. *Supplementary material for "Frequency-based nanoparticle sensing over large field ranges using the ferromagnetic resonances of a magnetic nanodisc"*. 2016. URL: http://dx.doi.org/10.5281/zenodo.60605.

[179] A. Rafati, R. ter Veen, and D. G. Castner. “Low-energy ion scattering: Determining overlayer thickness for functionalized gold nanoparticles”. In: *Surf. Interface Anal.* 45 (2013), pp. 1737–1741.

[180] N. Locatelli et al. “Dynamics of two coupled vortices in a spin valve nanopillar excited by spin transfer torque”. In: *Appl. Phys. Lett.* 98 (2011), p. 062501.

[181] R. Lebrun et al. “Nonlinear Behavior and Mode Coupling in Spin-Transfer Nano-Oscillators”. In: *Phys. Rev. App.* 2.6 (2014), p. 061001.